

Observational Signatures of
Recollimation Shocks in Relativistic Jets:
The Case of a Disordered Upstream Magnetic Field

Christopher Kaye

A THESIS SUBMITTED IN PARTIAL FULFILMENT
OF THE REQUIREMENTS FOR THE DEGREE OF
DOCTOR OF PHILOSOPHY

Jeremiah Horrocks Institute for Mathematics, Physics and Astronomy
University of Central Lancashire

October 2019

Declaration

Type of Award: Doctor of Philosophy

School: Physical Sciences and Computing

I declare that while registered as a candidate for the research degree, I have not been a registered candidate or enrolled student for another award of the University or other academic or professional institution.

I declare that no material contained in the thesis has been used in any other submission for an academic award and is solely my own work.

No proof-reading service was used in the compilation of this thesis.



Christopher Kaye

Abstract

Astrophysical jets launched from active galactic nuclei can remain highly collimated over large distances due, in part, to recollimation shocks; the aim of this work was to determine what signatures of a recollimation shock are imparted into a hydrodynamic flow after crossing these shocks, for plasma with an initially completely disordered flux-frozen magnetic field. This work uses a statistical treatment of the magnetic field (c.f. Matthews & Scheuer, 1990), in which initially orthogonal vector triads (each vector monitoring one side of a parallelepipedic volume) are advected with the flow; these vectors are then used to determine the volume’s emissivity. A modified version of the Hughes et al. (2002) code was employed to determine the parallelepiped advection using the same Godunov-type solver it employs to solve the Euler equations; it was found that the jets developed strong cylindrical asymmetries, however, and some parallelepiped components experienced huge growth, inexplicable in terms of the jet’s velocity gradients. It was then decided to determine the parallelepipeds for time-independent, axisymmetric jets from the code of Fuentes et al. (2018). The parallelepiped evolution in steady flows may be determined by advecting marker particles with the flow, as the pathlines and streamlines are identical. We present the equations to describe the polarization for the cases of initial magnetic field that are (i) completely disordered, and (ii) partially ordered, consisting of a disordered component with a uniform or helical component. We present the data from three jet models with the same initial Lorentz factor and over-pressure ratio, characterized by their levels of internal energy as either “hot”, “intermediate”,

or “cold”. For each model, we determine the total and fractional polarizations for lines of sight through the centre of widest and narrowest parts of the jets, for a range of viewing angles; similar variations of these parameters are found to occur in each model, but at higher viewing angles in the hotter models. Simulated images of the total and polarized flux densities, and fractional polarization are discussed for a range of viewing angles; importantly, we find that the recollimation shock structures in a jet may be clearly seen in its fractional polarization distribution. This work may be further developed by the inclusion of opacity and spectral ageing, and through the exploration of parameter space of the jet and initial magnetic field properties.

Contents

Declaration	ii
Abstract	iii
Acknowledgements	xiii
1 Introduction	1
1.1 Radio-Loud Active Galaxies	1
1.1.1 Astrophysical Jets	5
1.1.2 AGN Unification Schemes	8
1.1.3 Jet Launching Mechanisms	11
1.2 Emission and Polarization	13
1.3 Previous Jet and Shock Simulations	17
1.3.1 Jet Simulations	17
1.3.2 Shock Simulations	21
1.4 The Necessity of Disordered Magnetic Fields	27
1.5 Recent Developments	29
1.5.1 Observations	29
1.5.2 Simulations	31
2 Three-Dimensional Simulations	33
2.1 Fluid Dynamics	34

2.1.1	Godunov Approach	35
2.2	Boundary and Initial Conditions	36
2.2.1	Boundary Conditions	37
2.2.2	Initial Conditions	38
2.3	Flux-Based Parallelepiped Vector Monitoring	40
2.4	Relativistic Motion Transforms	42
2.5	Validating the Modified Code	43
2.5.1	Resolution Comparison	44
2.5.2	Testing the Parallelepipeds with Planar Shocks	44
2.6	Parallelepiped Evolution	49
2.6.1	Anomalous Parallelepiped Growth	50
2.7	First-Order Parallelepiped Vector Evolution	52
2.7.1	Comparison with Streamline-Based Parallelepipeds	55
2.7.2	Hydrodynamical Asymmetries	60
2.8	Summary	60
3	Axisymmetric Simulations: Methods	63
3.1	The Simulation Suite	64
3.1.1	Azimuthal Velocities	66
3.1.2	Verifying the Hydrodynamic Nature of the Flow	67
3.2	Determining Synchrotron Emission Coefficients	72
3.2.1	Stokes Parameters	72
3.2.2	Determining the Synchrotron Emission	73
3.2.3	Defining the Magnetic Field	76
3.3	Streamline-based Parallelepiped Monitoring	80
3.3.1	Obtaining Extraplanar Parallelepipeds	83
3.4	Rest-Frame Parallelepiped Vector Transforms	85
3.5	Radiative Transfer and Transforming Emission Coefficients	87

4	Results	90
4.1	Data Processing	90
4.1.1	Radial Jet Trimming	91
4.1.2	Gaussian Smoothing	92
4.2	Presentation of the Data	97
4.2.1	Simulated Lines of Sight	103
4.2.2	The Simulated Images	113
4.3	Comparison with Observations	132
4.3.1	0044+566	134
4.3.2	1803+784	134
4.3.3	M87	136
5	Summary and Conclusions	142
5.1	Conclusions	144
5.2	Further Work	146
	References	149

List of Tables

2.1	Hydrodynamical jet parameters in the injection plane	41
3.1	Parameters of MHD jet models in the inlet plane	64

List of Figures

1.1	AGN jets and cocoon schematic	2
1.2	Radio images of 3C 31 and 3C 175	4
1.3	Recollimation shocks in supersonic, terrestrial jets	6
1.4	The Unification Scheme for Active Galactic Nuclei	10
2.1	The Riemann Problem for a pressure discontinuity	35
2.2	Absolute velocity profiles of Punch initialized simulation	39
2.3	Lorentz factor cross-sections of simulations RES1 and RES2	45
2.4	On-axis profiles of Lorentz factor and pressure in RES1 and RES2	46
2.5	Comparison of densities in PLN at multiple epochs	48
2.6	CTRL inlet boundary cross-sections of $ \beta $ and c_z	49
2.7	CTRL and XTND cross-section of Lorentz factor, and v_z and c_z profiles	51
2.8	Lorentz factor cross-section for GBOX, and profiles of v_z and c_z	53
2.9	CTRL and XTND cross-sections of c_z , and profiles of v_z and c_z	56
2.10	Lorentz factor profile of ORD1	57
2.11	Pre-shock parallelepiped components of ORD1 determined by direct-differencing and streamline-based methods	58
2.12	Post-shock parallelepiped components of ORD1 determined by direct-differencing and streamline-based methods	59
2.13	ORD1 Lorentz factor cross-sections showing jet asymmetries	61
3.1	Lorentz factor profiles of models J105, J106 and J109	65

3.2	Cross-section of the azimuthal velocity in J106, and the estimated twist induced	68
3.3a	Comparison of the radial velocity profiles of J105 and J119	70
3.3b	Comparison of the axial velocity profiles of J105 and J119	71
3.4	Schematic of marker particle advection and how this corresponds to the parallelepiped vectors	81
3.5	Axis reference frames for determining emissivities	86
4.1	Pixel $I(r)$ for two x - y slices through the cold jet	91
4.2	The radial boundary for each model as a function of z -position	92
4.3a	Profiles of components v_r , v_z , a_x , and a_z for the cold model	93
4.3b	Profiles of components b_y , c_x and c_z , and $V'^{-11/3}$ for the cold model	94
4.4	Parallelepiped a_x component plots with streamlines for striated pixels	95
4.5	Radial velocity difference as a function of radial velocity for a selection of streamline marker particles	96
4.6	Simulated P image of the cold jet at $\theta = 5^\circ$, for unsmoothed parallelepiped components	96
4.7	Comparison of a_x before and after smoothing in the cold jet	98
4.8	On-axis profile of Γv_z across the first bubble of each model	99
4.9a	Profiles of components v_r and v_z , and the smoothed components a_x and a_z for the cold model	101
4.9b	Profiles of smoothed components b_y , c_x and c_z , and $V'^{-11/3}$ from the smoothed components, for the cold model	102
4.10	Comparison of density- and parallelepiped-based measures of pixel monitoring	104
4.11	Stokes Q as a function of θ for lines of sight through the jet bubble	105
4.12	Fractional polarization as a function of θ for lines of sight through the jet bubble	105

4.13	Stokes Q as a function of θ for lines of sight through the jet pinch point	106
4.14	Fractional polarization as a function of θ for lines of sight through the jet pinch point	107
4.15	Average parallelepiped components \tilde{a}'_x , \tilde{b}'_y , and \tilde{c}'_z as a function of viewing angle, for lines of sight through the jet bubble	108
4.16	Average parallelepiped components \tilde{a}'_x , \tilde{b}'_y , and \tilde{c}'_z as a function of viewing angle, for lines of sight through the jet pinch point	109
4.17	Comparison of Stokes Q and its estimate, as a function of viewing angle	110
4.18	Lines of sight for each model that intersect the same parts of their respective jets	112
4.19	Simulated I images of the hot model at $\theta = 5^\circ$, 10° and 20° , with EVPA sticks overplotted	114
4.20	Simulated P images of the hot model at $\theta = 5^\circ$, 10° and 20°	115
4.21	Simulated II images of the hot model at $\theta = 5^\circ$, 10° and 20°	116
4.22	Comparison of shock structures and II in the hot jet	118
4.23	Simulated I images of the intermediate model at $\theta = 5^\circ$, 10° and 20° , with EVPA sticks overplotted	119
4.24	Simulated P images of the intermediate model at $\theta = 5^\circ$, 10° and 20°	120
4.25	Simulated π images of the intermediate model at $\theta = 5^\circ$, 10° and 20° .	121
4.26	Simulated I images of the cold model at $\theta = 5^\circ$, 10° and 20° , with EVPA sticks overplotted	124
4.27	Simulated P images of the cold model at $\theta = 5^\circ$, 10° and 20°	125
4.28	Simulated II images of the cold model at $\theta = 5^\circ$, 10° and 20°	126
4.29	Images of 0836+710 at 15.4 GHz: contours of total and polarized intensity, overplotted with fractional polarization and EVPA sticks . .	131

4.30	Simulated I images of the cold model, with EVPA sticks overplotted, at $\theta = 20^\circ$, after being convolved with Gaussian kernels of FWHM 50, 100, and 150 pixels	133
4.31	Images of 0044+566 at 15.4 GHz: contours of total and polarized intensity, overplotted with fractional polarization and EVPA sticks . .	135
4.32	Images of 1803+784 at 43 GHz	137
4.33	Simulated P and II images of the cold model at $\theta = 20^\circ$, after being convolved with a Gaussian kernels of FWHM 50 pixels	138
4.34	Nucleus of M87, and knot HST-1, at 22 GHz: contours of total intensity, overplotted with magnetic field vector sticks proportional to the polarized intensity and fractional polarization	140

Acknowledgements

I would first like to thank Tim Cawthorne for his brilliant guidance; I will never be able to repay his kindness. Philip Hughes deserves my thanks for his invaluable suggestions on this work. My unending gratitude also goes out to José-María Martí, who generously provided the simulation data that forms the backbone of this thesis. I would also like to thank my viva examiners, José Luis Gómez and Derek Ward-Thompson, for an enjoyable discussion of my work, and valuable improvements to this document.

Appreciations go out to Leigh-Anne Homer and Stacey Mackenzie-Wintle, who were always there for me, and never let me forget that there is a world outside of my computer terminal. Thanks to Danny Lee and Simon Smalley, for trying to keep me sane; lesser thanks go to Andrew Walker, for trying the opposite! I am also grateful to my housemates, past and present, for their patience; I am specifically grateful for Jordan Thirlwall's steady supply of food and tea.

I dedicate this thesis to my family, for their continued support throughout this long journey, and for their understanding and patience when I became an irritable recluse. I made it, like you always knew I could.

In the beginning the Universe was created.
This has made a lot of people very angry
and been widely regarded as a bad move.

The Hitchhiker's Guide to the Galaxy
DOUGLAS ADAMS

Chapter 1

Introduction

Active galaxies are some of the most luminous of objects, and thus are readily detectable throughout the distant universe. There are two distinct classes of active galaxy—radio-loud and radio-quiet; their thermal emissions (infrared to X-ray continua and spectral lines) appear similar, but, as the names imply, the greatest distinctions lie in their radio emissions (summarized by Wilson & Colbert, 1995). Radio-loud active galaxies account for only $\sim 10\%$ of all detected active galaxies (Kellermann et al., 2016, and references therein), and emit strongly in radio frequencies, having significantly luminous relativistic collimated outflows (“jets”) and lobes. Radio-quiet active galaxies produce jets that are either energetically insignificant or completely unobservable, and as such we only concern ourselves with radio-loud galaxies hereafter.

1.1 Radio-Loud Active Galaxies

Radio-loud active galaxies all share a few key morphological components, including the aforementioned jets; in some cases these highly collimated structures extend

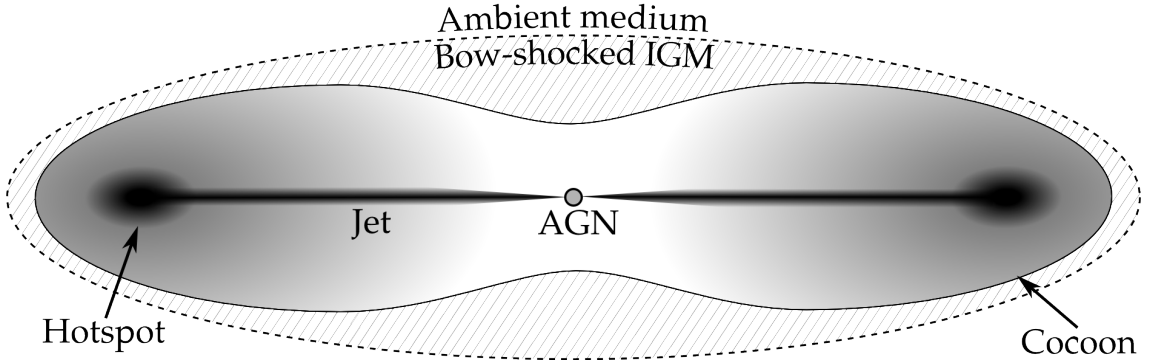


Figure 1.1: AGN jets produce bow shocks and two-lobed cocoons (with embedded hotspots) as they propagate into an ambient medium

up to megaparsec scales. The jets propagate away from the optically thick radio-core, which is a region of extremely high luminosity, downstream from the jet-launching regions within the active galactic nucleus (AGN). It is expected that the ultraviolet and higher frequency radiation coming from this central region are produced on scales smaller than the radio-core, although correlations between the electric vector polarization angles (EVPAs) of radio and optical emission have been found, suggesting they may come from the same region (e.g. Gabuzda et al., 1996). Aspects of the radio-core are discussed later, but for now we note that these highly emissive, optically thick surfaces are frequency dependent.

As a jet propagates away from the AGN, it must displace the surrounding intergalactic medium (IGM). This induces a bow shock at the leading edge of the jet; upstream jet material that reaches this shock will back-flow and fill a cocoon bounded by the shocked IGM (Scheuer, 1974), as shown in Figure 1.1. Where the jet collides with the IGM and terminates, or is strongly disrupted, a region of increased luminosity known as a “hotspot” occurs. This deflected material forms a diffuse lobe that surrounds the more emissive hotspot, and the region of highest plasma compression is expected to be the source of the hotspot. As the jet material imparts energy into the much denser ambient medium, recession speed of the hotspot will

CHAPTER 1

necessarily be much lower than that of the incident jet material. Smaller, sometimes transient, regions of enhanced emissivity, called knots, may also occur along the length of the jets; knots often display superluminal motion, but may also be stationary features. The bottom panel of Figure 1.2 shows the radio source 3C 175, associated with a quasar at a redshift $z = 0.768$ (Lynds, 1967), which has clear examples of radio lobes, hotspots, a jet with knots, and a radio-core.

There are many properties used to classify radio-loud active galaxies, and one of the most widely-known schemes was developed by Fanaroff & Riley (1974), who found that the total low frequency radio luminosity correlates with the relative galaxy-hotspot separation. Fanaroff-Riley class I (FR I) sources, in which hotspots are closer to the central galaxy than to the jet extremities, generally have two oppositely-directed jets emerging from the host galaxy. Comparatively, Fanaroff-Riley class II (FR II) sources often have a single, narrower, more powerful jet emerging from the galaxy, and are defined by their hotspots forming closer to the ends of the jets than their host galaxy. Figure 1.2 shows a well-known example of both types; in the top panel is the FR I radio galaxy 3C 31, located at a redshift of $z \approx 0.017$ (Smith et al., 2000), and the quasar 3C 175 is an FR II radio source.

The observational history of active galaxies means that many categories have overlapping criteria, but some of the major subdivisions are listed here:

(i) Radio galaxies have a radio-core with narrow spectral lines and two radio lobes with hotspots; additionally, FR II radio galaxies also display strong featureless optical continua and broad components to their spectral lines.

(ii) Quasars are compact radio sources that have both broad and narrow spectral lines, and have either lobe- or core-dominated radio emission, which have steep and flat spectra respectively.

(iii) BL Lac objects (named after their archetype, BL Lacertae) exhibit rapidly variable emission and high levels of polarization, with featureless optical continua.

CHAPTER 1

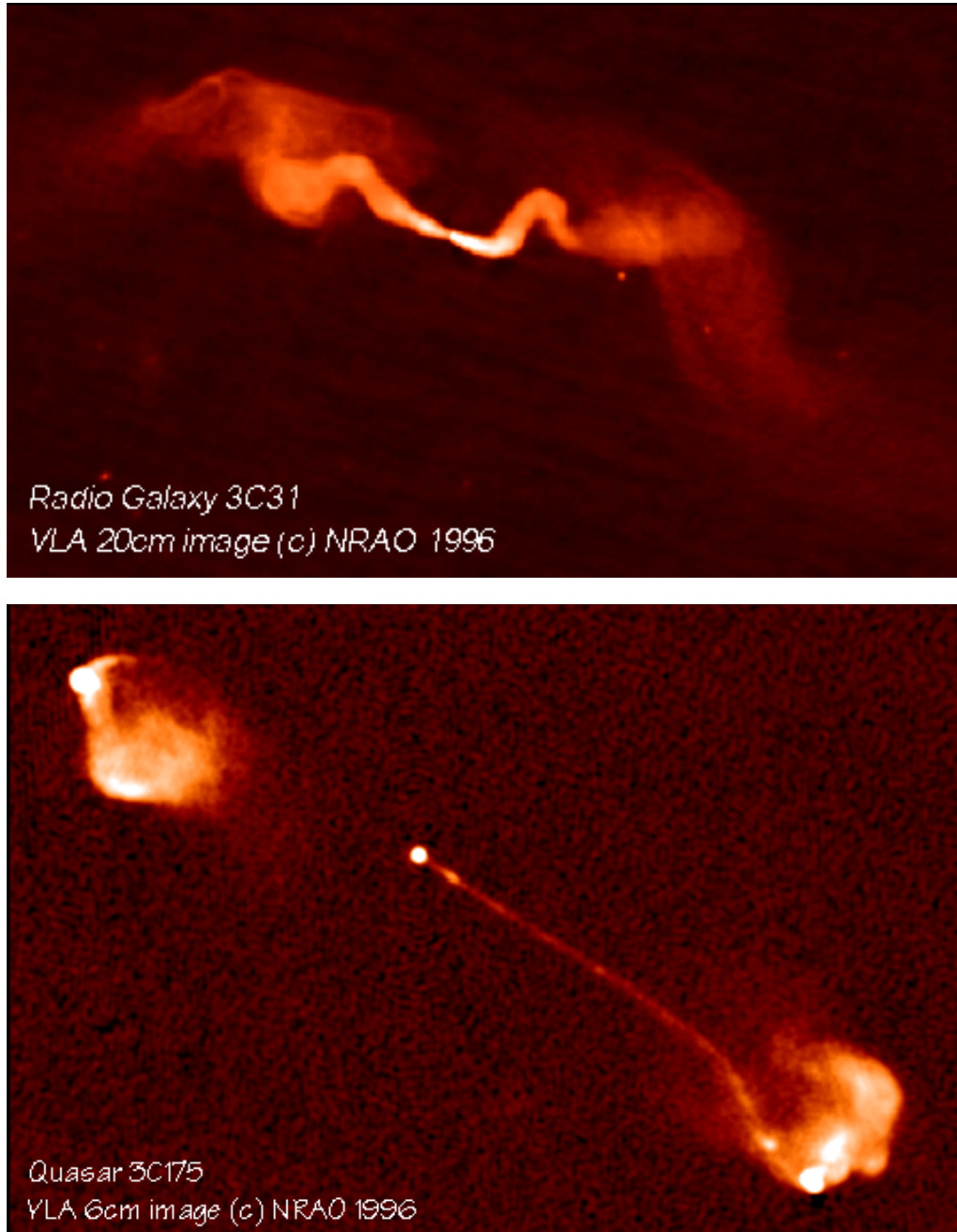
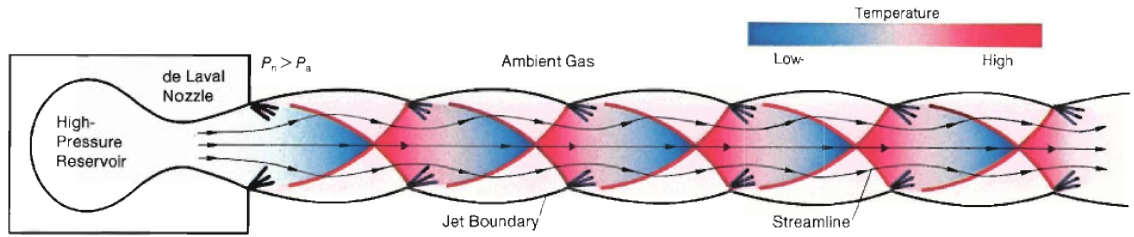


Figure 1.2: Very Large Array images of radio sources 3C 31 (top) and 3C 175.
Images courtesy of NRAO/AUI

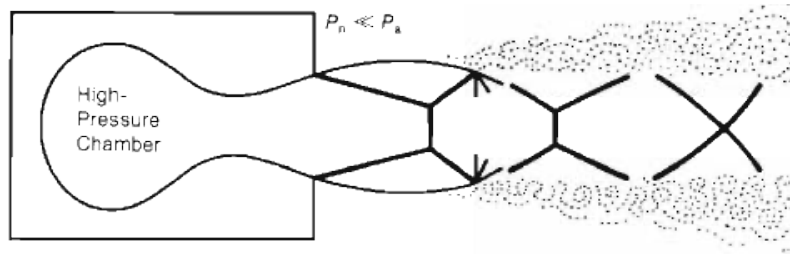
1.1.1 Astrophysical Jets

As noted previously, hotspots occur where the jet material is strongly shocked; it is currently thought that weaker, less disruptive shocks may be the cause of the bright knots seen along some jets. Sanders (1983) and Wilson & Falle (1985) both show that over-pressured, steady jets will readily form internal shocks which act to recollimate the flow and keep the jet in equilibrium with the ambient medium. In a stable flow, these recollimation shocks (RSs) remain stationary with respect to the base of the jet, and are thought to be the explanation for radio-cores and the stationary bright knots observed in many jets (Daly & Marscher, 1988).

The formation of RSs within astrophysical jets is due to the pressure imbalance between the jet and its surroundings. The ambient medium has a low pressure, so a jet propagating through it will expand laterally; because of the inertia of the jet material, and the flow being supersonic, the jet will over-expand and become under-pressured with respect to the IGM, and thus be driven radially inwards. A series of RSs may occur as the jet oscillates about its equilibrium pressure, but these shocks are both smooth and weak in comparison to the bow shocks that result in the hotspots. This is thoroughly described by Norman & Winkler (1985), wherein the mechanics of terrestrial jets are discussed; these are over-dense in comparison to the ambient medium, whereas astrophysical jets are under-dense, although pressure is the confining parameter for both jet types. Figure 1.3 illustrates a series of initially over-pressured, over-dense laboratory jet flows and RSs. Astrophysical jets tend to be under-dense with respect to their environment, but this figure serves to illustrate the general structure of RSs, specifically shock diamonds in Figure 1.3a, which act to collimate the jet; in some instances, a Mach disc will form at the “X” point, such that the shock has a transverse disc at the centre and is edged by the diamond components (Figure 1.3b).



(a) Shock diamonds in a supersonic jet.



(b) Recollimation shocks with and without Mach discs.

Figure 1.3: Recollimation shocks in supersonic, terrestrial jets with high pressure and density (Norman & Winkler, 1985).

Relativistic Jets

The typical AGN jet has relativistic bulk motion (with Lorentz factors $\Gamma \sim 10$), likely composed of an electron–positron dominated plasma (Wardle et al., 1998; Kino & Takahara, 2004). These particles have highly relativistic random motions ($\Gamma \gtrsim 10^3$) and the jet plasma, compared to the IGM, has low density and high pressure (Worrall & Birkinshaw, 2006, Chapters 6.3–6.4).

The tendency for radio-loud active galaxies to have apparently one-sided jets was once thought to be due to intrinsic asymmetries in these sources (e.g. van Groningen et al., 1980); when combined with other lines of evidence, however, it became clear that parsec-scale AGN jets are two-sided and experience relativistic Doppler beaming. Firstly, the rapid variability observed in jet emissions is explained by relativistic beaming making the flux changes seem accelerated (Mutel et al., 1981). This was suggested earlier by Rees (1966), who accurately predicted that this would lead to apparent superluminal motion in the on-sky projections of many astrophysical

CHAPTER 1

jets (e.g. Cohen & Unwin, 1982), which can occur when a jet has a significant component of relativistic velocity directed towards the observer (Blandford & Königl, 1979). Lastly, we mention the “inverse-Compton problem”, wherein the predicted X-ray inverse-Compton emission exceeds the observed flux, unless bulk relativistic motion is allowed for (Unwin et al., 1994).

The scientific community was initially sceptical of jets remaining relativistic on kiloparsec scales, with some suggesting that the large-scale jets were independent from the VLBI jets, and remaining sub-relativistic. This is not possible, however, as Scheuer (1984), while strongly advocating for the relativistic beaming model, explains that if the VLBI-scale jets are relativistic, then the large-scale jets must also be so. It is known that when mapped, the VLBI-cores, present wherever there are large-scale jets, display a VLBI jet pointing towards the large-scale jet. If the large-scale jets were sub-relativistic, then we would arrive at predictions that contradict observations, regardless of whether the relativistic VLBI jets are intrinsically one-sided or not. Supposing the VLBI jets are one-sided, then half of all observed sources should have a large-scale jet with no visible VLBI core, and if they are two-sided then the two scales of jet should be seen on opposite sides of the radio-core in $\sim 50\%$ of observations (Bridle, 1992); neither of these predictions are borne out. In fact, the parsec- and kiloparsec-scale jets always appear on the same side of the radio-core; if one scale of jet is intrinsically one-sided and independent of the other, then there should be many detections of the two scales of jet being on opposite sides of the radio-core, but there is not even one. One more instance of evidence supporting relativistic kiloparsec-scale jets comes from observations that the Faraday depolarization rate with frequency in active galaxies was lower for the lobes containing a radio jet than for lobes with no visible jet (Garrington et al., 1988; Laing, 1988). This was suggested to be a result of the lobe with a visible jet being directed towards the observer, and thus having a shorter path-length through

CHAPTER 1

a Faraday rotation (FR) inducing medium surrounding the source; emission from the lobe with no jet, which would consequently be directed away from the observer, would have a longer path-length through the FR “screen”, and also be beamed away from the observer, thus rendering the receding jet too dim to be observable. This explains the asymmetry in FR, provided both jets remain relativistic on kiloparsec scales; an alternative solution would require a contrived geometry of the FR-inducing medium, and intrinsic one-sidedness in certain classes of active galaxies.

With evidence that jets are highly relativistic on both parsec and kiloparsec scales, it was realized that relativistic effects played a large role in determining the appearance of these jets. This caused some astronomers to suggest that observationally distinct radio-loud active galaxies are actually structurally similar.

1.1.2 AGN Unification Schemes

The Unification Scheme (Antonucci, 1993; Urry & Padovani, 1995) posits that the observed variations between the numerous types of active galaxies is due to differences in their orientation and level of obscuration, with respect to the observer. Figure 1.4 shows the components thought to be common to all AGNs, with the compact supermassive black hole and accretion disc being integral to generating such high luminosities within the relatively small regions that AGNs are known to occupy. Closely surrounding these are broad line clouds, with a region of narrow line clouds encompassing these in turn. Radiation absorbed by a gas is re-emitted with Doppler broadened emission lines, the extent of the broadening increasing with the blackbody temperature of the gas cloud; hence the broad and narrow line clouds are composed of high- and low-velocity gas, respectively. While the jets of active galaxies dominate the production of hard X-rays, it is thought that more of the softer X-ray emission is from a hot corona that surrounds the accretion disc. Obscuring part of this system is a dusty torus-like absorber, with a symmetry axis that is often

CHAPTER 1

closely aligned with the radio jet axes.

Unification via obscuration contends that many narrow line objects (NLOs), i.e. AGNs exhibiting only narrow spectral lines, are from the same population as broad line objects (BLOs), which emit both narrow and broad spectral lines, but that these two groups are being observed from different orientations with respect to their symmetry axes. Antonucci & Miller (1985) found that multiple NLOs showed broad lines in their polarized light, which were not apparent in the unpolarized spectra. It was inferred that the region producing narrow line emission was always directly visible, while the broad line emission was being obscured in some cases; in these instances, the presence of broad spectral lines in the polarized radiation suggested that they were being observed as scattered light, because the scattering process polarizes radiation. This evidence has been used to suggest the existence of the dusty torus.

Unification via orientation suggests that the angle between the observer's line of sight and the AGN jet-axis drastically alters how the active galaxy appears due to relativistic effects. Padovani & Urry (1992) found that the observed luminosity functions for core- and lobe-dominated quasars were well replicated with models for relativistic beaming at angles of $\lesssim 14^\circ$ and $\lesssim 38^\circ$ to the line of sight, respectively. Additionally, the beamed luminosity function for FR II radio galaxies was found to be very similar to that of the lobe-dominated quasars, suggesting that with the same orientation, multiple active galaxy types would appear similar.

While these unifications may seem promising, a number of important variables are overlooked, including the various parameters of the torus, the spectrum of AGN jet strengths, and the accretion rate of the black hole. Some active galaxies are also highly variable with time, meaning that a static explanation such as this is somewhat simplistic.

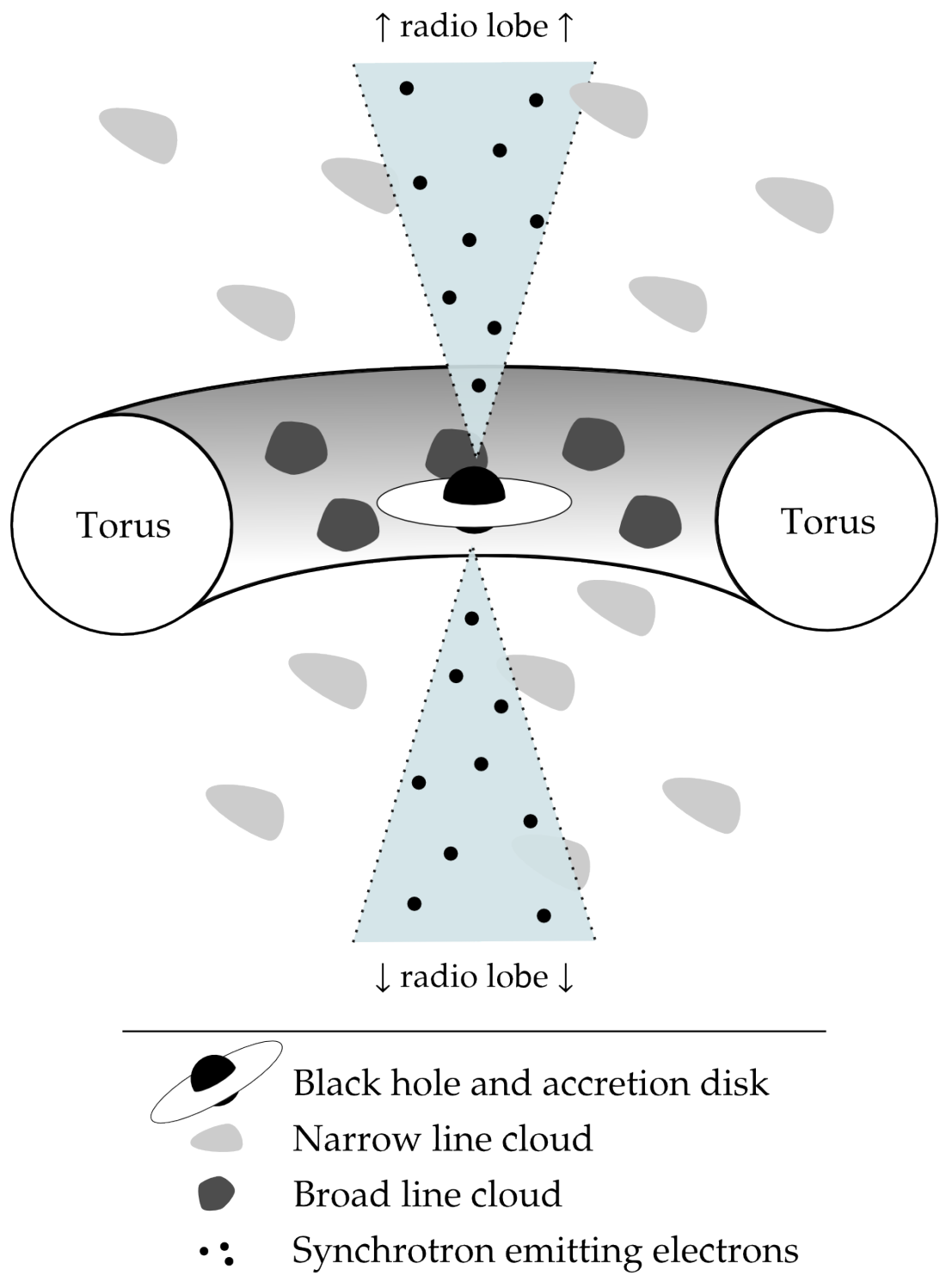


Figure 1.4: The Unification Scheme for Active Galactic Nuclei

1.1.3 Jet Launching Mechanisms

The RadioAstron satellite, in combination with terrestrial telescopes, has been able to resolve the jet in 3C 84 from ~ 0.001 to ~ 0.1 parsecs from the black hole (Giovannini et al., 2018), and Very Long Baseline Interferometry (VLBI) observations have been used to determine that the 5.5 gravitational radius, or 3.2 milliparsec radius, jet in M87 is launched from an accretion disc rotating prograde with respect to the black hole (Doeleman et al., 2012). These observations, while impressive, still lack the resolution that is required to detail predicted jet-launching regions.

In addition to this, the observed position of the radio-core is frequency dependent, and multiple frequencies of radio observations are often combined to produce images of jets that are sensitive to structures at different length scales. The “core-shift problem” (Marcaide & Shapiro, 1984) arises as a result of these two facts, because at higher frequencies (and hence higher resolution) the optically thin region begins nearer the base of the jet than at lower frequencies, and so it is not a trivial matter to align multifrequency observations. Inadequate resolution and core-shift issues are two factors contributing to the persisting uncertainty over the exact processes for the production of jets in radio-loud AGN.

Numerous mechanisms of producing jets have been suggested over the decades, invoking a wide range of features, but we are still unable to unambiguously declare the exact processes involved. Radiation driven jets have been proposed (e.g. Lynden-Bell, 1978), but would be unable to produce highly relativistic jets. As the speed of the jet increases, there comes a point in the rest-frame at which the radiation field exerts a backwards drag on the jet. This occurs because it is the radiation that meets the jet head-on which is the most strongly blueshifted, in the jet fluid’s rest-frame.

The jet-acceleration mechanisms most frequently discussed are those put forward by Blandford and coworkers. First, Blandford & Znajek (1977) showed that

CHAPTER 1

for a magnetic field threading and co-rotating with a black hole accretion disc with enough angular momentum, charged particles in the vicinity will be accelerated, producing synchrotron radiation that may, in turn, decay into an electron–positron pair, resulting in a cascade of pair-production. While the plasma itself merely supports the magnetic fields, such free production of charged particles will result in a force-free electromagnetic field; energy and angular momentum are then able to be transported outwards similarly to the mechanism proposed by Penrose (1969)—instead of rotational energy being extracted from a black hole by particles entering its ergosphere, however, it is done by particles inside the event horizon interacting with exterior particles by using the threaded magnetic field.

Later, while also considering a magnetic field that co-rotates with a black hole accretion disc due to flux-freezing, Blandford & Payne (1982) suggested that magnetic stresses remove energy and angular momentum from the accretion disc of a black hole, instead of from the black hole itself. In this model, the accretion disc itself supplies the material for the jets, where the magnetic field is not normal to the accretion disc above the disc surface. Close to the disc, the flow is assumed to be driven by gas pressure in a hot magnetically dominated corona. If the angle between the disc surface and a magnetic field line is smaller than 60° , then matter has enough kinetic energy to move radially outwards along the magnetic field line, outwards from the black hole.

As for collimating the jet material, it has been suggested that a toroidal component of magnetic field, produced due to differential rotation of the accretion disc at large radii, acts to collimate the outflow; the findings of Boccardi et al. (2016) support this by finding that the outer regions of the accretion disc in Cygnus A are indeed connected to the launching of its jet. However, Eichler (1993) argues that magnetic confinement alone would require magnetic fields strong enough to also disrupt the flow of the jet, and that any magnetic contribution to jet collimation ought

CHAPTER 1

to be modest.

These three mechanisms form the basis of many of the more recent models proposed, such as those involving “magnetically arrested” accretion discs, which suggest that the magnetic field around the black hole may become so strong that the infall of matter and the accretion disc rotation become halted. As discussed by Tchekhovskoy (2015), however, supposing the accretion disc does become magnetically arrested, there are certainly other mechanisms involved in this process. The base models themselves are far from perfect as a starting point too; e.g. Livio et al. (1999) criticized Blandford & Znajek (1977) for assuming that stronger magnetic fields threaded the accretion disc at greater radii, and for producing under-powered jets. This is not to say that they are without utility, however, as Zamaninasab et al. (2014) found that the estimated accretion disc luminosity was proportional to the VLBI-measured magnetic flux for a number of AGNs, supporting the conjecture that there is an electromagnetic component to the launching process.

1.2 Emission and Polarization

Radio emission from jets is almost exclusively produced as the result of synchrotron radiation, as suggested by the non-thermal spectra and often high levels of polarization observed. Synchrotron emission occurs when charged particles are accelerated by a magnetic field, and assuming a plasma is comprised of electrons and positrons with identical numbers and energy distributions, the total synchrotron radiation produced by each lepton is equal; the opposite charge between the particles means that electrons will gyrate about the magnetic field in a right-handed sense, while a positron will gyrate in a left-handed sense.

Synchrotron radiation from a single electron* is elliptically polarized, and the frequency of the emission extends up to $\nu \simeq \Gamma^2 \nu_L$, where the Larmor frequency

*The term *electron* here may be used interchangeably with any other charged particle.

CHAPTER 1

of a particle with rest mass m and charge q , in a magnetic field \mathbf{B} , is given by $\nu_L = q|\mathbf{B}|/(2\pi m)$. Both the power and peak frequency of a radiating electron are proportional to the square of its energy (e.g. Condon & Ransom, 2016, §5.2); as such, the higher energy electrons radiate away their energy first. As the population ages, a sharp turn-down in the spectral energy distribution forms that moves to lower energies as time progresses (Longair, 2011). For an ensemble of electrons with a power-law energy distribution $N(E) = N_0 E^{-\gamma}$, the total emission coefficient is

$$\varepsilon_\nu \propto N_0 B_\perp^{(1+\gamma)/2} \nu^{(1-\gamma)/2}$$

where B_\perp is the component of magnetic flux density perpendicular to the line of sight (e.g. Pacholczyk, 1970). This work currently only considers optically thin emission, and so the emission intensity $I_\nu = \int_L \varepsilon_\nu d\ell$ is produced along the line of sight L .

The radio emission from AGN jets may be very strongly polarized, with degrees of linear polarization up to $\sim 70\%$, although they are usually significantly smaller than this at $\lesssim 20\text{--}30\%$. The circularly polarized flux, conversely, is extremely weak, generally comprising $\lesssim 0.1\%$ of the total flux (levels of $\lesssim 1\%$ are sometimes detected; Thum et al., 2018). A statistically random distribution of electron velocities, relative to the local magnetic field, yields synchrotron emission with right- and left-handed components of circular polarization that are nearly equal and opposite. Throughout this work, we assume that no circularly polarized radiation is produced.

The high conductivity of the plasma requires that magnetic flux-freezing occurs within the jets, such that the plasma and magnetic field lines are tethered together (Longair, 2011); this in conjunction with the high level of linear polarization in synchrotron radiation, and the geometrical relationship between the magnetic field and the emitting electrons, means it may be possible to infer certain features of the magnetic field and jet structure from the synchrotron polarization. It must be noted that observationally, however, we are unable to determine the magnetic field

CHAPTER 1

direction of an observed source, instead measuring the direction of the radiation's electric field, which is perpendicular to the on-sky projection of the magnetic field. Additionally, in cases where the source is moving relativistically, the relation between the magnetic and electric field vector polarizations may be more complex than simple perpendicularity (Lyutikov et al., 2005).

Most noticeable for an initially disordered magnetic field, a transverse shock would order the magnetic field perpendicularly to the flow direction, as this component would be enhanced, while the longitudinal field component remains unchanged. Conversely, a shearing flow would enhance the longitudinal magnetic field component, giving rise to an ordered field parallel to the jet; this is generally the case (Bridle, 1982), and Kahn (1983) produced a fairly successful model with flux-freezing and shearing.

Much work has been done to show that the moderate compression of a randomly tangled magnetic field can drastically increase the field's ordering as seen from angles close to the plane of compression (e.g. Laing, 1980; Hughes et al., 1985), a brief overview of which is given in Section 1.3.2. This compression also increases the emissivity of the plasma (e.g. Pacholczyk, 1970), meaning that the observed synchrotron radiation acquires a higher intensity and degree of polarization (e.g. Cohen et al., 2014; Gómez et al., 2016). It has long been hypothesized that these shocks may be the cause of the knots and radio-cores often seen in jets (Daly & Marscher, 1988).

Although other phenomena may have greater influence on the overall structure of jets (e.g. Gourgouliatos & Komissarov, 2018), there should obviously be polarization signatures of shock compression in the emission of recollimated jets (e.g. Cawthorne & Cobb, 1990; Cawthorne, 2006); hence, it may be possible to use recollimation shocks as a diagnostic in determining some properties of their host AGN (Hervet et al., 2016, 2017). More recently, Park et al. (2019) found that the rotation measure (RM, defined in the following paragraph) at the HST-1 knot in the jet of M87 is an

CHAPTER 1

order of magnitude larger (and of the opposite sign) than the RM profile inside the Bondi radius*. They conclude that the presence of a RS at HST-1 (as suggested by Stawarz et al., 2006, and others) is consistent with their findings of such large RM values which, they suggest, are caused by a compact emitting region associated with a RS, surrounded by hot jet material.

However, the rotation measure is one of the factors that can also act to obfuscate the relationship between polarization and the structure of the jet, along with the aforementioned core-shift issues, and Faraday rotation (mentioned briefly in Section 1.1.1), wherein the polarization angle of radiation is rotated as it propagates through an appropriate medium, such as a magnetized plasma of thermal electrons surrounding a source of emission. The rotation angle ϕ is determined by the emission wavelength λ and the rotation measure RM as follows (e.g. Binney & Merrifield, 1998)

$$\begin{aligned}\phi &= \lambda^2 \cdot \text{RM} \\ \text{RM} &\propto \int_L n_e \mathbf{B} \cdot d\boldsymbol{\ell}.\end{aligned}\tag{1.1}$$

The rotation measure depends on the electron density n_e and the magnetic flux density \mathbf{B} of any plasma along the line of sight L , meaning that the rotation measure can vary between different sources, or within an individual source. As can be seen from Equation (1.1), the direction of the magnetic field with respect to L will determine the direction of rotation. A multitude of transverse RM gradients across jets have been reported in a range of sources; the implication of a RM gradient is that there is a helical structure to the magnetic field in the FR-inducing medium surrounding jets (e.g. Gabuzda et al., 2014, 2015b, and many others). These controversial conclusions been contested by Taylor & Zavala (2010), who claim that many

*Knot HST-1 is located beyond the Bondi radius; beyond the Bondi radius, the gravitational potential energy of a black hole is less than the thermal energy of the local gas.

CHAPTER 1

of the observed gradients are disputable due to low resolution, opacity where the gradient is measured, and low signal-to-noise ratios. Wardle (2013) opines that new technologies may remedy many of Taylor & Zavala’s criticisms, while also suggesting that RM gradients may merely indicate toroidal components of magnetic fields, not necessarily fields which are fully helical.

1.3 Previous Jet and Shock Simulations

In the field of astrophysics, simulation is one of the most powerful tools available for testing hypotheses. Observationally, very few parameters, such as observation frequencies, may be changed; conversely, theoretical models are able to propose mechanisms that may be unphysical. The simulational approach to astronomy acts as a bridge, connecting the observational and theoretical aspects of the discipline, and providing observational predictions and theoretical constraints. In the following sections, we outline some of the most significant simulations of AGN jets and recollimation shocks (RSs); we also note whether a simulation is two-dimensional and assumes axial symmetry, or is a fully three-dimensional simulation.

1.3.1 Jet Simulations

Many simulations of astrophysical jets have been produced over the past few decades, one of the earliest being that of Scheuer (1974), outlining an extremely simple model for the transport of energy from an AGN to the hotspots in radio sources by relativistic jets. This work qualitatively explained the shape of a jet, and predicted that jets are radially pressure-confined, and that the expansion of the leading edge is limited by the ram-pressure of the IGM.

More recent simulations, by comparison, can make far more advanced predictions

CHAPTER 1

by utilizing the increases in computer processing capabilities. One of the key distinctions between the types of code that are used depends on the assumed importance of magnetic fields within the flow. In magnetohydrodynamical (MHD) simulations, the magnetic field is dynamically important, and able to physically affect the evolution of the flow; this is not the case in hydrodynamical simulations, for which the presence of any magnetic field is dynamically negligible. We will briefly outline the findings of some of the most significant jet simulations of each variety now; three of the simulations will also be discussed in greater detail in later chapters, due to their relevance to this thesis.

Hydrodynamical Simulations

We first mention the non-relativistic three-dimensional simulations of Williams & Gull (1985), in which a jet propagating into a stationary, homogeneous ambient medium was suddenly realigned, such that the injected fluid had a different velocity vector. This model makes multiple predictions, one of which being that shocks within jets would tend to be oblique (i.e. recollimation shocks), with Mach discs forming only rarely, in highly axisymmetric cases. In the same year, Smith et al. (1985) published two-dimensional, non-relativistic numerical simulations of a jet also piercing through a uniform, stationary ambient medium; the emissivity of the jet was assumed to be proportional to the density of the fluid, while the ambient medium was assumed to have no emission. While little attention is paid to the polarization properties of the emission, the total luminosity features of hotspots were able to be replicated by this work, such as the “twin wings” and “tail” often seen extending towards the AGN.

The code of Matthews & Scheuer (1990) was also for fairly sophisticated axisymmetric numerical simulations; these were able to passively advect a randomly tangled magnetic field with the flow of an evolving jet, and determine the spectral ageing of

CHAPTER 1

the plasma's relativistic electron population. In the model, the non-relativistic jet propagated into an ambient gas of equal pressure, with marker particles advected from the injection region; each marker particle had an associated parallelepiped vector-triad that was initially an orthogonal set of unit vectors. The distortion of the magnetic field at the particle's position was monitored through parallelepiped deformation. The dynamics of the flow were simulated first, and then the synchrotron emission was determined using the parallelepipeds. This approach gave results that quantitatively agreed with the observed polarization and brightness distributions, but strongly over-predicted fractional polarization. In Chapter 3, we describe the implementation of similar marker particles to monitor the evolution of an initially randomly tangled magnetic field in the simulations used in this thesis.

Duncan & Hughes (1994) produced a two-dimensional numerical, relativistic hydrodynamical code with the possibility of adaptive mesh refinement, and the simulations they presented were from jets injected into a stationary ambient medium of equal pressure, but a density ten times that of the jet. A selection of simulations with varying adiabatic indices and injection velocities were shown, each having the same general jet and bow shock morphology; it was found that slower jets have greater internal disorder, while changes in adiabatic indices had a more subtle effect on the jet structure. This code was modified so as to be able to handle three-dimensional systems (Hughes et al., 2002, wherein examples of precessed and deflected jets are shown); the code has been verified by testing the output for cases with known results, such as ensuring that axisymmetry persists for a symmetric inflow and ambient medium, and that it is able to accurately simulate one-dimensional relativistic shocks. The code by Hughes et al. is also of interest in this thesis, and will be more fully discussed in Chapter 2.

Magnetohydrodynamical Simulations

To examine the differences between the hydrodynamical and MHD results of a simulation, Mizuno et al. (2015) analysed the results of a two-dimensional MHD simulation in which four over-pressured, differently magnetized jets were injected into a stationary ambient medium with Lorentz factor $\Gamma = 3$. The first jet had no magnetization, and thus was hydrodynamical, while the other three jets had either axial, toroidal or helical magnetic fields. It is shown that, relative to the hydrodynamical case, the axially magnetized jet has stronger RSs and a larger variation in jet width; the toroidally magnetized jet, conversely have weaker shocks and a flatter radial profile. Predictably, the jet with a helical magnetic field lies on a scale between these two cases, the extent to which either dominates being dependent on the pitch angle of the magnetic field.

There have also been multiple MHD simulations performed with the aim to analyse the stability of AGN jets, such as was done by Porth & Komissarov (2015). The code used was a three-dimensional, relativistic MHD code where jets were injected into atmospheres of exponentially decreasing pressure p_{atm} , with distance from the jet base z . They show that for an atmosphere with $p_{\text{atm}} \propto z^{-2}$ or steeper, the jet rapidly expands, becoming causally disconnected across its width; this is suggested to be how jets remains stable on such great length-scales. It is argued that this explains the distinction between FR I and FR II active galaxies, with the former becoming collimated in the corona around the AGN, while the latter only become collimated much further out. This work provides excellent justification for assuming the existence of a disordered magnetic field within jets; instabilities that are shown to form within the “spine” of jet flows may lead to dissipation of the magnetic energy within that region, releasing radiation and kinetic energy, and randomizing the magnetic field structure.

CHAPTER 1

We briefly mention the work of Martí et al. (2016), which also presents a relativistic, two-dimensional jet simulation code. Simulations of jets with helical magnetic fields are produced with different levels of magnetization. Jets dominated by their internal energy, rest-mass energy, and magnetic energy are compared. One of the key findings is that high magnetization, in magnetically-dominated jets, tends to result in magnetic pinch instabilities; this provides constraints for the maximum possible magnetization present in AGN jets. Finally, we outline the work of Fuentes et al. (2018), from which axisymmetric, time-independent simulations may be obtained. The jets produced in this work are also characterized according to their dominant energy type (internal, kinetic, and magnetic), but the presence of a thin shear layer about the jet allows the formation of RSs within each energy type of model, as opposed to the findings of Martí et al. (2016), in which RSs only formed in jets dominated by internal energy. It is also found that a rotation of the EVPAs of stationary components within jets may be observed; it is suggested that this can be used to identify RSs in observations of astrophysical jets. This simulation code is discussed in more detail in Chapter 3, as its results are used within this thesis.

The simulations outlined here generally have ordered magnetic fields because the MHD approach requires extremely high resolutions to represent the disordered magnetic fields that observations lead us to expect (Murphy et al., 2013); this would result in a prohibitively large run-time if MHD code were to be used in this way.

1.3.2 Shock Simulations

There are two main ways a shock may be simulated: semi-dynamically and numerically. Semi-dynamical models represent the action of a shock through jump conditions in the fluid parameters, which gives a sharp edge to the shock. The shocked plasma is also assumed to cool rapidly, and to only emit near the shock, thus ignoring emission contributions from upstream and inter-shock regions. By

CHAPTER 1

assuming the shape of these shocks and making other simplifications, this approach is often less computationally expensive than the numerical approach.

Shocks may be more accurately represented by numerical simulations because their shapes, positions, and strengths are calculated, as opposed to being assumed. However, the use of ordered magnetic fields in many numerical simulations means that plasma compression due to a relatively weak shock, such as a recollimation shock, will have little effect on the polarization of synchrotron radiation.

For both the semi-dynamical and numerical approach to simulations, what follows is a brief time-line of some of the work done.

Semi-Dynamical Simulations

One of the earliest examples of this approach was used by Laing (1980), in which a randomly tangled magnetic field was compressed into a cylindrical shell; it was shown that for different viewing angles, a range of polarization profiles may be obtained. The high fractional polarization seen in many radio sources were shown to be a potential result of the radial compression on a randomly tangled magnetic field, replicating the polarization properties seen in filaments in the Crab Nebula, and other extragalactic radio sources.

Later work was done to specifically replicate the highly polarized, spatially unresolved radio knots observed in BL Lacertae (Aller et al., 1985); Hughes et al. (1985) produced a model that assumed that the emission came from a diverging plasma flow with a randomly tangled magnetic field and power-law spectrum of electrons. In order to accurately reproduce observations of the most recent knots, it was necessary to have a propagating planar shock, as well as radiation from the optically thin region and the optically thick surface. The propagating shock structure consisted of a contact discontinuity, flanked by both an upstream and downstream shock, one of which was assumed to be much weaker than the other, and thus radiatively

CHAPTER 1

negligible. The synchrotron emission for such a system was able to closely fit measurements of the total flux, polarized flux, and electric vector polarization angle (EVPA) of the knots, finding that moderate compression from a weak shock can produce high degrees of polarization.

Using a slightly simplified version of this model, Cawthorne & Wardle (1988) examined the polarization data for a knot in OJ 287. While attempting to model the knot as a simple ballistic component of the jet, it was found that the maximum Doppler shift possible for agreement between the apparent velocity and fractional polarization of the knot was less than the value determined by using the X-ray variability in OJ 287. When the knot was treated as a propagating planar shock wave, however, much larger possible Doppler shifts were obtained, in better agreement with the values required by the X-ray variability. As the emitting material propagates away from the shock faster than the pattern moves, the relativistic motion and light aberration effects cause the compression-plane to be closer to the observer's line of sight in this model.

Stationary, conical recollimation shocks, with a randomly tangled upstream magnetic field, were simulated by Cawthorne & Cobb (1990), who assumed that only the shocked material emits, and that upstream flow was parallel to the axis of the shock, suggesting a radially fixed flow. Using the results of Hughes et al. (1985) to determine the polarization from this shock, it was found that this structure may be able to explain some of the observed polarization distribution in BL Lacertae. Cawthorne (2006) built upon by this model by adding a jet-parallel component to the upstream magnetic field, and convolving the result with a circular beam, for comparison with observation of a knot in 3C 380. showing that that the polarization maps of a knot in 3C 380 can also be explained as being the result of conically shocked emission from a (predominantly) randomly tangled magnetic field. A few years later, the approach of Cawthorne & Cobb (1990) and Cawthorne (2006) was

CHAPTER 1

employed to replicate the observations of a stationary knot in 3C 120 (Agudo et al., 2012). It was found that the poloidal component employed by Cawthorne (2006) was unnecessary, as was a slightly converging upstream flow; the only necessary features were the randomly tangled upstream magnetic field propagating through a conical shock to reproduce total flux, polarized flux and EVPA maps.

As noted by Cawthorne et al. (2013), however, all examples of jets, be they in a laboratory or a computer simulation, show recollimation shocks as two oppositely-opening conical shocks, meeting at their vertices (or a flattened Mach disc). In order to simulate emission from the core of BL Lac object 1803+784, a model was used in which a plasma with initially disordered magnetic field propagates through a collimating conical shock, and then a decollimating conical shock. Many assumptions were made to simplify the model, such as the flow following linear streamlines, but it was found that such an unphysical system was still able to predict the polarized flux and EVPA map extremely well. This suggests that, as predicted by Daly & Marscher (1988), the high-frequency radio-cores of AGNs are the result of RSs.

Instead of treating a randomly tangled magnetic field as unresolved on the scale of the simulation, Marscher (2014) took a significantly different approach; having a large number of non-interacting cells of plasma, each with randomly oriented, uniform magnetic fields, on large scales the plasma would appear unpolarized. These plasma cells are advected downstream until they propagate through a conical shock, into a region of turbulence; here the plasma is randomly assigned a fixed component of turbulent velocity. As the plasma cells propagate through turbulent region, their synchrotron and inverse-Compton emissions are calculated, until they reach the downstream rarefaction front. Overall, it was found that while the model underestimated the γ -ray to X-ray luminosity ratio, many observational signatures of blazars were well replicated, e.g. the temporal evolution of total flux and linear polarization. This leads to the conclusion that the outbursts seen in many blazars may

CHAPTER 1

be as a result of an extended period of noisy excitation, as opposed to a dramatic, instantaneous event.

Numerical Simulations

Using a non-relativistic numerical simulation in which the density of the ambient medium eventually becomes inversely proportional to the distance from the base of the jet, Falle & Wilson (1985) used a hydrodynamical code to calculate the expected spacing of recollimation shocks for a flow injected into this atmosphere. This atmosphere was modelled after that surrounding M87, becoming less dense with distance from the injection nozzle. It was found that this provided a good replication of the spacing of the knots seen in the jet of M87; this supports the previous assumption that the jet may indeed be pressure-confined.

Gómez et al. (1995) performed two axisymmetric, relativistic hydrodynamical simulations of a jet formed from fluid injected into an atmosphere, one with a constant profile, and one decreasing in density with distance from the injection point. Calculations of their synchrotron emission assumed that the plasma contained a population of highly relativistic electrons and a dynamically insignificant, predominantly disordered magnetic field that had a small jet-parallel component. By including opacity effects, multifrequency total intensity maps were produced. The jet embedded in a constant ambient medium showed regular shock strength and spacings, and a fairly constant maximum jet radius, whereas the jet in the diffusing ambient medium showed an increasing jet radius and decreasing shock strength with distance from the jet base.

Later, Gómez et al. (1997) produced two-dimensional simulations of a velocity perturbation moving through a jet; the perturbation was comprised of a leading shock and a trailing rarefaction wave, and created by temporarily increasing the injection velocity of material at the jet base. Stationary RSs within the jet were seen

CHAPTER 1

to be temporarily “dragged” downstream as the perturbation passed through them, with slowly propagating reverse shocks being created by the interaction between the RSs and the perturbation’s rarefaction wave. Radio synchrotron emissions were determined by using a power-law distribution of electron energies, and assuming that the magnetic energy is proportional to the local particle energy density. The relativistic nature of the evolving system meant that it was also necessary to introduce a delay, accounting for the light travel-time; this resulted in low-level fluctuations in the long-term evolution of the apparent velocity and light curve decay, due to the perturbation interacting with the stable jet. The simulated maps showed the perturbation itself as a region of enhanced intensity moving downstream at apparently superluminal velocities.

With the intention of examining how “superluminal” features interact with the underlying jet, Agudo et al. (2001) presented two-dimensional relativistic simulations in which a velocity perturbation propagates downstream through a stable jet with a constant opening angle. It was shown that the perturbation causes instabilities to form as it passed through the jet material, triggering the formation of RSs in its wake. Simulated radio maps of synchrotron radiation were produced in the same manner as that of Gómez et al. (1997); these suggested that the RSs should be readily visible in observations, appearing to emit from the superluminal component, as opposed to the radio-core. The velocities of these RSs were found to increase with distance from the core, reaching apparently superluminal motions downstream, but always with velocities less than that of the perturbation and the jet flow speed.

Roca-Sogorb et al. (2009) also determine the expected synchrotron emission from an axisymmetric relativistic MHD jet code. Using an initially helical magnetic field (with pitch angle $\phi = 65^\circ$), the magnetization of the plasma was varied in order to investigate the role of magnetic the field in the dynamics and emissions of AGN jets. It was found that with an increasingly magnetized jet plasma, the predicted knot

CHAPTER 1

brightness decreased. This suggests that the level of helical magnetization within AGN jets is generally fairly low.

To investigate how the ambient medium, and obscuring torus, affect the observed properties of AGN jets, Fromm et al. (2018) performed two-dimensional special-relativistic hydrodynamical simulations of over-pressured and pressure-matched jets with respect to the ambient medium. The jets had relatively modest Lorentz factors $\Gamma = 1.15$, and a non-interacting, steady-state torus was inserted into the simulation once the jet had become stable. Simulated images of the total intensity from synchrotron emission (and the thermal absorption by the torus) were produced for jets embedded in a range of ambient medium and torus configurations. The conclusion drawn from these simulations is that it should be possible to distinguish between over-pressured and pressure-matched jets using observable properties, such as the core-shift.

1.4 The Necessity of Disordered Magnetic Fields

It appears to be a recent trend for simulations and models to assume that strongly ordered magnetic fields are embedded in the plasma of jets, whether the ordering is necessitated by a MHD approach, or freely chosen in hydrodynamical simulations. However, while there is certainly evidence that some level of order is present in AGN jets, is it required for the fields to be so highly ordered? On the contrary, it could be argued that a disordered field is often *required* to accurately replicate observations.

In some cases, work is done in which randomly tangled magnetic fields are employed, but their contribution is downplayed, as is the case with Zamaninasab et al. (2013), in which two magnetic field configurations, called “helical” and “alternative” fields, are used to model the jet in 3C 454.3. The “alternative” magnetic field is a composition of a poloidal component and a randomly tangled magnetic field that has been somewhat compressed, and thus ordered, by a shock. This configuration

CHAPTER 1

was able to reproduce the observed flux density and degree of polarization profiles observed in the jet, but had a rather poor fit for the rotation measure and EVPA distributions. The profiles from the “helical” field were consistently better fits with observed rotation measure, flux density and EVPA, and arguably the degree of polarization too; the problem, however, is the lack of emphasis placed on the fact that a component of randomly tangled magnetic field is *also* included. For a given pixel, the rest-frame synchrotron contribution from the disordered magnetic field j'_{rand} , as a ratio of the total emission j'_{tot} , is given by

$$\frac{j'_{\text{rand}}}{j'_{\text{tot}}} = \frac{f}{f + C \sin^2 \theta},$$

where the weighting of the randomly tangled magnetic field component $f = 0.45$, and θ is the angle between the helical magnetic field and the line of sight. The undisclosed constant of proportionality between the helical magnetic field component and its rest-frame synchrotron emission is C ; if we assume that $C = 1$, then the tangled component of the magnetic field will constitute anywhere between 31% and 100% of the emission at any given location.

In other instances, unreasonable assumptions are made to justify the absence of random magnetic field components, when many simulations suggest they ought to be present. For instance, Lyutikov et al. (2005) concludes that all jets must contain a poloidal core and toroidal sheath of magnetic field, which would lead to a high degree of cancellation in their polarized emission. This work represents the resulting degrees of polarization (up to $\sim 15\%$) as “fairly low”, while observationally this level of polarization is extremely high.

As mentioned in previous sections, Gómez et al. (1995) and Cawthorne (2006) included a significant component of disordered magnetic field to replicate observations, and Porth & Komissarov (2015) show that instabilities forming within the spine of the jet are able to generate randomly tangled magnetic fields. Models by

CHAPTER 1

Cawthorne & Cobb (1990) and Cawthorne et al. (2013) were able to replicate observations of knots in BL Lacertae and the core of 1803+784, respectively, using *only* randomly tangled magnetic fields and recollimation shocks.

In this thesis it is assumed that the magnetic field in a jet is significantly disordered, as suggested by the low degrees of polarization observed throughout jets, and the observed increase when jet material is shocked.

1.5 Recent Developments

In this section, we review some of the recent work with results that may greatly impact the future study of AGN jets, and have interesting implications.

1.5.1 Observations

Radio jets in radio-quiet quasars

Hartley et al. (2019) present e-MERLIN and European VLBI Network observations of radio-quiet source HS 0810+2554, in which clear jet activity is present. The associated jets are extremely faint, and are only visible due to extremely strong gravitational lensing of the source, which has an intrinsic flux density of only 880 nJy. This is the faintest radio source ever imaged, and also the best resolved radio-quiet source, imaged with VLBI to a scale of 0.27 pc. By modelling the lensing body, it was found to have a non-smooth mass distribution, and so was determined to be a substructure of dark matter. The presence of jets in a radio-quiet source supports the view that the same AGN mechanism can operate as the dominant source of radio emission, even in the least radio luminous quasars.

Event Horizon Telescope Observations of M87

At a distance of 16 Mpc, giant elliptical galaxy M87 is one of the best studied AGN, with jets spanning $\gtrsim 1.5$ kpc, at an angle of 14° to line of sight (Asada & Nakamura, 2012). Recently, M87 has dominated the news due to the efforts of the Event Horizon Telescope (EHT) Collaboration (2019), which was able to image the shadow of the black hole at the centre of M87 at a wavelength of 1.3 mm. Comprised of eight individual millimetre and sub-millimetre telescopes, the EHT was a global VLBI array, with baselines spanning 160 m–10, 700 km.

The compact radio source at the centre of M87 was resolved (at a scale of $25 \mu\text{as}$) to be a circular emission ring, with a diameter of $42 \pm 3 \mu\text{as}$ and an asymmetric brightness distribution, a factor of $\gtrsim 10$ brighter than the region it encircled. The images obtained were compared to general relativistic MHD simulations of a synchrotron emitting plasma, relativistically orbiting black holes with a range of masses and spin parameters; it was found that the images are consistent with predictions of strongly gravitationally lensed synchrotron emission from a hot plasma, orbiting near the black hole event horizon. The ring radius and ring asymmetry depend on black hole mass and spin, respectively; the black hole has been estimated to have a mass of $(6.5 \pm 0.7) \times 10^9 M_\odot$, and models suggest its spin vector points away from the Earth.

Sadly, the EHT configuration for these observations lacked the short-baseline coverage and dynamic range necessary to image the comparatively faint jet of M87, although this could potentially be remedied in future observations, with campaigns at 230 and 345 GHz already planned. With the capability to resolve temporally and spatially on event horizon scales, the EHT will be able to probe general relativistic effects in the strong-field regime and to study accretion and relativistic jet formation near the black hole boundary, which have previously been unobservable.

1.5.2 Simulations

Resolution’s Influence on Magnetically Arrested Disk Simulations

Using a general relativistic MHD code to simulate magnetically arrested disks around spinning black holes, White et al. (2019) compared the same system at different resolutions. It was found that convergent properties included the accretion rate, the jet’s energy-extraction efficiency (via the Blandford–Znajek process), the magnetic structure (in particular, the flux accumulated by the magnetically arrested disk), the resultant suppression of the magneto-rotational instability, and the general large-scale structure of the flow.

However, the spatial structure of the jet shows variation across the set of grids employed, as do the Lorentz factors; small-scale features of the turbulence are also not fully converged. Hence, for steady state simulations, one can expect the resolution to notably change the position and obliquity of any RSs that form within simulated jets. Further to this, modelling of synchrotron emission revealed that the light-curve variability also does not converge, decreasing with increasing resolution, even at the highest resolutions.

This work implies that the currently available cluster resources for general relativistic MHD simulations are insufficient for accurately representing the physics occurring across scales spanning from the accretion disk to the extended jets.

The Fanaroff–Riley Class Distinction

We have already briefly mentioned the work of Porth & Komissarov (2015), in which moderately magnetized and moderately relativistic jets were simulated; it was demonstrated that jets entering atmospheres with a pressure gradient $p \propto z^{-k}$ experience a causal disconnect between the inner core and outer sheath, assuming that $k \geq 2$. This disconnect allows the jet core to expand slower than the sheath, suffering local instabilities and dissipating energy, while the jet as a whole remains

CHAPTER 1

stable. Porth & Komissarov propose that the presence (or absence) of this disconnect, and the z-pinch instabilities in particular, may explain the difference between FR I and FR II sources.

Further to this, Gourgouliatos & Komissarov (2018) produced a range of simulations in which the jets are either of equal density to the uniform ambient medium, or they are underdense with respect to the ambient medium, which in turn has a decreasing density gradient with distance from the inlet plane. These simulations represent FR II jets within the pre-evacuated lobes, and FR I jets pushing through the IGM, respectively. They find that in the case of unmagnetized relativistic jets, their recollimation is followed by the development of the centrifugal instability, after which the jet becomes turbulent. It is suggested that the long-term stability of AGN jets is due to their rapid expansion, and that the Fanaroff–Riley classification division of radio sources is connected to the onset of instabilities near the RS, after which the jet becomes turbulent.

These works strongly suggest that the classification of a radio jet is more dependent on the ambient medium than any inherent property of the AGN, meaning that this is a good indicator of the environment surrounding the AGN.

Chapter 2

Three-Dimensional Simulations

In order to produce radiative transfer images for a jet with an initially disordered magnetic field, the three-dimensional, grid-based, relativistic hydrodynamic simulation code by Hughes et al. (2002, hereafter HuMiD) was kindly provided by Prof. Philip Hughes, in order that we may simulate the jets throughout this chapter. The HuMiD code assumes the fluid is an inviscid, compressible ideal gas with a constant adiabatic index that we choose to be $\gamma = 4/3$, which corresponds to the limit for a relativistic monotonic gas; the magnetic field is also dynamically unimportant. This code has been validated by comparing results with previous simulations, and evolving systems with known behaviours, such as the one-dimensional shock tube.

We aim to simulate the distortion of a randomly tangled magnetic field, in a statistical sense, in order to obtain the polarization properties of the associated synchrotron emission. This may be achieved by monitoring the size and shape of each fluid “element” throughout the simulation, under the assumption of magnetic flux freezing. It is noted that a fixed Cartesian coordinate system is used for these simulations, where the unit vectors $\hat{\mathbf{i}}$, $\hat{\mathbf{j}}$, and $\hat{\mathbf{k}}$ are parallel to the x -, y -, and z -axes respectively; we adopt the convention that jets are always injected into the simulation with some velocity $\mathbf{v}_0 \parallel \hat{\mathbf{k}}$.

2.1 Fluid Dynamics

The evolution of the simulation in the HuMiD code is governed by the Euler equations, which ensure that, in the observer's reference frame, the particle number density N , momentum density \mathbf{M} , and total energy density E are conserved for an inviscid, compressible flow. These relate to the rest-frame number density n and total energy density ϵ , via the following Lorentz transformations:

$$\begin{aligned} N &= \Gamma n, \\ \mathbf{M} &= \Gamma^2(\epsilon + p)\boldsymbol{\beta}, \\ E &= \Gamma^2(\epsilon + p) - p, \end{aligned}$$

for fluid with normalized velocity $\boldsymbol{\beta} = \mathbf{v}/c$, Lorentz factor $\Gamma = (1 - |\boldsymbol{\beta}|^2)^{-\frac{1}{2}}$, and Lorentz invariant pressure $p = (\Gamma - 1)(\epsilon - nm_0c^2)$, for particles of rest energy m_0c^2 . The relativistic Euler equations (e.g. Amsden et al., 1977) may be written as

$$\frac{\partial}{\partial t} \begin{pmatrix} N \\ \mathbf{M} \\ E \end{pmatrix} + \nabla \cdot \begin{pmatrix} \boldsymbol{\beta}N \\ \boldsymbol{\beta}\mathbf{M} \\ \boldsymbol{\beta}E \end{pmatrix} = \begin{pmatrix} 0 \\ -\nabla p \\ -\nabla \cdot (\boldsymbol{\beta}p) \end{pmatrix}. \quad (2.1)$$

Here the Euler equations are presented conservatively, i.e. they are of the form $\partial_t \mathbf{U} + \nabla \cdot \mathbf{F} = \mathbf{J}$, where the solution vector \mathbf{U} contains the conservation quantities, \mathbf{F} is the flux vector, and \mathbf{J} is the source term. While other, mathematically identical, forms of these equations exist, it is necessary for simulations that employ shock-capturing methods, such as the HuMiD code, that these equations are written in conservation form. In a shock-capturing simulation, the presence of any shocks come about naturally as a result of the general treatment of the fluid; if non-conservative equations were to be used, this may produce misplaced shocks, unstable solutions, and oscillations up- and downstream from the shock (e.g. Anderson, 1995).

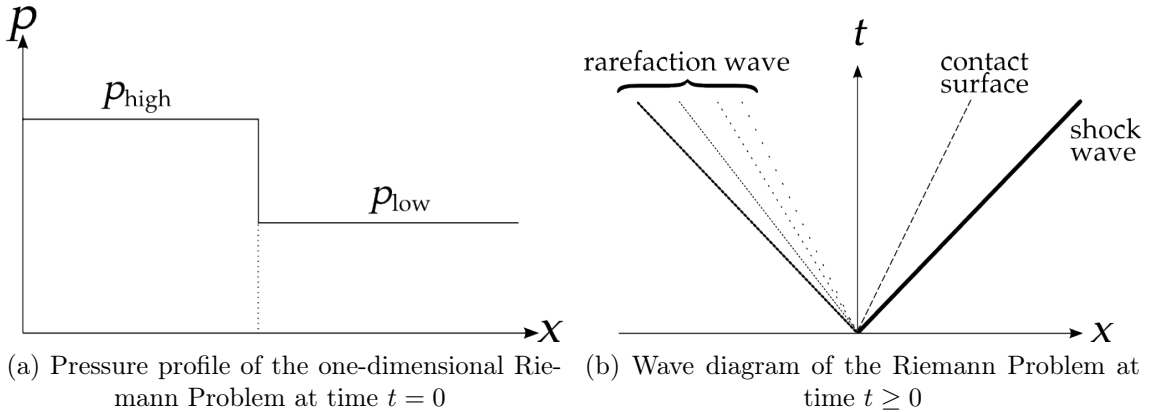


Figure 2.1: The Riemann Problem for a pressure discontinuity

2.1.1 Godunov Approach

For any field, continuous or discrete, that is sampled on a grid of finite spatial resolution, as is the case with HuMiD simulations, differences between the properties of any two adjacent grid points may be treated as a discontinuity. This discontinuity is analogous to the Riemann problem, in which a sealed, one-dimensional tube contains a diaphragm that separates the tube into a region of high pressure, and a region of low pressure (as illustrated by Figure 2.1a). At time $t = 0$, the diaphragm is removed, and at a later time $t = \delta t$ a perpetually widening rarefaction wave will have propagated into the high pressure region, while a shock wave will have propagated into the low pressure region, with a contact surface that separates two regions of discontinuous density (see Figure 2.1b).

In the Godunov approach, the exact solutions to the Euler equations are determined by decomposing the discontinuities between each cell interface into local Riemann problems, and the total fluxes are obtained globally by combining the local solutions across the whole system. When the fluxes of a system are known, it is then possible to determine how the whole system advances with time. However, this approach is only valid on the condition that none of the converging pairs of shock and rarefaction waves propagate far enough to interact with each other; this

CHAPTER 2

places limits on the time increment δt . The HuMiD code approximates relativistic solutions to Riemann problems by employing a Godunov-type solver based on the work by Harten et al. (1983), and later modified by Einfeldt (1988, henceforth HLL), in order to evolve the variable discontinuities at each grid cell interface for each iteration. The relativistic HLL approach neglects the contact discontinuity, replacing it, and the two constant states it separates, with a single piecewise constant state; this smears the contact discontinuity and results in some dissipation, but greatly increases the efficiency of any algorithm employing this method. In one spatial dimension, the part of the update due to advection of the solution vector \mathbf{U} of the Euler equations may be written as

$$U_i^{n+1} = U_i^n - \frac{\delta t}{\delta x} \left(F_{i+\frac{1}{2}} - F_{i-\frac{1}{2}} \right),$$

where the solution vector at iteration $n + 1$ is changed according to the fluxes F across the interfaces that bound the current cell i from its neighbours.

For a constant adiabatic index, the computation of n , ϵ and β reduces to the solution of the quartic equation

$$\left(\gamma |\beta| (E - |\beta| |\mathbf{M}|) - |\mathbf{M}| (1 - |\beta|^2) \right)^2 - (1 - |\beta|^2) |\beta|^2 (\gamma - 1)^2 N^2 = 0.$$

The HuMiD code solves this quartic at each cell several times during the update of a given mesh by using Newton-Raphson iteration, generally to second-order accuracy.

2.2 Boundary and Initial Conditions

Due to the finite nature of computational power, every simulation may only span a finite time and region; it is therefore also necessary to specify the conditions at any simulation boundaries, to define how material should evolve when impinging on

CHAPTER 2

such a surface. Depending on the initialization of a simulation, its evolution may be drastically different.

2.2.1 Boundary Conditions

There are two types of boundary condition employed in HuMiD simulations; five of the six boundaries have open boundaries, and the sixth surface is a fixed value boundary.

Open Boundary

The purpose of an open boundary is to allow fluid that impinges upon it to freely leave the simulation volume, such that it may be ignored thereafter. This is intended to produce the same effect as if the simulated flow were actually embedded within an infinite ambient medium, which is obviously computationally impossible.

The open boundaries in the HuMiD code are each two pixels thick, and their properties are duplicated from the two layers of pixels adjacent to each boundary, such that as the properties of the fluid impinging on them change, the boundary properties also change; this allows any outflowing material to leave the simulation unimpeded. This type of boundary condition is somewhat simplistic, and physically unjustified, but by having a large enough separation between these boundaries and the regions of interest, these issues can usually be neglected.

Fixed Value Boundary

The fixed value boundary (unsurprisingly) consists of cells with properties that are unchanging for the duration of the simulation. This boundary is the inlet plane for the jet and is also two pixels thick, with both layers having identical properties. The centre of the boundary has a circular region of radius r_{jet} , within which the jet is injected; beyond this radius, the boundary layer has the same properties as the

CHAPTER 2

initial ambient medium.

The properties that we initialize are the jet inlet radius r_0 , the jet velocity \mathbf{v}_0 , the densities of the jet and the ambient medium (ρ_0 and ρ_{amb} respectively), the pressure ratio between the ambient medium and jet (p_{amb}/p_0), and the relativistic Mach number $\mathcal{M} = \Gamma\beta_0/(\Gamma_s c_s)$, where the normalized initial velocity $\beta_0 = \mathbf{v}_0/c$, and the sound speed $c_s = \sqrt{dp/d\rho}$ has the corresponding Lorentz factor Γ_s . All simulations have the same initial relativistic Mach number $\mathcal{M}_0 = 8$ in this chapter.

2.2.2 Initial Conditions

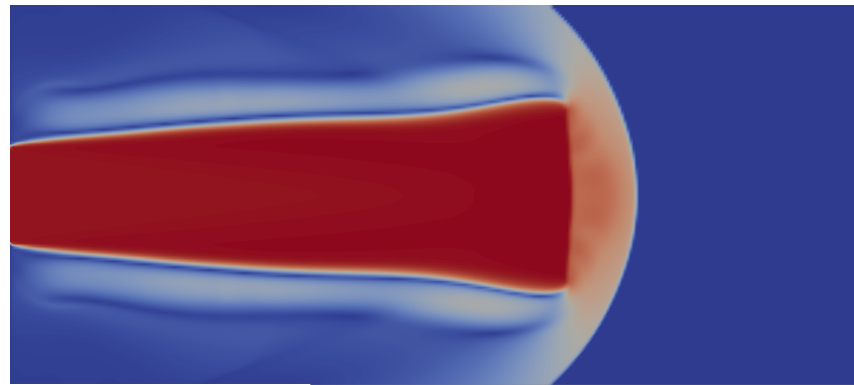
Two different schema have been used for initializing the simulations discussed in this chapter, and we discuss their differences here:

Punch Initialization

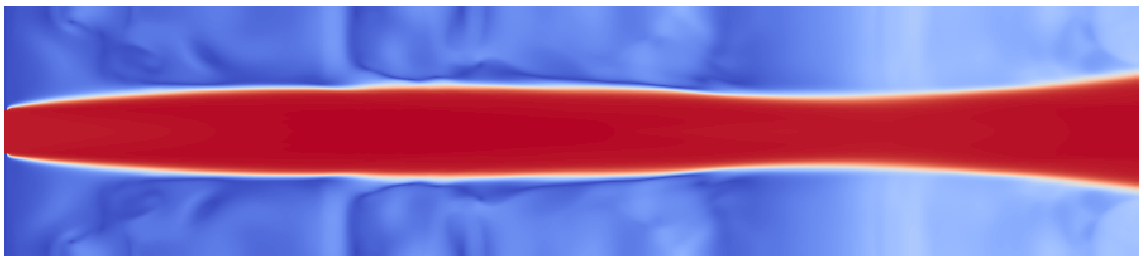
For the “punch” initialization (PI), the simulation is set to contain a stationary, uniform ambient medium of density ρ_{amb} , and pressure p_{amb} . After initialization, the jet must “punch” its way through the material filling the simulation volume, until it is able to propagate from the inlet boundary to the opposite open boundary. This initialization means that we make no assumptions about the final form of the jet, as we specify only the conditions at the inlet nozzle; however, it was found that the PI is sub-optimal for several reasons. For instance, the simulation will only reach a steady state after the jet has pushed its way across the entire length of the simulation, and then has had time to reach an equilibrium with the ambient medium. Another issue, illustrated in Figure 2.2a, is that a bow shock will readily form as the jet propagates from the inlet plane.

Depending on the shock strength and the size of the simulation volume, the bow shock can easily cover the entire x - y plane; as the jet propagates from the inlet plane to the opposite boundary, much, if not all, of the ambient medium is perturbed by

CHAPTER 2



(a) The normalized absolute velocity $|\beta|$ a “punch” initialized simulation. A strong bow shock is produced at the leading edge of the jet, which disturbs the entire volume of the simulation.



(b) The same simulation, at a later epoch, has displaced the ambient medium. The surrounding fluid can be seen to have transient structures.

Figure 2.2: The normalized absolute velocity profiles of a simulation at two different epochs are shown for a simulation using the punch initialization, wherein the jet must displace the ambient medium.

CHAPTER 2

this shock. This means that the transient features imparted by the shock, as can be seen in Figure 2.2b, require more time to diminish; a larger issue caused by bow shocks is that the properties of shocked ambient material will differ from its initialized state. While this makes it harder to produce a steady-state simulation with the parameters one is interested in, a bigger problem is that it tests our chosen method of monitoring the deformation of the fluid element volumes to the point where it is unreliable (see Section 2.6).

Spine Initialization

To reduce unnecessary computations, and prevent the formation of bow shocks the “spine” initialization (SI) was developed. The SI has a cylindrical jet of constant velocity (a “spine”) embedded in an ambient medium, spanning a region from the inlet plane to the opposite boundary. The properties of this initial jet, including radius, are equal to those of the inlet plane, but are still able to evolve with the simulation. This means that the fast flowing column at the centre of this simulation will reach equilibrium with the ambient medium sooner than for a PI jet, and without creating a bow shock. The key simulations used in this chapter are listed in Table 2.1, along with their initialization properties and elapsed times.

2.3 Flux-Based Parallelepiped Vector Monitoring

We aim to determine the polarization of the synchrotron radiation from the simulated jets, assuming an initially disordered magnetic field. This choice is motivated by the low polarizations observed in most astrophysical jets, which suggests a high degree of field disorder. Determination of polarization requires that we follow the distortions in shape of plasma particles as they flow through the simulation; to do this, we adopt the method devised by Matthews & Scheuer (1990).

To determine the synchrotron radiation produced by HuMiD simulation jets in

CHAPTER 2

Table 2.1: Hydrodynamical jet parameters in the injection plane

Simulation	ρ^*	p^*	β [c]	r_{jet}	t_{sim}	Init.	n_{xy}	n_z	δ_{xyz}
RES1	10.0	0.330	$0.9798\hat{\mathbf{k}}$	22	2222	PI	200	900	1.33
RES2	10.0	0.330	$0.9798\hat{\mathbf{k}}$	22	2176	PI	400	1800	0.665
PLN	1.0	0.330	$0.9798\hat{\mathbf{k}}$	25 [†]	Multiple [‡]	PI	20	100	1.33
GBOX	0.44	0.100	$0.96144\hat{\mathbf{k}}$	14.5	5291	PI	200	3800	1.33
CTRL	10.0	0.330	$0.9798\hat{\mathbf{k}}$	7.5	469	SI	50	300	1.33
XTND	10.0	0.330	$0.9798\hat{\mathbf{k}}$	7.5	469	SI	50	300	1.33
ORD1	10.0	0.330	$0.9798\hat{\mathbf{k}}$	10	1164	SI	200	1500	0.665

Notes: Tabulated data denote the jet model, density, pressure, velocity, and radius of the injected jet, elapsed time, the simulation’s initialization type, number of pixels in both the x/y and z directions, and the grid-spacing, in that order. Asterisked terms are a ratio between the jet- and ambient-value in the injection plane, and all lengths and times are given in simulational units, such that a photon travels unit distance per unit time.

[†] Injection occurs over the entire injection plane.

[‡] The average time elapsed per iteration $\bar{\delta}_t \approx 0.237$; PLN is shown at 60, 90 and 120 iterations in Figure 2.5.

the same manner as Matthews & Scheuer (1990) requires knowledge of the deformation of each emitting volume element. The approach taken by Matthews & Scheuer was to advect marker particles from the base of the flow, each with an associated vector triad that deforms with the flow. The marker particles are initially unit cubes, but subsequently evolve into parallelepipeds with shape that is monitored by their vector triad; the triads of vectors remain aligned with each of the three (initially orthogonal) edges of the parallelepipeds. The problem with advecting marker particles from the base of the jet, however, is that the final distribution of marker particles is entirely dependent on the jet flow, meaning that the distribution is likely to be uneven. This may lead to large errors from interpolating parallelepiped components over poorly sampled regions. Instead, we aim to evaluate the evolution of the parallelepipeds throughout the entirety of the simulated jet, with resolution equal to that of the hydrodynamical properties.

In the frame of the observer, we label the parallelepiped vectors $\mathbf{a}_{(0)}$, $\mathbf{b}_{(0)}$, and

CHAPTER 2

$\mathbf{c}_{(0)}$, where the subscript “0” denotes the value at initialization; to monitor the evolution of the parallelepipeds it is possible to advect each of these vectors with the fluid flow. From Matthews & Scheuer (1990), the advection of the i^{th} component of the observer-frame vector \mathbf{s} is given by

$$\frac{Ds_i}{Dt} = \mathbf{s} \cdot \nabla v_i, \quad (2.2)$$

where the substantial derivative is defined as

$$\frac{D}{Dt} \equiv \frac{\partial}{\partial t} + (\mathbf{v} \cdot \nabla). \quad (2.3)$$

Hence, from Equations (2.2) and (2.3) we obtain that

$$\frac{\partial s_i}{\partial t} = \mathbf{s} \cdot \nabla v_i - \mathbf{v} \cdot \nabla s_i, \quad (2.4a)$$

$$\implies \frac{\partial s_i}{\partial t} + \nabla \cdot (s_i \mathbf{v}) = \mathbf{s} \cdot \nabla v_i + s_i \nabla \cdot \mathbf{v}, \quad (2.4b)$$

where Equation (2.4b) is in its conservative form. This means that, in the same way the Euler equations may be evolved by the Godunov-type solver, to second-order accuracy, so too may the parallelepiped vectors. We always initialize the vector triads in their rest-frame such that

$$\mathbf{a}'_0 = \hat{\mathbf{i}}, \quad \mathbf{b}'_0 = \hat{\mathbf{j}}, \quad \text{and} \quad \mathbf{c}'_0 = \hat{\mathbf{k}},$$

where a prime indicates the value is in the rest frame.

2.4 Relativistic Motion Transforms

The parallelepipeds are initialized in the jet fluid’s rest-frame \mathcal{S}' , where they are initially cubic, but as the equations for evolution are formulated in the observer’s

CHAPTER 2

frame \mathcal{S} it is necessary to transform between the frames. From Jackson (1975), the following transform may be used to convert a vector from the observer's frame \mathcal{S} to its state in the rest frame of the fluid \mathcal{S}' , which moves with velocity \mathbf{v} to \mathcal{S} :

$$\mathbf{s}' = \mathbf{s} + \frac{\Gamma - 1}{|\boldsymbol{\beta}|^2}(\boldsymbol{\beta} \cdot \mathbf{s})\boldsymbol{\beta} - \Gamma\boldsymbol{\beta}t \quad (2.5)$$

where the position vector $\mathbf{s} = x\hat{\mathbf{i}} + y\hat{\mathbf{j}} + z\hat{\mathbf{k}}$ and time t give a point in the \mathcal{S} frame (space-time coordinates for the \mathcal{S}' are likewise declared with primed variables), and the Lorentz factor $\Gamma = (1 - |\boldsymbol{\beta}|^2)^{-\frac{1}{2}}$, where the normalized velocity $\boldsymbol{\beta} = \mathbf{v}/c$.

We can use Equation (2.5) to describe the transformation of vector \mathcal{A} , the endpoints of which are measured simultaneously in the \mathcal{S} frame, such that $\Delta t = 0$:

$$\mathcal{A}' = \mathcal{A} + \frac{\Gamma - 1}{|\boldsymbol{\beta}|^2}(\boldsymbol{\beta} \cdot \mathcal{A})\boldsymbol{\beta}. \quad (2.6)$$

If we take the scalar product of $\boldsymbol{\beta}$ with Equation (2.6), we obtain $\boldsymbol{\beta} \cdot \mathcal{A}' = \Gamma\boldsymbol{\beta} \cdot \mathcal{A}$, which, when substituted into Equation (2.6), gives the inverse transform

$$\mathcal{A} = \mathcal{A}' - \frac{\Gamma}{\Gamma + 1}(\boldsymbol{\beta} \cdot \mathcal{A}')\boldsymbol{\beta}.$$

2.5 Validating the Modified Code

After the equations for advecting the parallelepiped vectors have been incorporated into the HuMiD code, it is necessary to show that the simulations evolve as expected. In these HuMiD simulations the conservation of the density, momentum, and energy of the evolved evolving fluid are maintained in accordance with the Euler equations. From the conserved properties, the velocity and pressure of the fluid throughout the simulation may be calculated.

The original plan for this thesis was that the equations already present for parallelepiped advection would be verified, and then we could move towards an investigation of parameter space by producing a range of jets and calculating their radiative transfer.

2.5.1 Resolution Comparison

In order to verify the scalability of the HuMiD code, simulations RES1 and RES2 were produced; as Table 2.1 shows, these simulations are initialized identically, but the spatial and temporal resolutions of RES2 is double that of RES1. Cross-sections of the Lorentz profiles through simulations RES1 and RES2 (top and bottom panels of Figure 2.3, respectively) clearly show the convergence between the two simulations. We see a sharper recollimation shock and less blurring in the ambient material of RES2, but both simulations are clearly still evolving, as evidenced by the structure of the ambient medium. Regardless, it is clear that after the same amount of time has elapsed for both simulations, their general structure is the same, with the recollimation shocks being present in the same location. The strength of the shock is greater for the double resolution simulation, as can be more readily be seen in the top panel of Figure 2.4, which shows a more rapid decrease in the Lorentz factor across the recollimation shock. The bottom panel of Figure 2.4 generally shows steeper pressure gradients in the double-resolution simulation also, while maintaining the same general pressure profile.

2.5.2 Testing the Parallelepipeds with Planar Shocks

One method of verifying that the simulation of parallelepiped advection is accurate is by propagating a planar shock into an ambient medium of equal density, and comparing the density profile with the parallelepiped volume profile; we call this

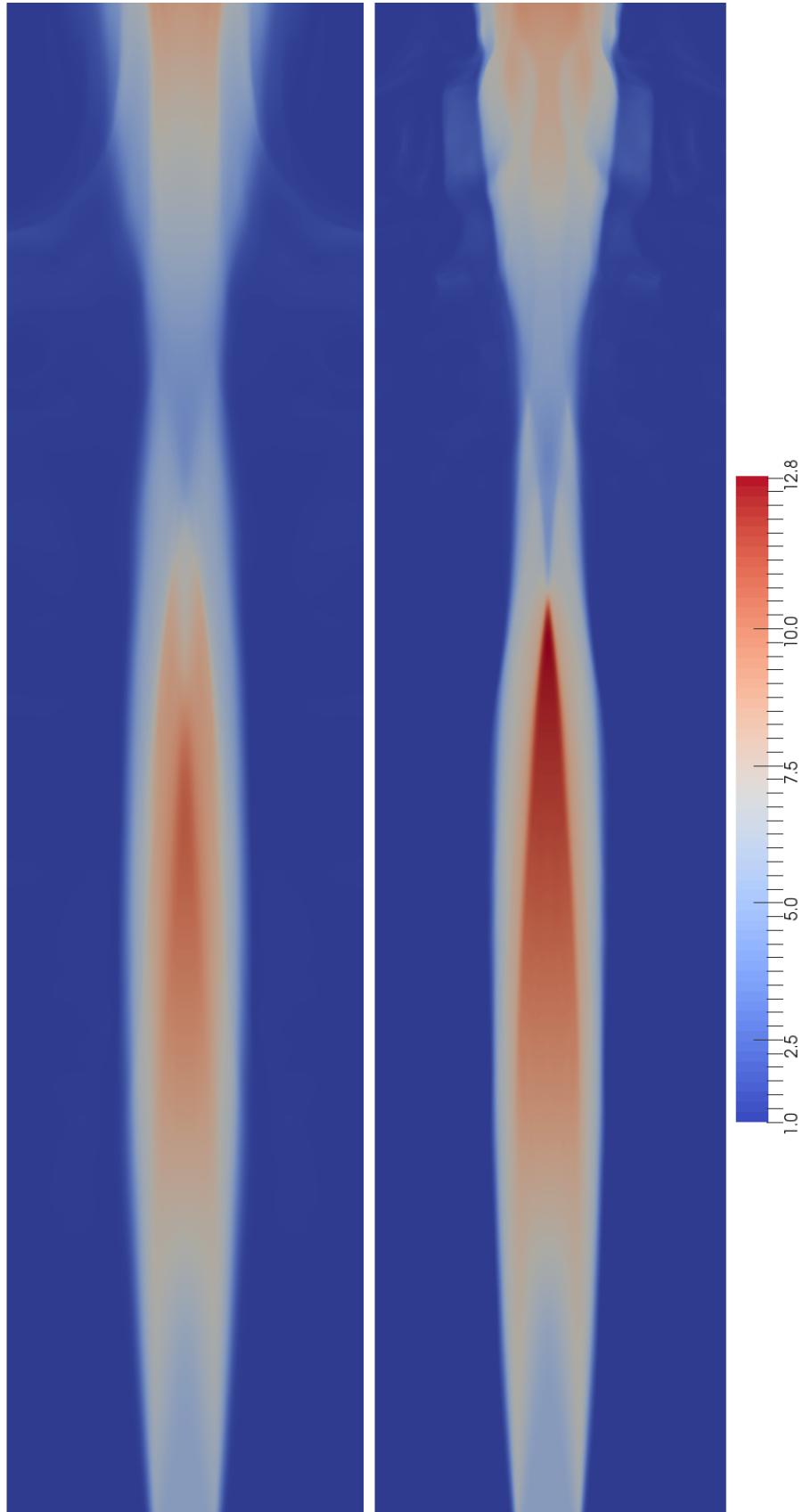


Figure 2.3: Lorentz factors for the cross-section of two simulations with standard (RES1, top) and double resolution (RES2).

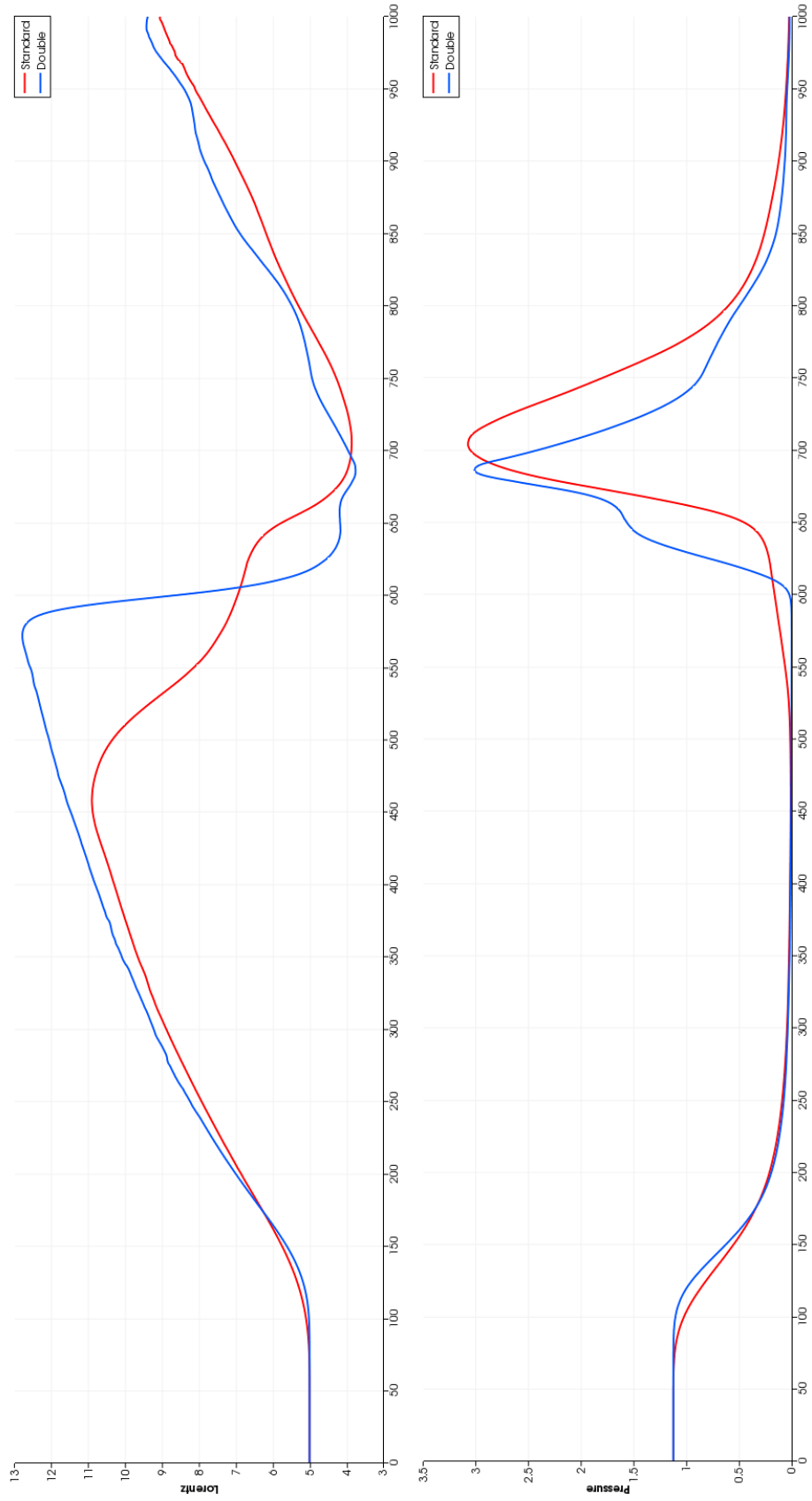


Figure 2.4: Lorentz factor (top) and pressure for simulations with standard (RES1) and double resolution (RES2), along the jet axis.

CHAPTER 2

model PLN, and its initialization properties are given in Table 2.1. For a parallelepiped described by the vector triad $\{\mathbf{a}, \mathbf{b}, \mathbf{c}\}$, the volume $V = |\mathbf{a} \cdot (\mathbf{b} \times \mathbf{c})|$; the compression is due to a planar shock in the x - y plane (the same plane as vectors \mathbf{a} and \mathbf{b}), propagating in the $\hat{\mathbf{k}}$ direction; this means that \mathbf{a} and \mathbf{b} are unaffected by the shock, such that the parallelepiped volume $V \approx |\mathbf{c}|$. Consider a fluid element with relativistic number density N and normalized velocity $\boldsymbol{\beta}$; from Equation (2.1), it is given that

$$\begin{aligned} \frac{\partial N}{\partial t} + \nabla \cdot (\boldsymbol{\beta} N) &= 0, \\ \implies \frac{\partial N}{\partial t} + (\boldsymbol{\beta} \cdot \nabla) N &= -N \nabla \cdot \boldsymbol{\beta}. \end{aligned}$$

From Equation (2.3), this becomes

$$\frac{1}{N} \frac{DN}{Dt} = -\nabla \cdot \boldsymbol{\beta}, \quad (2.7)$$

and the divergence of a fluid element's velocity (e.g. Anderson, 1995) gives

$$\nabla \cdot \boldsymbol{\beta} = \frac{1}{V} \frac{DV}{Dt}, \quad (2.8)$$

where V is the volume of a given group of fluid particles.

Combining Equations (2.7) and (2.8) gives

$$\frac{1}{NV} \frac{D}{Dt}(NV) = 0, \quad (2.9)$$

meaning that the mass within a given group of particles is constant. From Equation (2.9) we can see that the density and volume of the fluid are inversely proportional, and this is borne out in Figure 2.5, for which the density of a planar propagating shock is shown to be equal to the inverse of the local parallelepiped volume. As can be seen at each epoch, the density profile and the inverse volume

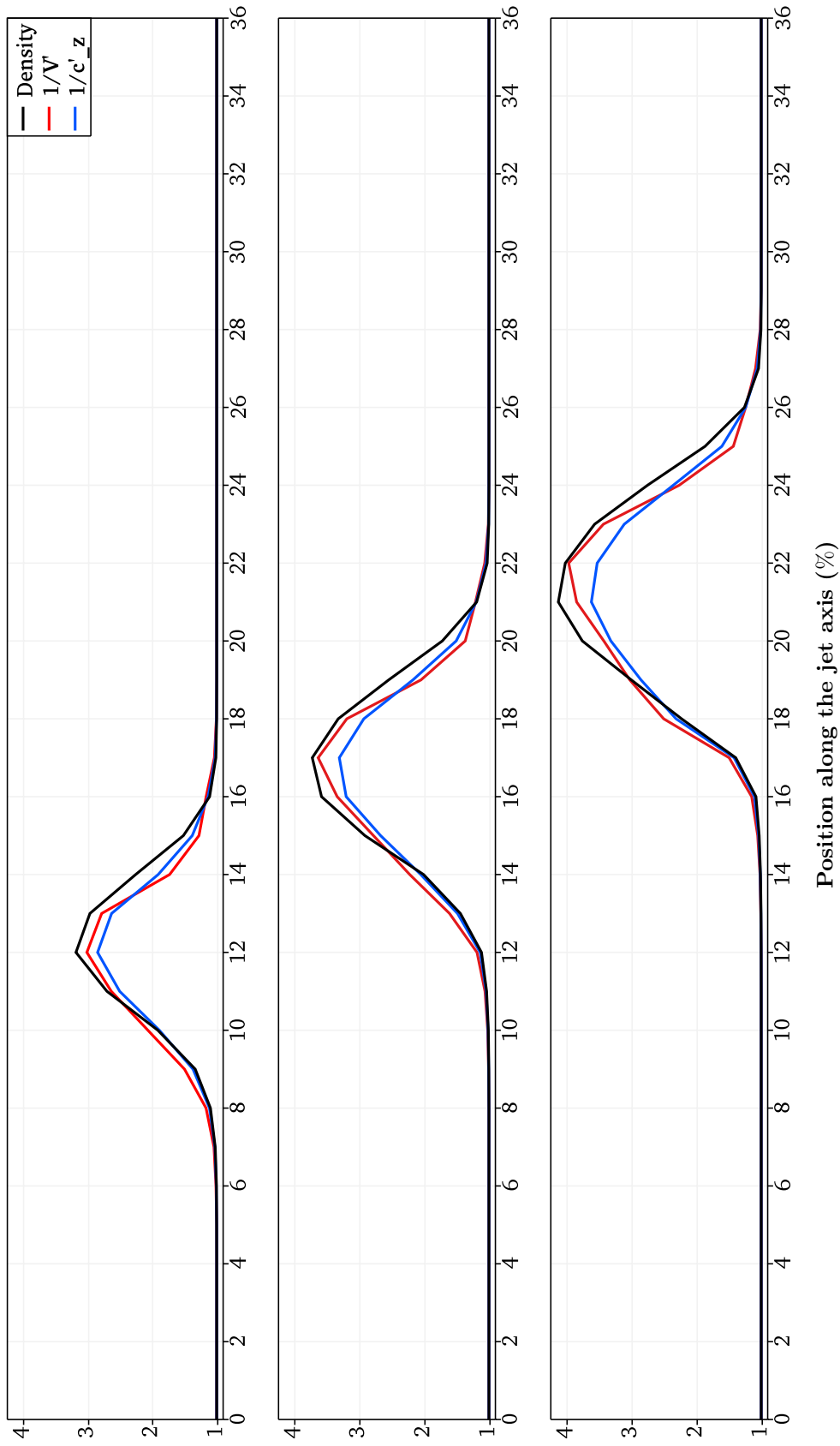


Figure 2.5: Comparison of the fluid density across the planar shock in simulation PLN for epochs at 60, 90, and 120 iterations (top to bottom respectively), as determined directly by the Euler equations, and as predicted by parallelepiped deformation.

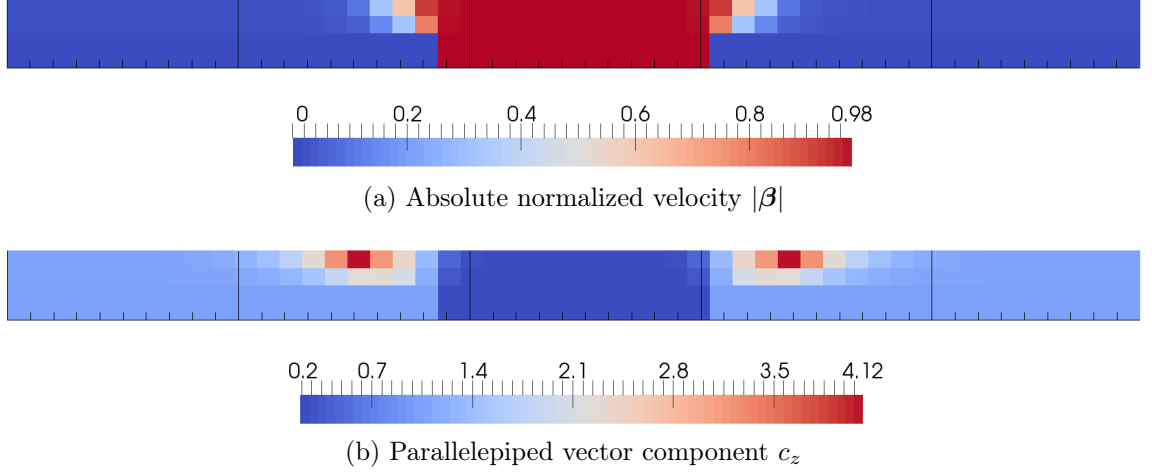


Figure 2.6: CTRL inlet boundary cross-section profiles of $|\beta|$ (top) and c_z .

profiles of each parallelepiped are equal to within 5.47% on average* for both the $1/V'$ and $1/c'_z$ metrics of determining the density.

2.6 Parallelepiped Evolution

It was found that, while the hydrodynamics of the code have been verified (Hughes et al., 2002), a significant amount of shear is introduced into the flow in the inlet boundary; e.g. see Figure 2.6, which shows that the parallelepiped vector component c_z was increased by a factor of $\gtrsim 20$ within two pixels of the base of the CTRL simulation. This occurs because there are discontinuities in the velocity and pressure of the jet and ambient medium in the inlet boundary; in turn, the volume-tracing parallelepipeds that were initialized in the inlet plane rapidly become excessively sheared due to the unrealistic nozzle conditions. The jet parallelepipeds near the shearing layer display unanticipated behaviours, such as the vectors \mathbf{a} and \mathbf{b} , which were initially in the x - y plane, becoming almost parallel to the jet axis.

In an attempt to minimize these effects, a separate fixed value boundary was

*This conservative estimate only includes pixels where $\rho \neq 1/V'$ or $\rho \neq 1/c'_z$; both the steadily flowing material, injected upstream of the shock, and the stationary ambient medium (downstream of the shockfront) have $\rho = 1/V' = 1/c'_z$. On average, the density differed from the $1/V'$ and $1/c'_z$ values by 5.99% and 4.94%, respectively.

CHAPTER 2

created, specifically for the parallelepiped vectors; by allowing the hydrodynamics of the simulation to evolve for a few pixels upstream from where the parallelepipeds begin to evolve, the level of shearing of the parallelepiped vectors due to the jet inlet is greatly reduced. This is readily visible upon inspection of Figure 2.7, the uppermost panel of which shows the Lorentz profile of simulations CTRL and XTND, which have the same hydrodynamical properties throughout (see Table 2.1); the fixed inlet boundary for the CTRL simulation includes the first two cells of the jet, while the XTND simulation has a boundary that fixes the parallelepipeds for the first ten pixels. The central panel of Figure 2.7 shows that, on-axis, $|\mathbf{c}|$ is much lower in the XTND simulation than in CTRL. While this is a significant improvement, it can be seen from the bottom panel of Figure 2.7 that the velocity after the recollimation shock is very constant, and certainly not changing with enough of a gradient to produce the strong increase seen in c_z .

2.6.1 Anomalous Parallelepiped Growth

It has been found that some parallelepiped components showed a general tendency to increase consistently, even though the velocity distribution suggested they should remain constant. A good example of this is shown by the GBOX simulation in Figure 2.8, which shows line plots along the jet axis of the axial components of velocity and the parallelepiped \mathbf{c} vector; the upper line plot shows these values before the recollimation shock, and the lower line plot covers the region downstream of this. The side panel shows the cross-section of the simulation's Lorentz factor profile. Prior to the RS, as expected, the axial velocity and parallelepiped component c_z remain fairly constant along the jet axis, close to their initial values; after the shock, however, the c_z component undergoes an increase many magnitudes larger than would be expected from the velocity profile, starting at $z \approx 720$. The steep increase in c_z thereafter is unexpected, however, as the velocity gradient parallel to

CHAPTER 2

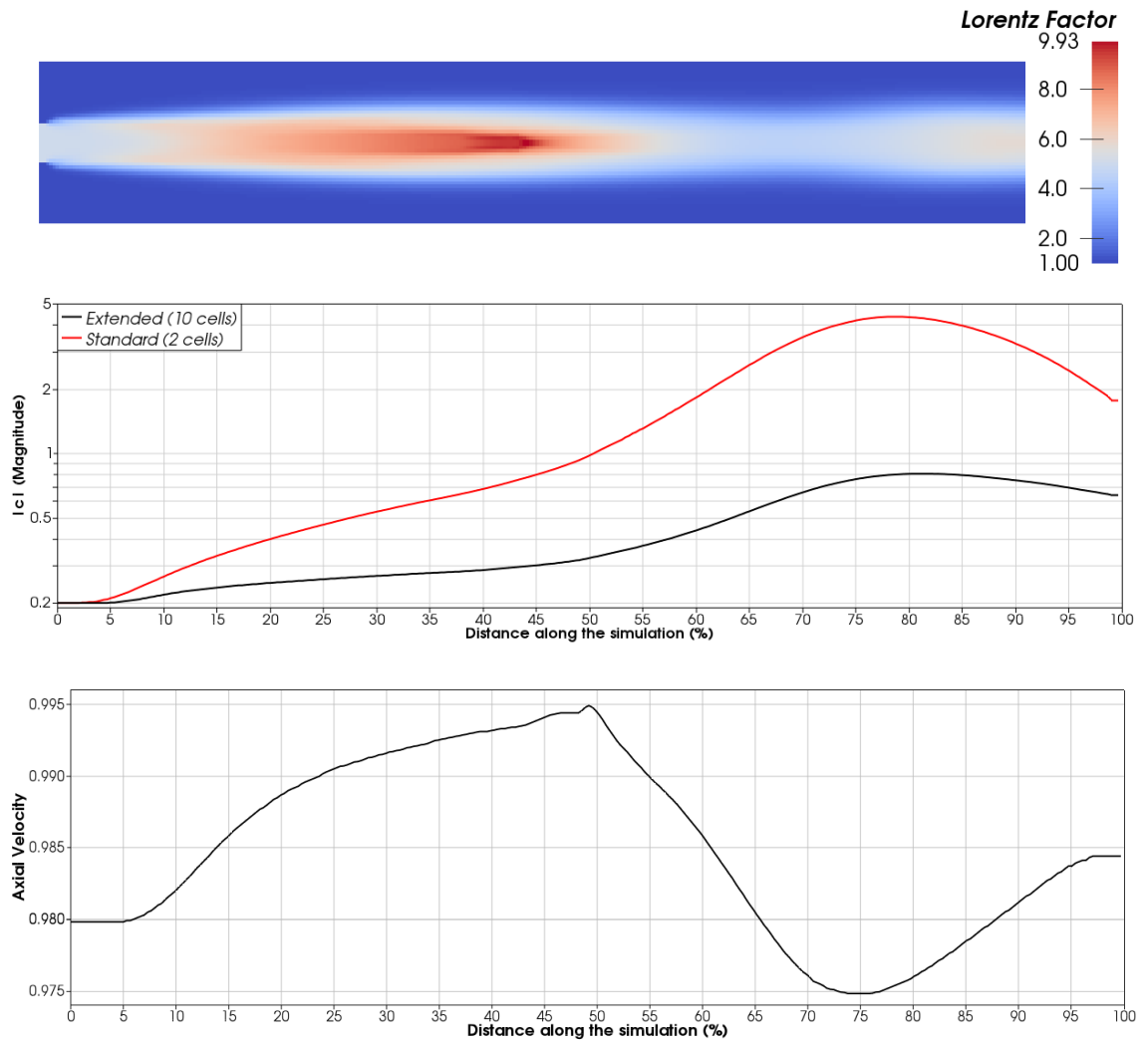


Figure 2.7: Cross-section of the Lorentz profile of a jet (top), the c_z profile along the jet-axis for standard (CTRL) and extended (XTND) thickness fixed parallelepiped boundaries (middle), and the axial β component along the same line.

CHAPTER 2

the jet is relatively small, and does not suggest such stretching of the parallelepipeds should occur. The a_z and b_z parallelepiped components were found to be similarly problematic.

A plausible explanation for the persistent problem near the inflow plane is that not only does the initialization of the jet flow establish a large shear, but the pressure mismatch between jet and ambient media causes the propagation of substantial pressure waves orthogonal to the jet axis. Such flow is of course also to be found downstream of recollimation shocks. In both cases, lateral flow will cause a growth in the \mathbf{a} and \mathbf{b} vectors, which in turn will be subject to shear. These highly localized structures are very poorly represented by the rather coarse Cartesian grids available to us, leading to a macroscopic growth in the parallelepipeds.

Indeed, a change in the parallelepiped vectors \mathbf{a} and \mathbf{b} that were assumed to be negligible in Section 2.5.2 is observed, and asymmetries associated with the finite resolution and boundary size of the Cartesian grid can be observed at a low level in the flow cross-sections (discussed in Section 2.7.2). It was decided that further quantification of these effects is not productive, as a detailed description of the unexpected growth in the parallelepiped vectors would not necessarily provide a path to mitigate the effects; for instance, if a much larger computational volume and higher spatial resolution are required, the necessary resources remain unavailable. However, it is necessary to confirm that the anomalous evolution of the parallelepipeds is not due to an error in the way that this was encoded. To this end we now consider an alternative method for evolving the parallelepiped vectors, and show that these problems persist.

2.7 First-Order Parallelepiped Vector Evolution

In light of the above discussion, we have determined the evolution of the parallelepiped vector components by a straightforward first-order implementation of the

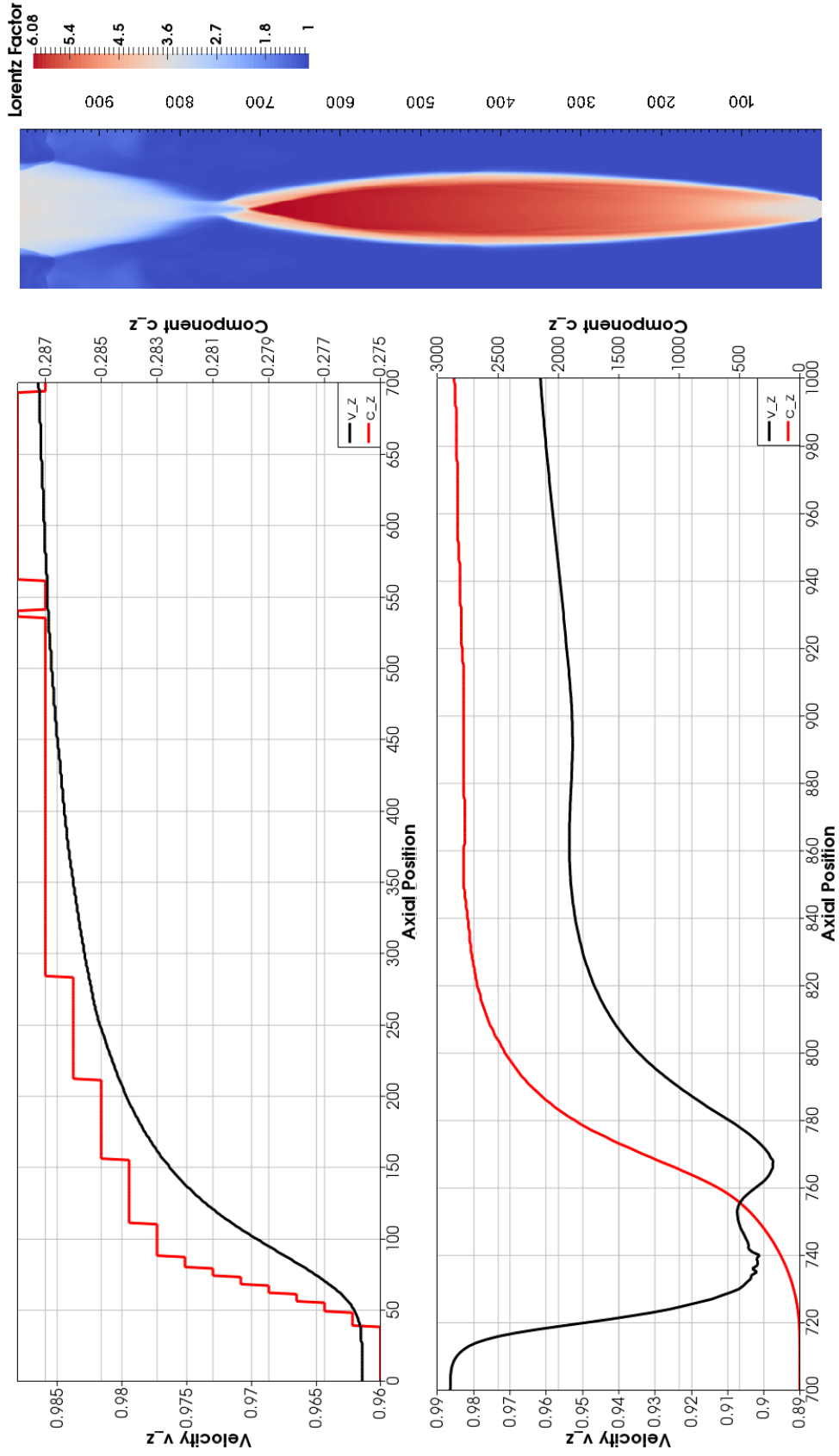


Figure 2.8: Cross-section of the Lorentz profile for part of the GBOX simulation (right). Two line plots of the axial components of velocity v_z and parallel velocity component c_z are shown along the jet axis before and after the recollimation shock (upper-left and lower-left respectively).

CHAPTER 2

advection equation. The partial derivatives of the parallelepiped vector components with respect to time can be expressed in terms of the velocities, the parallelepiped vectors themselves, and both their gradients, using Equation (2.4a). Then, for instance, a_x is simply updated from iteration n to $n + 1$, separated by a time period Δt , using

$$a_x^{n+1} = a_x + (\mathbf{a} \cdot \nabla v_x - \mathbf{v} \cdot \nabla a_x) \Delta t, \quad (2.10)$$

where the superscript denotes the iteration to which the variable corresponds, and, if absent, the current iteration n is assumed. We also only notate spatial coordinates which are not at the current position (i, j, k) , using square brackets, so $a_x^n(i, j, k) = a_x$, and $a_x^n(i, j + 1, k) = a_x^{[j+1]}$, for instance. The velocities are determined by the Godunov method, in a scheme that implements upwinding; such a scheme must also be employed in determining the parallelepiped evolution. Failure to take this precaution, and naively differencing the terms in the advection equation, led to rapidly oscillating instabilities of large and increasing amplitude. This is to be expected, of course, as it is well known that spatially centred finite difference schemes are unconditionally unstable for hyperbolic partial-differential equations (e.g. Edsberg, 2016), such as the Euler equations. Consider the gradient of a_x being taken in the x -direction, about the coordinates at (i, j, k) ; we would use $\partial_x a_x = (a_x^{[i+]} - a_x^{[i-]})/\delta_x$, where

$$i_- = \begin{cases} i - 1, & \text{if } v_x \geq 0 \\ i, & \text{otherwise,} \end{cases}$$

$$i_+ = \begin{cases} i, & \text{if } v_x \geq 0 \\ i + 1, & \text{otherwise.} \end{cases}$$

The same relations between the sign of v_y and y -coordinates j_+ and j_- , and the sign of v_z and z -coordinates k_+ and k_- also exist. This means that we calculate the

partial differential terms on the right-hand-side of Equation (2.10) as follows:

$$\mathbf{a} \cdot \nabla v_x = a_x \frac{v_x^{[i+1]} - v_x^{[i-1]}}{2\delta_x} + a_y \frac{v_x^{[j+1]} - v_x^{[j-1]}}{2\delta_y} + a_z \frac{v_x^{[k+1]} - v_x^{[k-1]}}{2\delta_z},$$

$$\mathbf{v} \cdot \nabla a_x = v_x \frac{a_x^{[i+]} - a_x^{[i-]}}{\delta_x} + v_y \frac{a_x^{[j+]} - a_x^{[j-]}}{\delta_y} + v_z \frac{a_x^{[k+]} - a_x^{[k-]}}{\delta_z}.$$

Unfortunately, this approach is found to be similarly beset by difficulties as encountered in the Godunov approach, even with the extended boundary condition for the parallelepiped components. This shows that the aforementioned problems are not the result of evolving the parallelepiped vectors in a hydrodynamic-like manner. Figure 2.9 shows colour plots of c_z in the y - z plane for CTRL and ORD1 in the top and middle panels, respectively. In CTRL it is shown that extremely large values of c_z up to ~ 60 occur, and in XTND it can be seen that the c_z profile has the same shape, but that the maximal value is lower. The effect of the extended boundary layer can be seen in the conical region of constant $c_z = 0.2$ at the base of the jet, and in the reduction of c_z by a factor of ~ 10 . The bottom panel of Figure 2.9 shows the v_z and c_z profiles of c_z for CTRL and XTND along the jet axis. This plot clearly shows that the c_z components in XTND are greater than those in CTRL, but that both have the same general profile, with c_z continuing to increase for CTRL and XTND after v_z begins to decrease.

2.7.1 Comparison with Streamline-Based Parallelepipeds

In order to check the accuracy of the first-order, direct-differencing approach, another approach was applied to obtain the parallelepipeds for the same simulation. In a similar manner to that of Matthews & Scheuer (1990), marker particles were advected with the flow to determine the parallelepiped vectors; this method is explained in greater detail in Chapter 3. The streamlines were determined for a jet that had settled to a steady state; in this case, fluid particles follow streamlines, and

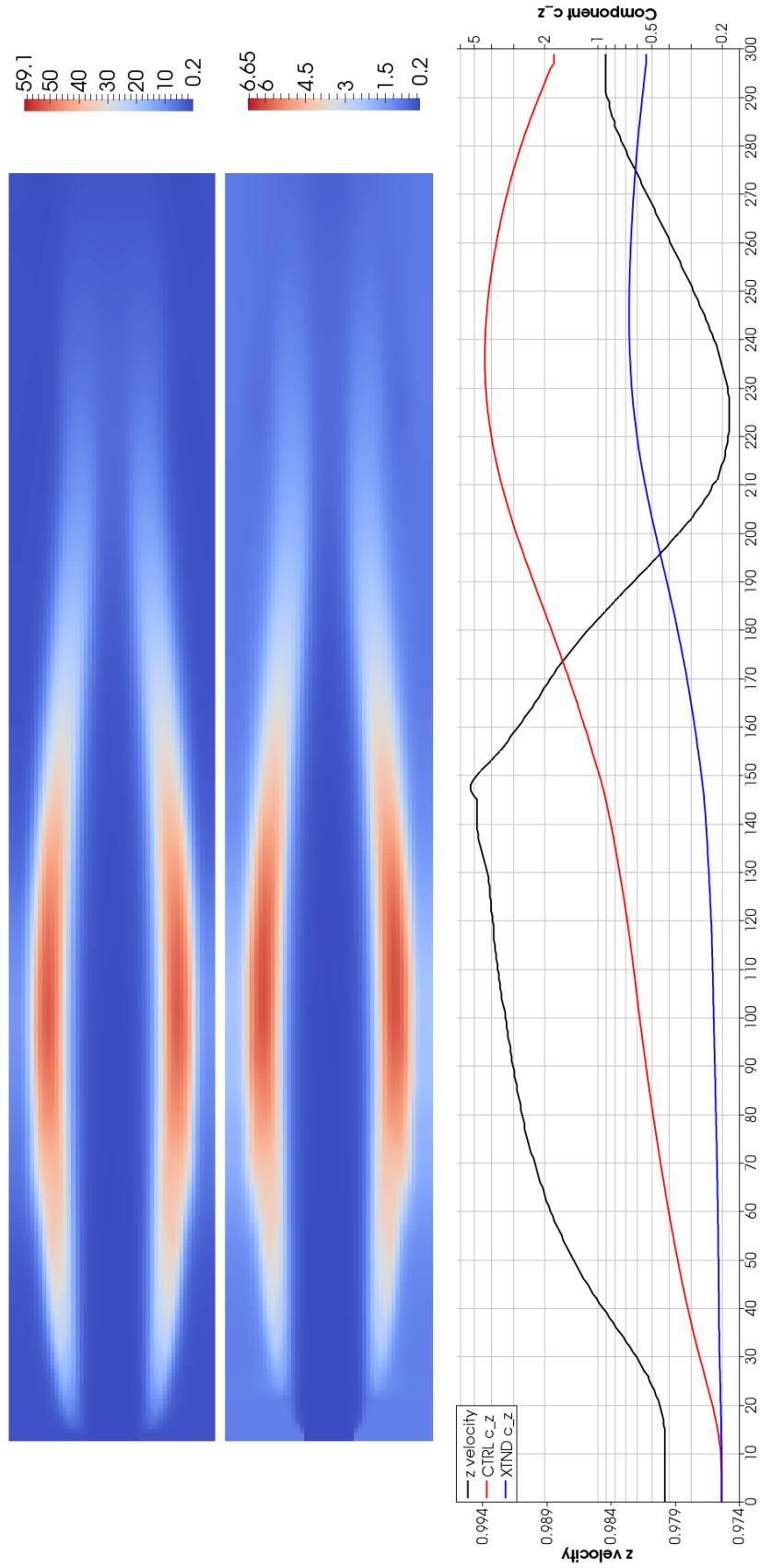


Figure 2.9: Parallelepiped component c_z is shown for the y - z plane through the centre of models CTRL (top) and XTND (middle). The bottom panel shows the on-axis values of v_z (left axis) and c_z (right axis) for the CTRL and XTND models.

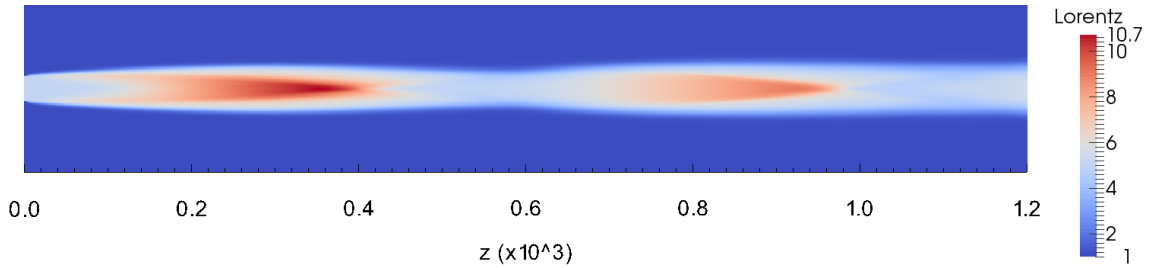


Figure 2.10: Lorentz factor profile of ORD1

the evolution of the parallelepiped vectors associated with each propagating marker particle may be determined from the steady state velocity field (see Section 3.3).

For simulation ORD1, both the first-order direct-differencing method for evolving the parallelepipeds, and the streamline-based method were used to determine the parallelepiped vectors throughout the simulation. The Lorentz factor profile of this simulation is shown in Figure 2.10, and Figures 2.11 and 2.12 show the parallelepiped vector components as a function of x -position, for $z = 249$ and $z = 499$ respectively, both 1.5 pixels above the y - z mid-plane, $x = 0$.

As can be seen from Figure 2.10, the first RS occurs at $z \approx 375$, and so the profiles in Figures 2.11 and 2.12 are taken before and after the shock, respectively. It can be seen that the parallelepiped component profiles in Figure 2.11 agree quite closely, especially closer to the jet axis ($x = 99.5$). After the RS, however, Figure 2.12 shows that many of the parallelepiped vector components determined via the direct-differencing approach are vastly different from those obtained via streamline-based methods; parallelepiped vector \mathbf{c}^* , and components a_z and b_z rapidly diverge from the values calculated by the streamline-based method especially quickly, while the other components remain in fairly good agreement until the shear-layer between the jet and ambient medium is approached.

*Components c_x and c_y tend to be very small, and as such, their discrepancies between the direct-differencing and streamline-based methods are less significant.

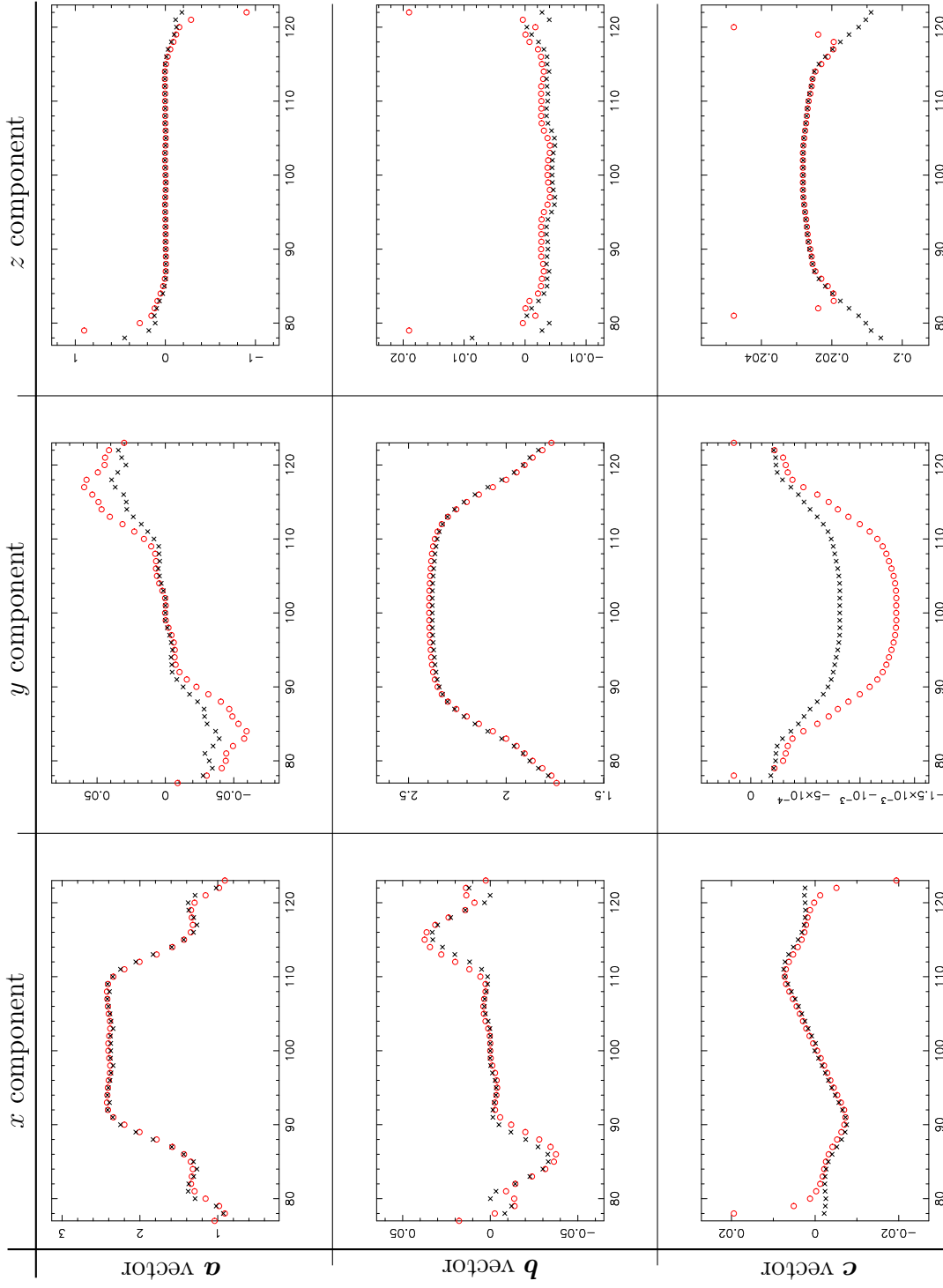


Figure 2.11: Comparison of ORD1 parallelepiped components, obtained by direct-differencing (red circles) and streamline-based methods (black crosses), as a function of x , at $y = y_{\text{mid}} - 1.5$ pixels and $z = 249$. Rows correspond to vectors \mathbf{a} , \mathbf{b} , and \mathbf{c} (top to bottom, respectively), and columns show the x -, y -, and z -components thereof (left to right, respectively).

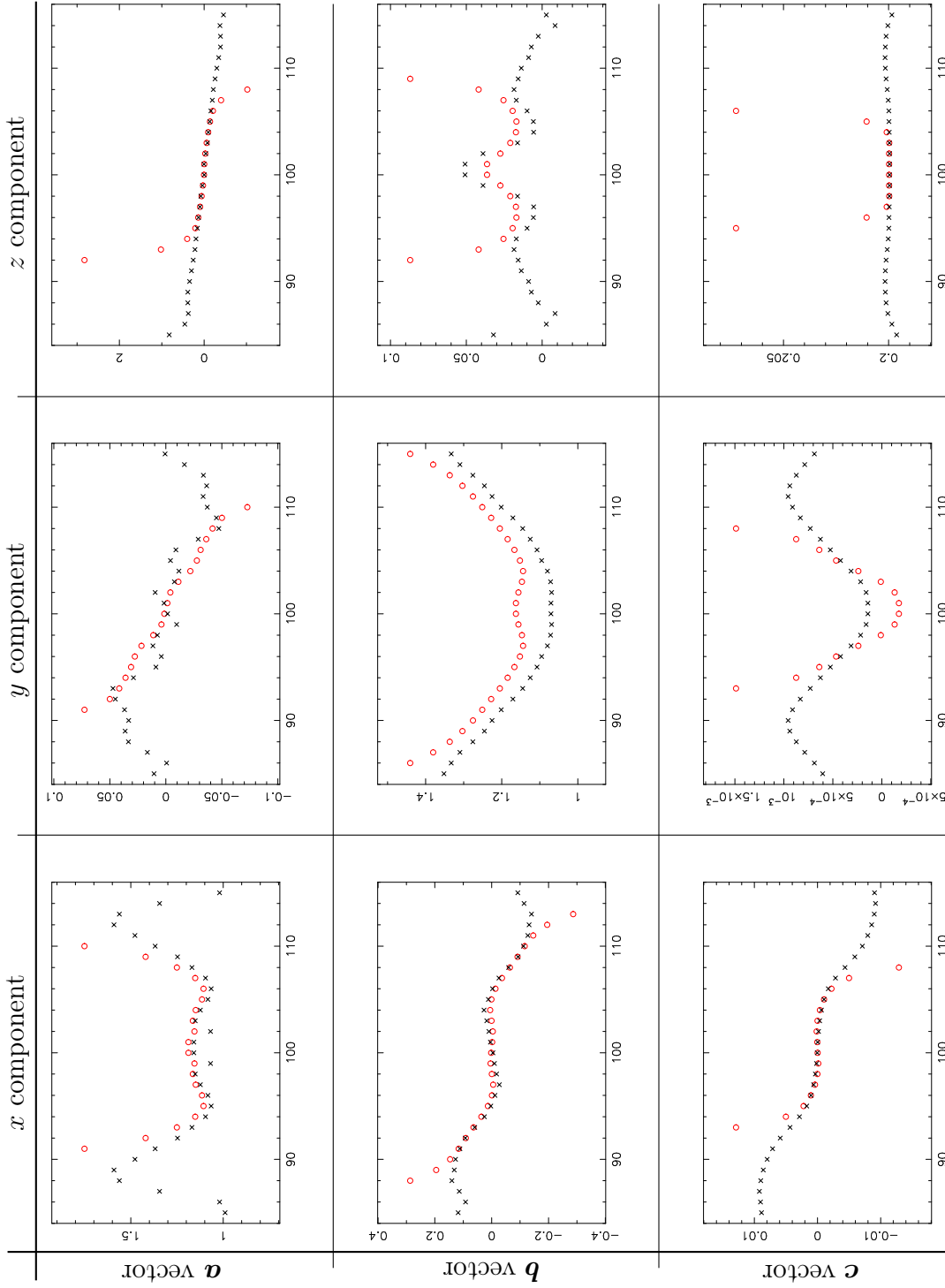


Figure 2.12: Comparison of ORD1 parallelepiped components, obtained by direct-differencing (red circles) and streamline-based methods (black crosses), as a function of x , at $y = y_{\text{mid}} - 1.5$ pixels and $z = 499$. Rows correspond to vectors \mathbf{a} , \mathbf{b} , and \mathbf{c} (top to bottom, respectively), and columns show the x -, y -, and z -components thereof (left to right, respectively).

2.7.2 Hydrodynamical Asymmetries

While employing a range of methods in an attempt to remedy the issues suffered by the parallelepiped vectors after the first recollimation shock, one factor was found to be irredeemable for the simulations that had evolved to a steady state. The use of a slice through the simulation volume in the x - z or y - z planes is an incredibly useful diagnostic, but when dealing with a system that has no symmetries imposed upon it, it is vital to ensure that the result is as expected from all vantage points. As the simulations advance, the cylindrical symmetry of the jets were found to become increasingly broken (e.g. Figure 2.13).

A range of attempts were made to reduce the severity of this issue, including realigning the centre of the simulation, doubling the resolution of the simulation, doubling the radial size of the simulation volume, and running the simulation for a greater number of iterations. None of these exercises resulted in greater cylindrical symmetry, suggesting that the additional resolution required is far beyond what was available to us, and greater simulational run-times significantly worsened the issue.

2.8 Summary

This chapter represents a very condensed summary of the work performed during the first 2.5 years of the PhD. Although no scientific results were obtained, it is included here in order to explain the strategy adopted in the following chapters of this work. We found that when determining the advection of the parallelepiped vectors, via the Godunov and direct-differencing approaches to Equation (2.4), the parallelepiped vector components experienced anomalous growth after the first recollimation shock. The parallelepipeds were found to agree quite well with those determined via streamline-based methods before the first shock, and only close to the jet axis thereafter; the anomalous growth issues remained unresolved, and so it

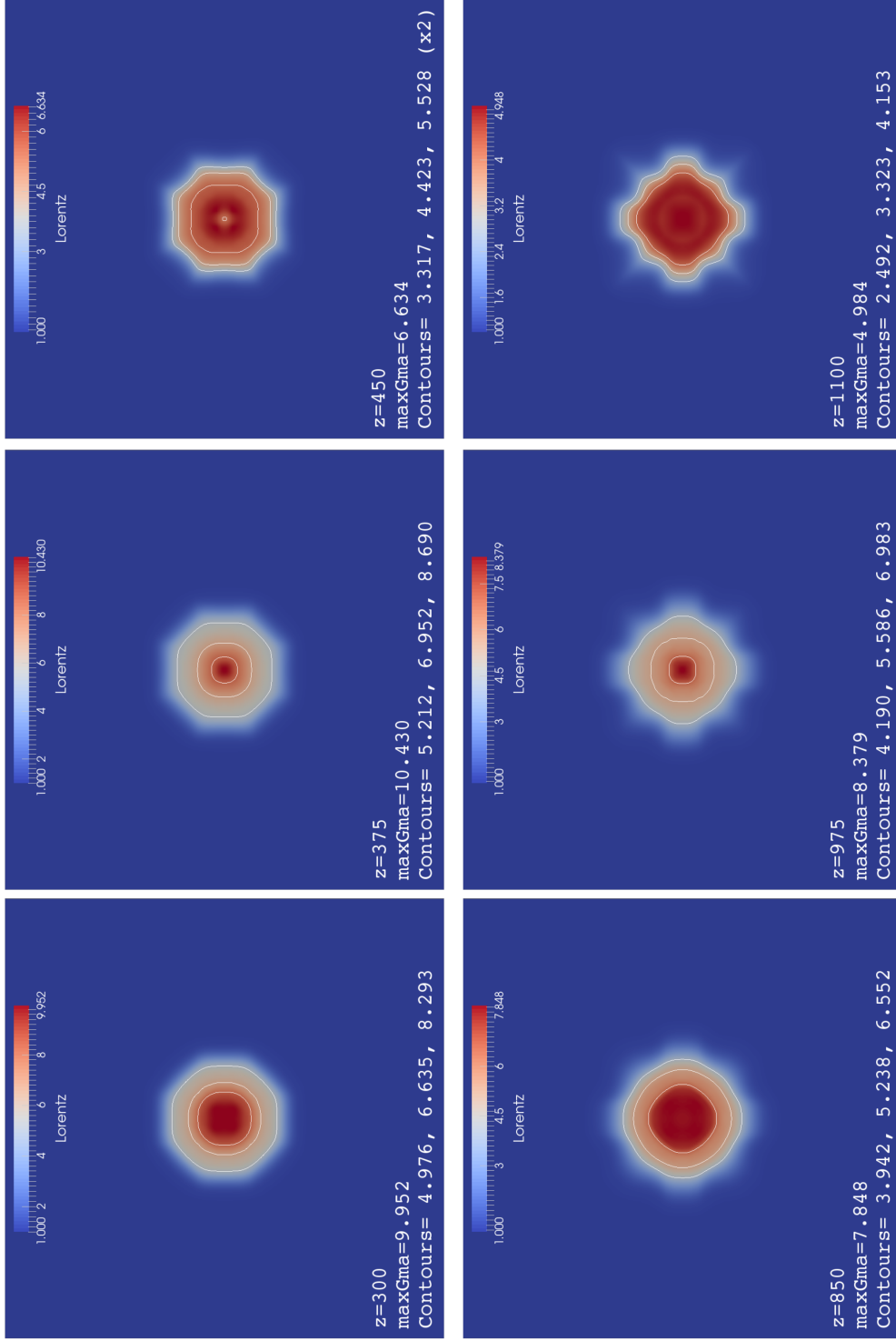


Figure 2.13: Cross-sections taken about the first two recollimation shocks in simulation ORD1, showing the Lorentz factor profiles, with contours Lorentz factor over-plotted at three-, four-, and five-sixths of Γ_{\max} —the largest Lorentz factor present in each x - y slice. The columns show slices prior to-, mid-, and post- recollimation shock (left to right, respectively), and the top and bottom rows correspond to the first and second shocks, respectively.

CHAPTER 2

was determined that any parallelepipeds obtained from HuMiD simulations would have to be calculated from streamline-based methods. The Godunov solver in the original HuMiD code has been verified via a range of tests, and the code to evolve the parallelepiped components via the Godunov solver was functionally identical to that for evolving the hydrodynamic variables (with the addition of source terms in their advection equations). The parallelepiped components determined via this approach, and the (Godunov-independent) direct-differencing method, were both found erroneous; hence, we are able to conclude that this is neither the equation implementations nor the Godunov solver at fault.

It was also found that the azimuthal symmetry of the jet was broken for simulations in which the flow had evolved to a steady state. Increasing the resolution and run-time of the simulations were found to make no difference to the symmetry.

We suggest that the simulations were executed with inadequate resolution, as an insufficient computational domain will lead to anomalous structures in the hydrodynamics, and these structural artefacts also drive the aforementioned mis-evolution of the parallelepipeds. With further routes of investigation using the HuMid code being closed to us, other methods were pursued.

Chapter 3

Axisymmetric Simulations: Methods

After the difficulties discussed in the previous chapter, it was decided to employ a “quasi-one-dimensional”, axisymmetric, time-independent code for simulating jets to perform radiative transfer calculations upon. The simulations discussed henceforth were produced by the relativistic magnetohydrodynamical (MHD) code of Fuentes et al. (2018, FGMP from now on), and were kindly provided by Prof. José-María Martí. Clearly, because the simulations are pre-existing and time-independent, the parallelepipeds required for radiative transfer will be determined post-processing.

The azimuthally-independent simulations produced by the FGMP code contain overpressured, narrow jets with steady, axisymmetric flows and highly relativistic speeds parallel to the jet axis. This code uses the findings of Komissarov et al. (2015), wherein it was shown that jets of this nature are well approximated by time-dependent, one-dimensional simulations, the temporal dimension of the latter acting as the axial dimension of the former. This approximation holds for both magnetized and unmagnetized relativistic flows in which axial velocity component is dominant, and close to the speed of light; if the magnetic field is dynamically significant, then the radial magnetic field strength must also remain very small throughout, in comparison with the local axial and toroidal magnetic field strengths. The models we use have a negligible component radial magnetic field throughout, and thus each

Table 3.1: Parameters of MHD jet models in the inlet plane

Simulation	$\epsilon [c^2]$	$\mathbf{v} [c]$	\mathcal{M}_0	p_{tot}^*	$\mathcal{B} [\%]$	B_ϕ/B_z	B_ϕ peak
J105	10.3	$0.950\hat{\mathbf{k}}$	3.5	2.05	1.51	28.7	smooth
J106	1.2	$0.950\hat{\mathbf{k}}$	6.0	2.29	9.39	4.6	smooth
J109	0.3	$0.950\hat{\mathbf{k}}$	10.0	2.05	1.51	45.5	smooth
J119	10.0	$0.950\hat{\mathbf{k}}$	3.5	2.01	1.04	1.4	smooth
J206	10.3	$0.950\hat{\mathbf{k}}$	3.5	2.06	2.27	6.6	sharp
J228	10.1	$0.950\hat{\mathbf{k}}$	3.5	2.01	1.20	1.8	sharp

Notes: Tabulated data denote the jet model, specific internal energy, velocity, initial relativistic Mach number, and total pressure at the centre of the jet inlet plane, and the maximum ratio of magnetic-to-gas pressure, the ratio of peak azimuthal and axial magnetic field components, and the shape of the B_ϕ inlet profile, in that order. Values are given to a maximum of three significant figures, and columns with * denote that the term is a ratio between the value at the jet axis, and in the ambient medium.

satisfy these requirements.

3.1 The Simulation Suite

Since in a steady flow, marker particles follow streamlines, our plan is to use the velocity profiles in steady state simulations to follow the trajectories of the corners of fluid volume elements, and hence to record their evolution in shape due to expansion, compression, and shear. The simulations chosen are all “weak field” cases, in which the magnetic pressure is much less than the gas pressure. In this case, the field structure is shown to have a negligible effect upon the kinematics of the flow (see Section 3.1.2). We therefore assume that the injected magnetic field is both weak and disordered, and then adapt the work of Matthews & Scheuer (1990) to determine the changes in the Stokes parameters (defined in Section 3.2.1) of fluid volume elements as they evolve during their journey through the jet.

The simulations we use are similar to each other in most regards, and their properties in the inlet plane are given in Table 3.1. Models J105, J119, J206 and J228 have different magnetic field configurations, but are all dominated by their

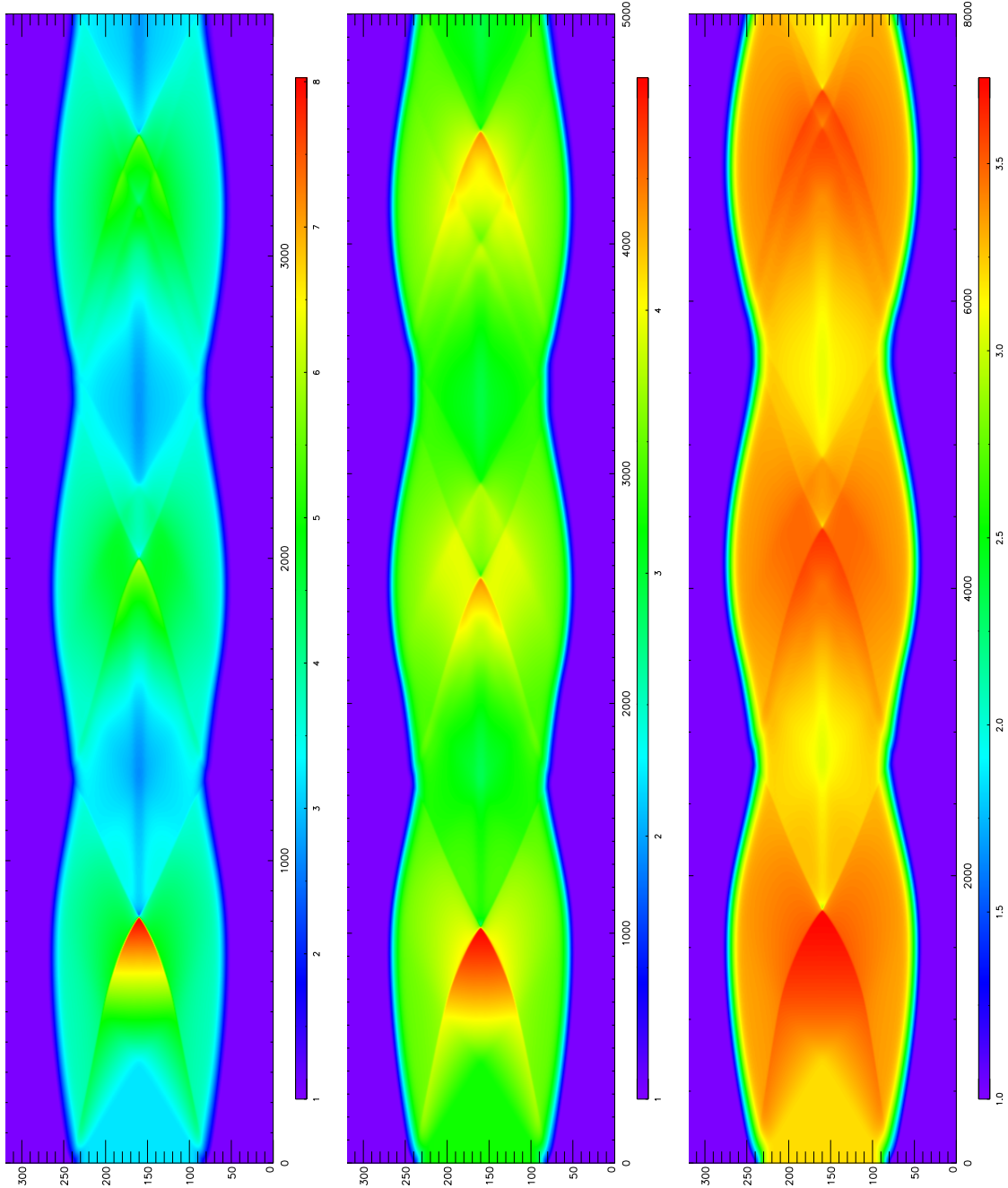


Figure 3.1: Lorentz factor profiles of models J105, J106 and J109, in that order from top to bottom.

CHAPTER 3

internal energy; these are classified as “hot” jets, and we show in Section 3.1.2 that these models contain jets that are almost indistinguishable from kinematical and geometrical perspectives. Jet J109 is a “cold”, kinetically dominated model, and the jet in J106 is intermediate between these two states. Each of the jet models we use has a low ratio of magnetic-to-gas pressure $\mathcal{B} \sim 1\%$.

Each of the simulations has the same resolution in the r - z plane, extending 160 pixels in the radial direction, and 8000 pixels along the jet axis. The Lorentz factor profiles of the first three recollimation shocks (RSs) in the jets of J105, J106 and J109 can be seen in Figure 3.1, each panel with independent aspect ratios and colour-bars. It must be emphasized that the RSs form with greater obliquity and lower separation in the hotter models; these jets have lower relativistic Mach numbers (see Table 3.1), and thus react more rapidly to environmental changes, resulting in a greater range of Lorentz factors within the flow. The fluid of kinetically dominated J109 is able to reach approximately the same speed upon arriving at each RS front due to the relatively weak nature of these shocks; the hotter jets, however, have stronger RSs and achieve significantly lower Lorentz factors upon reaching each successive RS. We assume that only material from within the jet produces synchrotron radiation, and we “trim” the jet based on the flow-speed in the inlet plane; while the inlet velocity $\mathbf{v} \geq 0.999\mathbf{v}_0$, where \mathbf{v}_0 is the on-axis injection velocity of the jet, the fluid is considered to be part of the jet. From the outermost point where this relation holds, we advect a streamline, and consider the points internal to this boundary to be part of the jet.

3.1.1 Azimuthal Velocities

Throughout the simulation, non-zero azimuthal velocities $v_\phi \ll |\mathbf{v}|$ are present, which result from the small Lorentz forces within the low magnetization jet. We choose to neglect these velocities, which would be absent in a fully hydrodynamical

CHAPTER 3

simulation, and interpret them as an indicator of the magnitude of errors in the axial and radial velocity components.

Regardless, a particle in an axisymmetric flow with azimuthal velocity v_ϕ , at a radius R , for duration T experiences $v_\phi T / (2\pi R)$ full rotations. Without determining the streamlines at this stage, we assume a particle is advected to each pixel in the R - z plane via a streamline of constant radius, with constant axial and azimuthal velocities, equal to those of the destination pixel. The duration T is assumed to be equal to the ratio of the pixel's z -position and v_z . Applying this to model J106, we obtain Figure 3.2; the upper panel shows the azimuthal velocity profile, and the lower panel shows the number of complete rotations for each pixel. In this approximation, we assume a constant rate of rotation along each streamline, meaning that the pixels with the greatest v_ϕ will overestimate the actual rotation of a particle advecting to that point. The largest theoretical rotation produced is found to be $\sim 2\%$ of a complete rotation, but this is an overestimate; it can be seen that within each RS, azimuthal rotation in one sense at the collimating part of the shock is often followed by rotation in the opposite sense at the decollimating part of the same RS. Hence, the total rotation experienced by a particle advected through simulations with such small azimuthal velocities is likely to be negligible.

3.1.2 Verifying the Hydrodynamic Nature of the Flow

As noted previously, MHD simulations generally require simulated magnetic fields to have high levels of ordering; this restriction is antithetical to the aims of this thesis. In this work we assume a magnetic field that is both uniform in strength and disordered in structure as it enters the jet. In order to check that the magnetic field structure in simulations with low magnetic flux density has no significant effect on the results, we examined four simulations with identical hydrodynamical

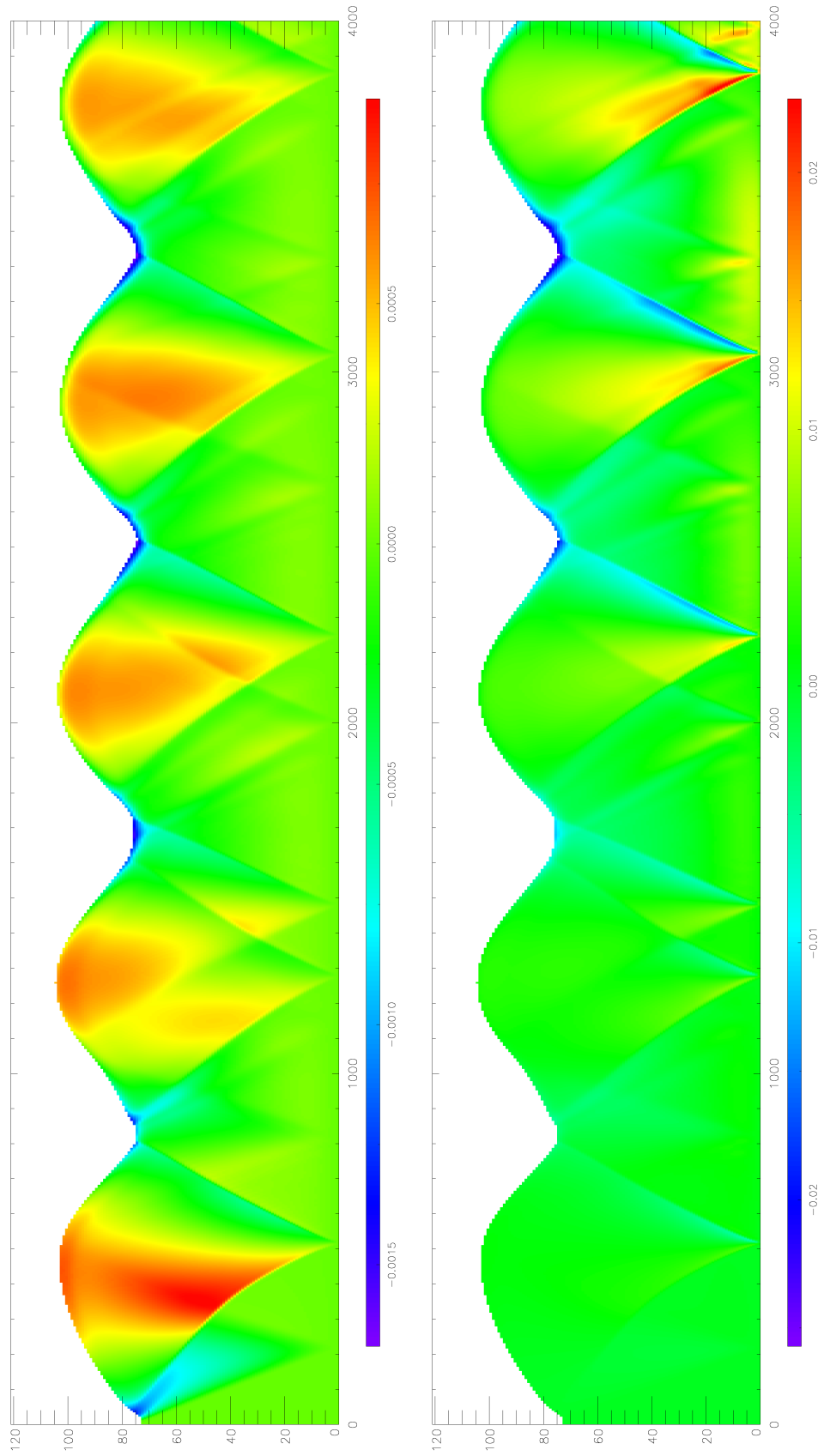


Figure 3.2: The azimuthal velocity field of the jet in model J106 (top), and the theoretical number of rotations experienced by particles on streamlines with constant radius, axial and azimuthal velocity, equal to those at the particles' end positions.

CHAPTER 3

initializations with similarly weak magnetic flux densities, but different initial magnetic configurations. These are models J105, J119, J206, and J228, as detailed in Table 3.1.

It was found that the velocity profiles of these jets are almost identical. The largest differences in the axial velocity between the jet models occur where the RSs meet the jet axis; these discrepancies are no greater than 5% between any pair of the four models, and are $\lesssim 0.001\%$ on average. Off-axis, the axial velocity across the RSs also differ from model to model, but these are more modest than those found nearer the axis. Although the fractional differences between the radial velocities are larger, the RS patterns are still very similar, and the average discrepancy between simulations is found to be $\lesssim 3\%$ for $|v_r| \geq 10^{-8}c$. This gives us the confidence to argue that an initially random magnetic field would yield essentially the same shock structure as formed in these simulations, provided it remains similarly weak in strength. The parallelepipeds, that we use to characterize the fluid distortion, from these four simulations are also consequently very similar. The method by which the parallelepipeds are obtained is explained in Section 3.3.

It seems that the reason for the small differences between the velocity profiles, and consequently the parallelepiped profiles, is that the simulations are forming RSs at slightly different distances from the inlet plane. The largest differences then occur when the pre-shock velocities in one model are compared to velocities that are post-shocked in a different model. This is clearly visible in Figure 3.3, which shows the velocity components of models J105 and J119, and their differences. The overall similarity between these jets with differently ordered magnetic fields indicates that at low magnetizations, the FGMP code produces jets that approach the magnetization-free limit.

CHAPTER 3

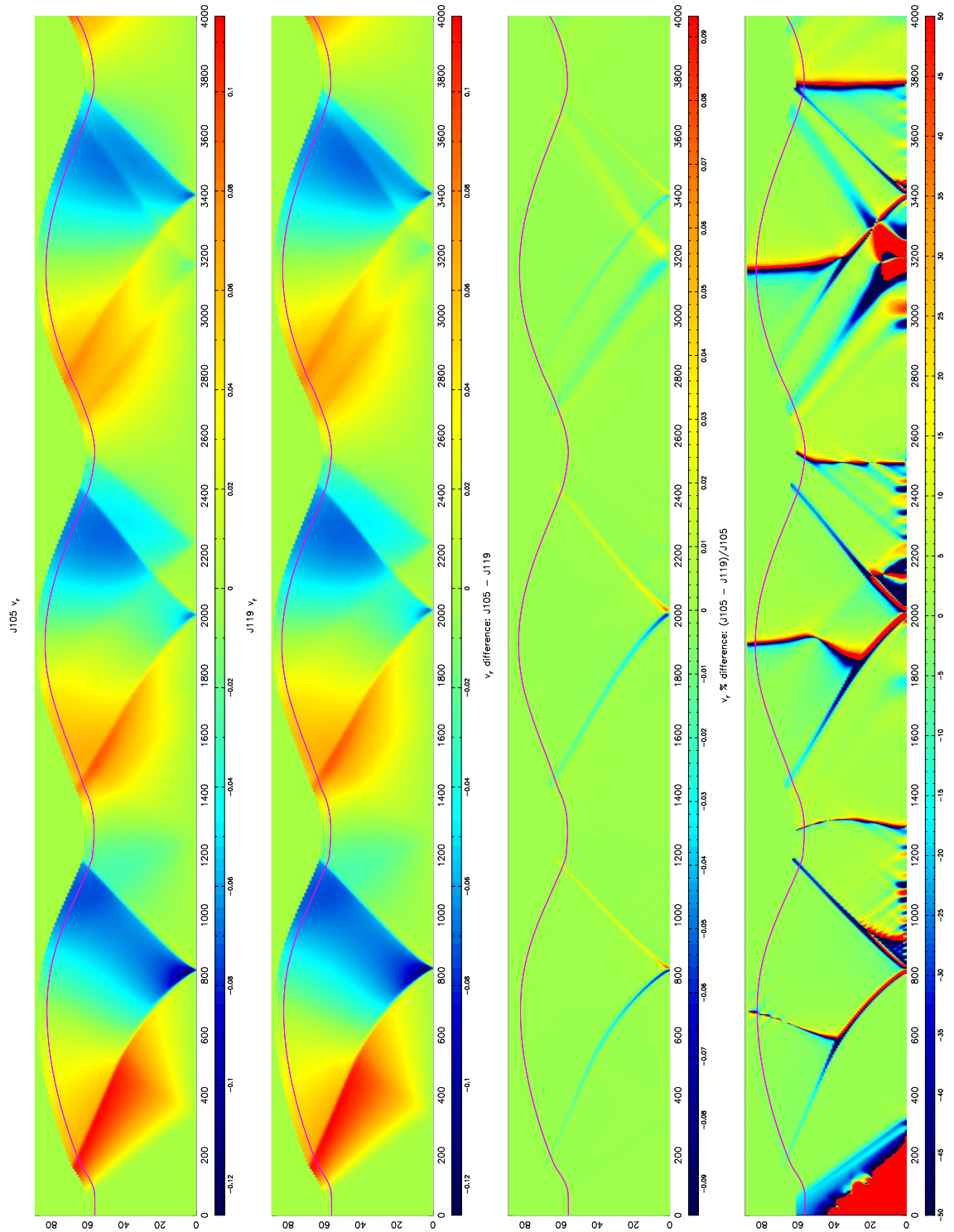


Figure 3.3a: Radial velocity profiles of models J105 and J119 are shown, as well as their differences and percentage differences, in that order, from left to right.

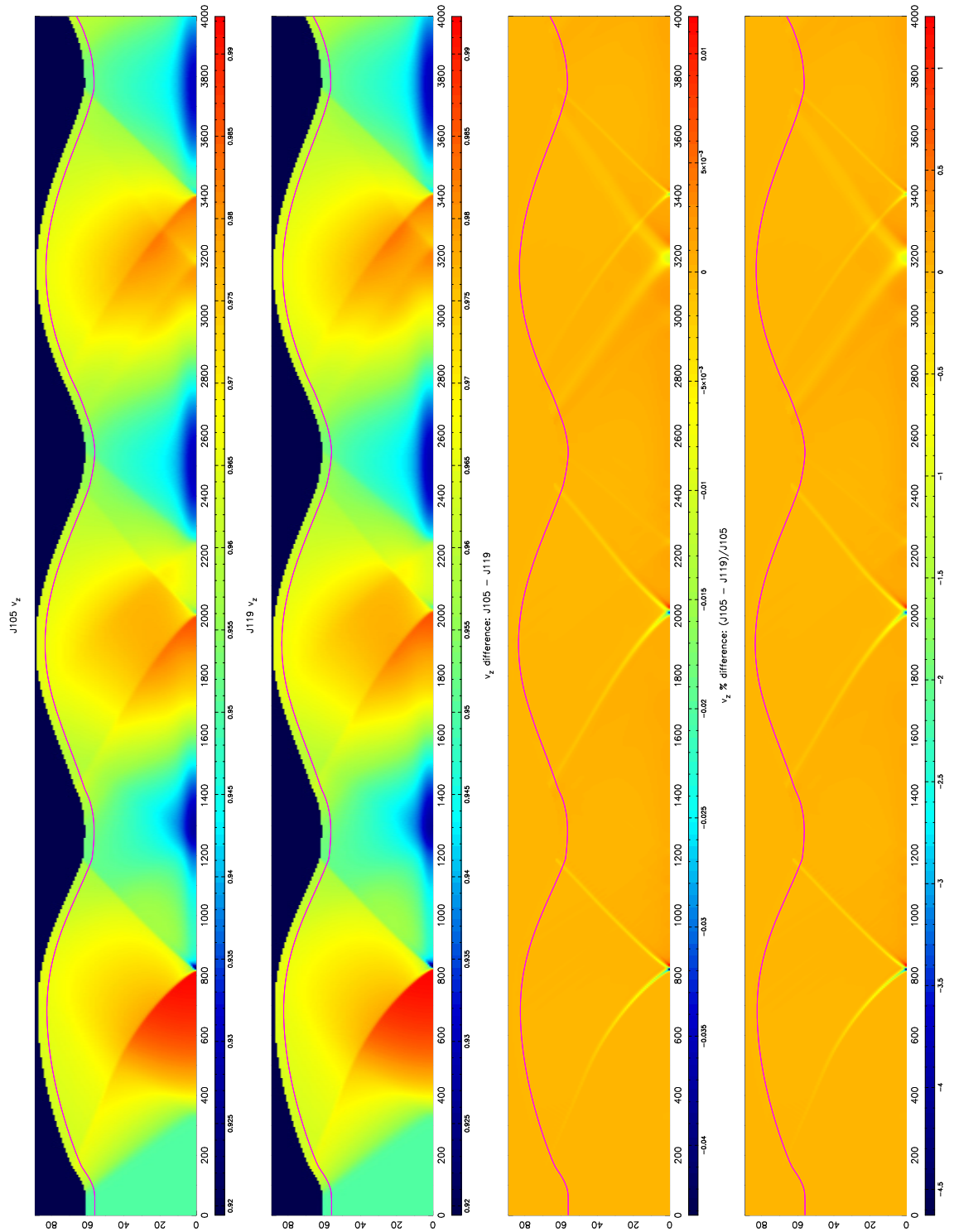


Figure 3.3b: The axial velocity profiles of models J105 and J119 are shown, as well as their differences and percentage differences, in that order, from left to right.

3.2 Determining Synchrotron Emission Coefficients

In order to compare a simulation with observations, it is necessary to determine what radiation would be produced by such a system, and what fraction of this would reach the observer. Radiative transfer calculations evaluate the process of energy transfer via radiation, using the emissivity, and opacity, of each simulation element that contributes to the total radiation field.

The images produced throughout this thesis are monochromatic, and opacity is assumed to be negligible, i.e. images are only simulated for a wavelength at which the source would be optically thin. In this section we obtain the emission coefficients that are used in the radiative transfer of Section 3.5.

3.2.1 Stokes Parameters

For a near-monochromatic, electromagnetic plane wave propagating in the z -direction, the electric field vector $\mathbf{E}(t) = E_x(t)\hat{\mathbf{i}} + E_y(t)\hat{\mathbf{j}}$, where (e.g. Kosowsky, 1999):

$$E_x(t) = A_x(t) \cos(\bar{\omega}t - \theta_x(t)), \quad (3.1a)$$

$$E_y(t) = A_y(t) \cos(\bar{\omega}t - \theta_y(t)); \quad (3.1b)$$

the wave's mean angular frequency is $\bar{\omega}$, and the component amplitudes A_x and A_y , and phase angles θ_x and θ_y , are functions of time t . The Stokes parameters— I , Q , U , and V —are a concise notation used to uniquely describe the polarization state of radiation. The total intensity is given by Stokes I , linear polarization is measured by Q and U , and V defines the circular polarization. For the plane wave described by Equation (3.1), the Stokes parameters are defined as the following time averages:

$$\begin{aligned} I &\equiv \langle A_x^2 \rangle + \langle A_y^2 \rangle, & Q &\equiv \langle A_x^2 \rangle - \langle A_y^2 \rangle, \\ U &\equiv \langle 2A_x A_y \cos(\theta_x - \theta_y) \rangle, & V &\equiv \langle 2A_x A_y \sin(\theta_x - \theta_y) \rangle. \end{aligned}$$

CHAPTER 3

Due to the generally low levels of circular polarization present in synchrotron radiation (i.e. $V \ll 1\%$, Pacholczyk, 1970), we assume that $V = 0$ throughout this thesis; we include Stokes V here for completeness, but it will not be mentioned beyond this section. The polarized flux density $P = \sqrt{Q^2 + U^2(+V^2)}$, the degree of polarization $\Pi = P/I$, and the electric vector polarization angle (EVPA) $\chi = \frac{1}{2} \tan^{-1}(U/Q)$.

3.2.2 Determining the Synchrotron Emission

In this thesis, we are only concerned with optically thin, monochromatic, radio synchrotron emission. It is also assumed that the initial magnetic fields of the jet plasma are completely, or predominantly, disordered; a volume of plasma with a randomly tangled magnetic field would produce synchrotron emission with $\Pi \approx 0$, from any viewing angle, while the polarization from an ordered field depends strongly on the specific configuration of the magnetic field, and its orientation with respect to the observer.

To determine the synchrotron emission produced, we follow the methods of Matthews & Scheuer (1990), who assumed that the initial magnetic field is completely disordered; we show how this approach may be extended to magnetic fields with ordered components in Section 3.2.3. Consider a rest-frame (indicated by the primes), unit cube of plasma, initially with the uniform, flux-frozen magnetic field

$$\mathbf{B}'_0 = B_{0x}\mathbf{a}'_0 + B_{0y}\mathbf{b}'_0 + B_{0z}\mathbf{c}'_0. \quad (3.2)$$

After this cube, with sides $\mathbf{a}'_0 = \hat{\mathbf{i}}$, $\mathbf{b}'_0 = \hat{\mathbf{j}}$, and $\mathbf{c}'_0 = \hat{\mathbf{k}}$, becomes distorted into a parallelepiped with sides \mathbf{a}' , \mathbf{b}' , and \mathbf{c}' , the magnetic field is given by

$$\mathbf{B}' = B_a\mathbf{a}' + B_b\mathbf{b}' + B_c\mathbf{c}'. \quad (3.3)$$

Magnetic flux-freezing, and the conservation of flux threading each parallelepiped

CHAPTER 3

surface, requires that the following holds true for each parallelepiped surface:

$$\begin{aligned}\Phi_x &= \mathbf{B}'_0 \cdot \hat{\mathbf{i}} = \mathbf{B}' \cdot (\mathbf{b}' \times \mathbf{c}'), \\ \Phi_y &= \mathbf{B}'_0 \cdot \hat{\mathbf{j}} = \mathbf{B}' \cdot (\mathbf{c}' \times \mathbf{a}'), \\ \Phi_z &= \mathbf{B}'_0 \cdot \hat{\mathbf{k}} = \mathbf{B}' \cdot (\mathbf{a}' \times \mathbf{b}').\end{aligned}$$

Using Equations (3.2) and (3.3) in conjunction with these results, we can obtain

$$\begin{aligned}B_{0x} &= B_a(\mathbf{a}' \cdot \mathbf{b}' \times \mathbf{c}'), \\ B_{0y} &= B_b(\mathbf{a}' \cdot \mathbf{b}' \times \mathbf{c}'), \\ B_{0z} &= B_c(\mathbf{a}' \cdot \mathbf{b}' \times \mathbf{c}'),\end{aligned}$$

which allows Equation (3.3) to be rewritten as

$$\mathbf{B}' = \frac{(B_{0x}\mathbf{a}' + B_{0y}\mathbf{b}' + B_{0z}\mathbf{c}')}{\mathbf{a}' \cdot \mathbf{b}' \times \mathbf{c}'}. \quad (3.4)$$

We assume that, throughout the simulation, the spectral index $\alpha = 1^*$ because this makes the upcoming calculations in this section significantly easier; we are justified in making such an assumption because (i) the chosen spectral index is close to the observed range of values ~ 0.5 – 0.7 , and (ii) the fractional polarization has been shown to be largely unaffected by different spectral indices (Hughes et al., 1985). We also assume that the relativistic electron population has an energy distribution such that

$$dn = K\Gamma^{-2\alpha-1} d\Gamma \quad (3.5)$$

represents the number of particles, per unit volume, with Lorentz factor in the range Γ to $\Gamma + d\Gamma$. The K term is a constant per unit volume, and we define the value $K = K_0$ where the particles are first injected. The initial dn_0 particles, with Lorentz

*We use the convention that the flux density $S(\nu)$ of a source is related to the frequency of emission ν by the relation $S(\nu) \propto \nu^{-\alpha}$, where α is the spectral index of the source.

CHAPTER 3

factors Γ_0 to $\Gamma_0 + d\Gamma_0$, become $V' dn = dn_0$ particles with Lorentz factors between $\Gamma = \Gamma_0 V'^{-1/3}$ and $\Gamma + d\Gamma = (\Gamma_0 + d\Gamma_0) V'^{-1/3}$. Substituting this into Equation (3.5), e.g. Matthews & Scheuer (1990), we obtain

$$K = K_0 V'^{-\frac{2}{3}\alpha-1}. \quad (3.6)$$

The emission coefficients of the Stokes parameters for synchrotron radiation, per unit volume, are given by (e.g. Rybicki & Lightman, 1979)

$$\begin{aligned} j'_I &= CK \left(\tilde{B}'_l{}^2 + \tilde{B}'_m{}^2 \right)^{(1+\alpha)/2} \\ j'_Q &= \Delta_0 CK \left(\tilde{B}'_l{}^2 + \tilde{B}'_m{}^2 \right)^{(\alpha-1)/2} \left(\tilde{B}'_l{}^2 - \tilde{B}'_m{}^2 \right) \\ j'_U &= \Delta_0 CK \left(\tilde{B}'_l{}^2 + \tilde{B}'_m{}^2 \right)^{(\alpha-1)/2} 2\tilde{B}'_l \tilde{B}'_m \end{aligned}$$

where C is a constant, and $\Delta_0 = (3\alpha + 3)/(3\alpha + 5)$. We define $\tilde{B}'_l = \mathbf{B}' \cdot \hat{\mathbf{l}}/V'$ and $\tilde{B}'_m = \mathbf{B}' \cdot \hat{\mathbf{m}}/V'$, where the rest-frame parallelepiped volume $V' = |\mathbf{a}' \cdot (\mathbf{b}' \times \mathbf{c}')|$, and unit vectors $\hat{\mathbf{l}}$, $\hat{\mathbf{m}}$, and line-of-sight vector $\hat{\mathbf{n}}$ form an orthogonal set. Recalling that we assume $\alpha = 1$, and since $\tilde{B}'_l = (B_{0x}a'_l + B_{0y}b'_l + B_{0z}c'_l)/V'$ and $\tilde{B}'_m = (B_{0x}a'_m + B_{0y}b'_m + B_{0z}c'_m)/V'$ from Equation (3.4), averaging over all possible injection angles for the uniform, initial magnetic field gives

$$\begin{aligned} \langle j'_I \rangle &= \frac{CK}{V'^2} \left(\langle B_{0x}^2 \rangle (a_l'^2 + a_m'^2) + \langle B_{0y}^2 \rangle (b_l'^2 + b_m'^2) \right. \\ &\quad + \langle B_{0z}^2 \rangle (c_l'^2 + c_m'^2) + 2 \langle B_{0x}B_{0y} \rangle (a'_l b'_l + a'_m b'_m) \\ &\quad \left. + 2 \langle B_{0x}B_{0z} \rangle (a'_l c'_l + a'_m c'_m) + 2 \langle B_{0y}B_{0z} \rangle (b'_l c'_l + b'_m c'_m) \right), \quad (3.7a) \end{aligned}$$

$$\begin{aligned}
 \langle j'_Q \rangle = \frac{3CK}{4V'^2} & \left(\langle B_{0x}^2 \rangle (a_l'^2 - a_m'^2) + \langle B_{0y}^2 \rangle (b_l'^2 - b_m'^2) \right. \\
 & + \langle B_{0z}^2 \rangle (c_l'^2 - c_m'^2) + 2 \langle B_{0x} B_{0y} \rangle (a_l' b_l' - a_m' b_m') \\
 & \left. + 2 \langle B_{0x} B_{0z} \rangle (a_l' c_l' - a_m' c_m') + 2 \langle B_{0y} B_{0z} \rangle (b_l' c_l' - b_m' c_m') \right), \quad (3.7b)
 \end{aligned}$$

$$\begin{aligned}
 \langle j'_U \rangle = \frac{3CK}{2V'^2} & \left(\langle B_{0x}^2 \rangle a_l' a_m' + \langle B_{0y}^2 \rangle b_l' b_m' + \langle B_{0z}^2 \rangle c_l' c_m' \right. \\
 & + \langle B_{0x} B_{0y} \rangle (a_l' b_m' + b_l' a_m') + \langle B_{0x} B_{0z} \rangle (a_l' c_m' + c_l' a_m') \\
 & \left. + \langle B_{0y} B_{0z} \rangle (b_l' c_m' + c_l' b_m') \right), \quad (3.7c)
 \end{aligned}$$

where the angled brackets denote a value averaged over all possible field orientations of the initial magnetic field \mathbf{B}_0 ; i.e. in spherical polar coordinates

$$\langle \mathcal{S} \rangle = \frac{\int_0^{2\pi} \int_0^\pi \mathcal{S}(\theta, \phi) \sin \theta \, d\theta \, d\phi}{\int_0^{2\pi} \int_0^\pi \sin \theta \, d\theta \, d\phi},$$

where θ and ϕ are the polar and azimuthal angles respectively.

3.2.3 Defining the Magnetic Field

We assume that all realizations of a uniform magnetic field are found on the sub-grid level within each pixel; therefore, by averaging over all possible directions of an injected uniform magnetic field, we are able to obtain results that are statistically equivalent to an injected plasma with a disordered magnetic field. We choose to initialize all parallelepipeds such that they are unit cubes threaded by fields B_{0x} , B_{0y} , and B_{0z} , which are parallel to the x -, y -, and z -axes respectively. In this section we show the results of averaging over the directions of a disordered magnetic field component that is uniform in magnitude.

CHAPTER 3

Purely Disordered Field

A magnetic field that is completely randomly tangled is given by

$$\mathbf{B}'_0 = B_r \left(\sin \theta (\cos \phi \hat{\mathbf{i}} + \sin \phi \hat{\mathbf{j}}) + \cos \theta \hat{\mathbf{k}} \right),$$

where B_r is the strength of the randomly tangled magnetic field; when the squared terms are averaged over all possible injection angles (θ, ϕ) , we find that

$$\begin{aligned} \langle B_{0x}^2 \rangle &= \langle B_{0y}^2 \rangle = \langle B_{0z}^2 \rangle = \frac{B_r^2}{3}, \\ \langle B_{0x} B_{0y} \rangle &= \langle B_{0x} B_{0z} \rangle = \langle B_{0y} B_{0z} \rangle = 0. \end{aligned}$$

Therefore, from Equation (3.7), the corresponding Stokes parameter emissivities in the particle rest frame are

$$\langle j'_I \rangle = \frac{CKB_r^2}{3V'^2} (a_l'^2 + b_l'^2 + c_l'^2 + a_m'^2 + b_m'^2 + c_m'^2), \quad (3.8a)$$

$$\langle j'_Q \rangle = \frac{CKB_r^2}{4V'^2} (a_l'^2 + b_l'^2 + c_l'^2 - a_m'^2 - b_m'^2 - c_m'^2), \quad (3.8b)$$

$$\langle j'_U \rangle = \frac{CKB_r^2}{2V'^2} (a_l' a_m' + b_l' b_m' + c_l' c_m'). \quad (3.8c)$$

as found earlier by Matthews & Scheuer (1990).

Disordered Field with an Axial Component

For a randomly tangled magnetic field that also has a component parallel to the jet-axis of magnitude B_{\parallel} , the field is given by

$$\mathbf{B}'_0 = B_r \sin \theta (\cos \phi \hat{\mathbf{i}} + \sin \phi \hat{\mathbf{j}}) + (B_r \cos \theta + B_{\parallel}) \hat{\mathbf{k}}.$$

CHAPTER 3

Upon spatially averaging the squared components, we obtain

$$\begin{aligned}\langle B_{0x}^2 \rangle &= \langle B_{0y}^2 \rangle = \frac{B_r^2}{3}, \\ \langle B_{0z}^2 \rangle &= \frac{B_r^2}{3} + B_{\parallel}^2, \\ \langle B_{0x}B_{0y} \rangle &= \langle B_{0x}B_{0z} \rangle = \langle B_{0y}B_{0z} \rangle = 0,\end{aligned}$$

and so the Stokes parameters according to Equation (3.7) are

$$\langle j'_I \rangle = \frac{CK}{V'^2} \left(\frac{B_r^2}{3} (a_l'^2 + b_l'^2 + c_l'^2 + a_m'^2 + b_m'^2 + c_m'^2) + B_{\parallel}^2 (c_l'^2 + c_m'^2) \right), \quad (3.9a)$$

$$\langle j'_Q \rangle = \frac{3CK}{4V'^2} \left(\frac{B_r^2}{3} (a_l'^2 + b_l'^2 + c_l'^2 - a_m'^2 - b_m'^2 - c_m'^2) + B_{\parallel}^2 (c_l'^2 - c_m'^2) \right), \quad (3.9b)$$

$$\langle j'_U \rangle = \frac{3CK}{2V'^2} \left(\frac{B_r^2}{3} (a_l'a_m' + b_l'b_m' + c_l'c_m') + B_{\parallel}^2 c_l'c_m' \right). \quad (3.9c)$$

Disordered Field with a Helical Component

It has been argued that jets may contain a helical component of magnetic field, possibly a relic of the extraction of plasma from a spinning accretion disc (e.g. Murphy et al., 2013). For a magnetic field that is randomly tangled, but also has a component B_h that is helically ordered with a pitch angle φ to the jet-parallel axis, the corresponding magnetic field is

$$\begin{aligned}\mathbf{B}'_0 &= (B_r \sin \theta \cos \phi - B_h \sin \varphi \sin \psi) \hat{\mathbf{i}} \\ &\quad + (B_r \sin \theta \sin \phi + B_h \sin \varphi \cos \psi) \hat{\mathbf{j}} \\ &\quad + (B_r \cos \theta + B_h \cos \varphi) \hat{\mathbf{k}},\end{aligned}$$

CHAPTER 3

where the position angle $\psi = \arctan2(y, x)$. Spatially averaging the squared magnetic field components for this field, we find

$$\begin{aligned}\langle B_{0x}^2 \rangle &= \frac{B_r^2}{3} + B_h^2 \sin^2 \varphi \sin^2 \psi, & \langle B_{0x} B_{0y} \rangle &= -\frac{B_h^2}{2} \sin^2 \varphi \sin(2\psi), \\ \langle B_{0y}^2 \rangle &= \frac{B_r^2}{3} + B_h^2 \sin^2 \varphi \cos^2 \psi, & \langle B_{0x} B_{0z} \rangle &= -\frac{B_h^2}{2} \sin(2\varphi) \sin \psi, \\ \langle B_{0z}^2 \rangle &= \frac{B_r^2}{3} + B_h^2 \cos^2 \varphi, & \langle B_{0y} B_{0z} \rangle &= \frac{B_h^2}{2} \sin(2\varphi) \cos \psi.\end{aligned}$$

By substituting these terms into Equation (3.7), we obtain

$$\begin{aligned}\langle j'_I \rangle &= \frac{CK}{V'^2} \left(\frac{B_r^2}{3} (a_l'^2 + b_l'^2 + c_l'^2 + a_m'^2 + b_m'^2 + c_m'^2) \right. \\ &\quad + B_h^2 \left[\sin^2 \varphi \left(\sin^2 \psi (a_l'^2 + a_m'^2) + \cos^2 \psi (b_l'^2 + b_m'^2) \right) \right. \\ &\quad + \cos^2 \varphi (c_l'^2 + c_m'^2) - \left. \left\{ (a_l' b_l' + a_m' b_m') \sin^2 \varphi \sin(2\psi) \right. \right. \\ &\quad \left. \left. + \sin(2\varphi) \left((a_l' c_l' + a_m' c_m') \sin \psi - (b_l' c_l' + b_m' c_m') \cos \psi \right) \right\} \right] \left. \right), \quad (3.10a)\end{aligned}$$

$$\begin{aligned}\langle j'_Q \rangle &= \frac{3CK}{4V'^2} \left(\frac{B_r^2}{3} (a_l'^2 + b_l'^2 + c_l'^2 - a_m'^2 - b_m'^2 - c_m'^2) \right. \\ &\quad + B_h^2 \left[\sin^2 \varphi \left(\sin^2 \psi (a_l'^2 - a_m'^2) + \cos^2 \psi (b_l'^2 - b_m'^2) \right) \right. \\ &\quad + \cos^2 \varphi (c_l'^2 - c_m'^2) - \left\{ \sin^2 \varphi \sin(2\psi) (a_l' b_l' - a_m' b_m') \right. \\ &\quad \left. \left. + \sin(2\varphi) \left((a_l' c_l' - a_m' c_m') \sin \psi - (b_l' c_l' - b_m' c_m') \cos \psi \right) \right\} \right] \left. \right), \quad (3.10b)\end{aligned}$$

$$\begin{aligned}\langle j'_U \rangle &= \frac{3CK}{2V'^2} \left(\frac{B_r^2}{3} (a_l' a_m' + b_l' b_m' + c_l' c_m') \right. \\ &\quad + B_h^2 \left[\sin^2 \varphi (\sin^2 \psi a_l' a_m' + \cos^2 \psi b_l' b_m') \right. \\ &\quad + \cos^2 \varphi c_l' c_m' - \frac{1}{2} \left\{ \sin^2 \varphi \sin(2\psi) (a_l' b_m' + b_l' a_m') \right. \\ &\quad \left. \left. + \sin(2\varphi) \left((a_l' c_m' + c_l' a_m') \sin \psi - (b_l' c_m' + c_l' b_m') \cos \psi \right) \right\} \right] \left. \right). \quad (3.10c)\end{aligned}$$

3.3 Streamline-based Parallelepiped Monitoring

In Section 2.7.1, the evolution of the parallelepiped vectors obtained using flux-based methods was compared to that using a more intuitive method based on streamlines in the flow. In this section, the streamline method is explained in detail. The method is similar to that used by Matthews & Scheuer (1990), who injected marker particles into the base of the flow at regular intervals, and followed their pathlines through the simulation. By monitoring the positions of the particles at the vertices of an initially cubic volume, the evolution of the cube into a parallelepiped may be followed, and the parallelepiped vectors found from the changes in vertex separation. An unfortunate result of this method is that the distribution of marker particles depends on the evolution of the flow, and becomes very irregular far from the injection plane. This leads to the difficult problem of interpolating the parallelepiped vectors from an irregularly sampled grid.

The streamline method used here is applicable to steady flows, so that marker particles follow the streamlines. To avoid the problem of an irregular distribution of parallelepipeds, a set of parallelepiped vectors is obtained for every grid point. This is done by advecting a particles at the centre of each grid point \mathbf{s}_0 backwards for N iterations, to a point \mathbf{s}_{base} , no more than one pixel from the inlet plane. We then advect a marker particle forwards from \mathbf{s}_{base} for N time steps, in order to verify the accuracy of the calculated streamline. If the final position of the marker particle is equal to \mathbf{s}_0 with a tolerance of 1% of the grid resolution then the streamline is accepted, and it was found that the average streamline discrepancy for models J105, J106 and J109 is much better than this, with discrepancies $\sim 10^{-4}\%$ of the grid resolution in the radial and axial directions. For verified streamlines, three further marker particles at the vertices of the cubical volume enclosing \mathbf{s}_{base} are released in

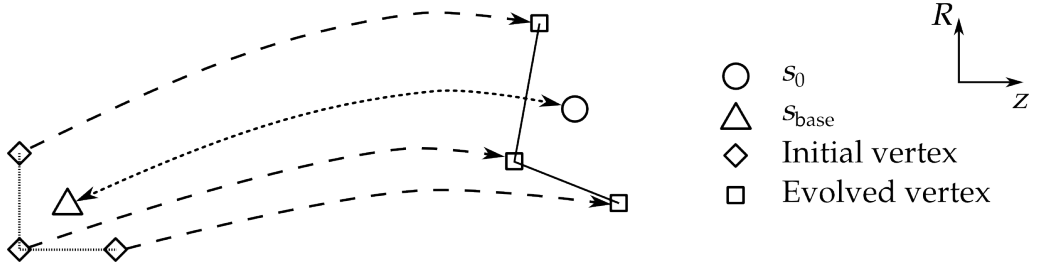


Figure 3.4: Schematic showing the marker particles advected, and how the change in particle separation gives the evolved parallelepiped vectors

the R - z plane at

$$\mathbf{s}_{\text{base}} - \frac{\delta_{xyz}}{4} (\hat{\mathbf{r}} + \hat{\mathbf{k}}), \quad \text{and} \quad \mathbf{s}_{\text{base}} + \frac{\delta_{xyz}}{4} (\pm \hat{\mathbf{r}} \mp \hat{\mathbf{k}}), \quad (3.11)$$

where δ_{xyz} is the grid coordinate separation. An illustration of the marker-particles advected for any particular grid point is shown in Figure 3.4.

To determine the evolved state of each parallelepiped vector using this method, two separate marker-particles per vector, of initial displacement $\Delta \mathbf{s}_{\text{base}}$, are released from the base of the jet; for simplicity, we always initialize the parallelepipeds with

$$\mathbf{a}'_0 = \hat{\mathbf{i}}, \quad \mathbf{b}'_0 = \hat{\mathbf{j}}, \quad \text{and} \quad \mathbf{c}'_0 = \hat{\mathbf{k}}. \quad (3.12)$$

The final displacement between the marker-particle pair $\Delta \mathbf{s}$ corresponds to the relevant distorted parallelepiped vector, which we calculate in the laboratory frame of the simulation. To initialize the parallelepiped such that Equation (3.12) is satisfied, after the deformed parallelepiped vectors have been obtained, it is necessary to reduce all components of \mathbf{c} by the Lorentz factor at the streamline's base Γ_{base} so that the initial rest frame value of $\mathbf{c}'_0 = (0, 0, 1)$. As noted in Equation (3.11), the vector marker particles have a total initial displacement of half of the grid spacing, meaning that all relevant terms must be scaled up by a factor of 2 in order to obtain the correct Stokes parameters from the emission. The reason for using an offset of

CHAPTER 3

$\pm\delta_{xyz}/4$ and then scaling the vectors, as opposed to $\pm\delta_{xyz}/2$, is that this provides us with a more sensitive measure of the local velocity gradients.

To advect a particle from its position in one iteration \mathbf{s}_i , where its velocity $\mathbf{v}_i = \mathbf{v}(\mathbf{s}_i)$, to its next iterative position \mathbf{s}_{i+1} , it is necessary to use the first-order Taylor series expansion of the velocities, such that a test particle will follow the same streamline between two points, i.e. $\overrightarrow{AB} \cong -\overleftarrow{AB}$.

An initial estimate of \mathbf{s}_{i+1} is provided by

$$\mathbf{s}_{i+1} = \mathbf{s}_i + \mathbf{v}_i\delta t,$$

where the velocity is $\mathbf{v}_{i+1} = \mathbf{v}(\mathbf{s}_{i+1})$. The off-grid velocities are determined via bilinear interpolation. The average velocity during this time step is

$$\bar{\mathbf{v}} = \frac{1}{2}(\mathbf{v}_i + \mathbf{v}_{i+1}),$$

and so our revised estimate of the destination of the particle at the end of the time step is then

$$\mathbf{s}_{i+1} = \mathbf{s}_i + \bar{\mathbf{v}}\delta t.$$

Note that we can write

$$\begin{aligned} \mathbf{s}_{i+1} &= \mathbf{s}_i + \mathbf{v}_i\delta t + \frac{1}{2}\left(\frac{\mathbf{v}_{i+1} - \mathbf{v}_i}{\delta t}\right)\delta t^2, \\ &= \mathbf{s}_i + \mathbf{v}_i\delta t + \frac{1}{2}\mathbf{a}_i\delta t^2, \end{aligned}$$

where \mathbf{a}_i is the average acceleration during the time step. This shows that the increments in δt are equivalent to assuming uniform acceleration over the time step. As noted above, advecting particles from \mathbf{s}_0 to \mathbf{s}_{base} and back typically recovers the value of \mathbf{s}_0 to an accuracy of one part in 10^6 , demonstrating the excellent levels of precision obtained.

3.3.1 Obtaining Extraplanar Parallelepipeds

Since the FGMP models are axisymmetric, and we neglect the very small azimuthal velocities (as justified in Section 3.1.1), the parallelepiped vectors can be found first in the R - z coordinate plane of the simulation, and then simply rotated into the Cartesian $\{x, y, z\}$ coordinate system for any given point in the three-dimensional flow. In cylindrical $\{R, \phi, z\}$ coordinates, the vector initially parallel to the R -axis is $(1, 0, 0)$, and after deformation becomes $(\Delta R_r, 0, \Delta R_k)$. Similarly, the vector initially parallel to the z -axis is $(0, 0, 1)^*$, and is transformed by the flow to become $(\Delta z_r, 0, \Delta z_k)$. The four terms that describe these evolved vectors can be obtained directly from the simulations using the method described in Section 3.3. In axisymmetry, two particles at different ϕ coordinates, but equal in R and z , must move equivalently in their respective R - z planes, and so their separation in ϕ must be proportional to their separation in R . Therefore, the vector initialized parallel to the ϕ axis is transformed from $(0, 1, 0)$ to $(0, \Delta\phi_\varphi, 0)$ in cylindrical coordinates, where

$$\Delta\phi_\varphi = 1 \times \frac{R_0}{R_{\text{base}}}.$$

Terms R_0 and R_{base} are the radial coordinates of the end and base of a streamline, respectively, and these are both determined by the streamline calculation of Section 3.3.

Hence, in cylindrical coordinates, the distortion from the initial parallelepiped (R_0, ϕ_0, z_0) to the evolved parallelepiped (R, ϕ, z) can be described by the equation

$$\begin{pmatrix} R \\ \phi \\ z \end{pmatrix} = \begin{pmatrix} \Delta R_r & 0 & \Delta z_r \\ 0 & \Delta\phi_\varphi & 0 \\ \Delta R_k & 0 & \Delta z_k \end{pmatrix} \begin{pmatrix} R_0 \\ \phi_0 \\ z_0 \end{pmatrix}. \quad (3.13)$$

*We neglect the effects of Lorentz contraction here, and correct for it in Equation (3.15).

CHAPTER 3

The transformations between the Cartesian and cylindrical coordinate systems are given by

$$\begin{pmatrix} R \\ \phi \\ z \end{pmatrix} = \begin{pmatrix} \cos \phi & \sin \phi & 0 \\ -\sin \phi & \cos \phi & 0 \\ 0 & 0 & 1 \end{pmatrix} \begin{pmatrix} x \\ y \\ z \end{pmatrix}, \quad (3.14a)$$

$$\begin{pmatrix} x \\ y \\ z \end{pmatrix} = \begin{pmatrix} \cos \phi & -\sin \phi & 0 \\ \sin \phi & \cos \phi & 0 \\ 0 & 0 & 1 \end{pmatrix} \begin{pmatrix} R \\ \phi \\ z \end{pmatrix}. \quad (3.14b)$$

Then, for example, the value of the parallelepiped vector \mathbf{a} , initially $(1, 0, 0)$ in Cartesian coordinates, or $(\cos \phi, -\sin \phi, 0)$ in cylindrical coordinates (from Equation 3.14a), is deformed by the flow into $(\Delta R_r \cos \phi, -\Delta \phi_\varphi \sin \phi, \Delta R_k \cos \phi)$, according to Equation 3.13. Transforming back into Cartesian coordinates using Equation 3.14b, we obtain the value of \mathbf{a} , evolved by the flow, to be

$$\mathbf{a} = \left(\Delta R_r \cos^2 \phi + \Delta \phi_\varphi \sin^2 \phi, (\Delta R_r - \Delta \phi_\varphi) \sin \phi \cos \phi, \Delta R_k \cos \phi \right).$$

The other parallelepiped vectors can be similarly obtained, leading to

$$\begin{pmatrix} \mathbf{a} \\ \mathbf{b} \\ \mathbf{c} \end{pmatrix} = \begin{pmatrix} \Delta R_r \cos^2 \phi + \Delta \phi_\varphi \sin^2 \phi & (\Delta R_r - \Delta \phi_\varphi) \sin \phi \cos \phi & \Delta R_k \cos \phi \\ (\Delta R_r - \Delta \phi_\varphi) \sin \phi \cos \phi & \Delta R_r \sin^2 \phi + \Delta \phi_\varphi \cos^2 \phi & \Delta R_k \sin \phi \\ \Gamma_{\text{base}}^{-1} \Delta z_r \cos \phi & \Gamma_{\text{base}}^{-1} \Delta z_r \sin \phi & \Gamma_{\text{base}}^{-1} \Delta z_k \end{pmatrix} \begin{pmatrix} 1 \\ 1 \\ 1 \end{pmatrix}, \quad (3.15)$$

in Cartesian coordinates, where vector \mathbf{c} is reduced by the Lorentz factor at the base of the streamline Γ_{base} because of the Lorentz contraction that would affect \mathbf{c}_0 .

In summary, therefore, the streamline analysis of Section 3.3 can be used on the two-dimensional FGMP simulation data to provide a set of parallelepiped vectors in the cylindrical coordinate system for each point in the R - z plane of the simulation.

In the Cartesian x - z plane, these translate directly into the \mathbf{a} , \mathbf{b} , and \mathbf{c} vectors. In other planes (i.e. for $\phi \neq 0$), these can be used to obtain the \mathbf{a} , \mathbf{b} , and \mathbf{c} vectors using Equation 3.15.

3.4 Rest-Frame Parallelepiped Vector Transforms

In this section, we describe the multiple reference frames used in the process of determining the advection of a marker particle and calculating the Stokes parameters of its associated parallelepiped volume; the axes described are illustrated in Figure 3.5. Equation (3.7) gives the Stokes parameters produced by a synchrotron radiating particle in its rest-frame, while the parallelepipeds, most easily determined in the frame of the observer, must therefore be transformed between reference frames. The simplest way to obtain the rest-frame values of a vector is to rotate from the fixed Cartesian frame, described by the $\{\hat{\mathbf{i}}, \hat{\mathbf{j}}, \hat{\mathbf{k}}\}$ triad, to a local frame described by the triad $\{\hat{\mathbf{e}}_1, \hat{\mathbf{e}}_2, \hat{\mathbf{e}}_3\}$, in which

$$\begin{aligned}\hat{\mathbf{e}}_1 &= \hat{\boldsymbol{\beta}}, \\ \hat{\mathbf{e}}_2 &= \hat{\mathbf{e}}_3 \times \hat{\mathbf{e}}_1, \\ \hat{\mathbf{e}}_3 &= \hat{\mathbf{e}}_1 \times \hat{\mathbf{n}} / |\hat{\mathbf{e}}_1 \times \hat{\mathbf{n}}|;\end{aligned}$$

the line-of-sight unit vector $\hat{\mathbf{n}} = \hat{\mathbf{i}} \sin \theta + \hat{\mathbf{k}} \cos \theta$, where θ is the angle between the line-of-sight and the jet-axis, and $\hat{\boldsymbol{\beta}} = \boldsymbol{\beta} / |\boldsymbol{\beta}|$ is the unit velocity vector. This makes it trivial to determine the rest-frame values of the parallelepiped vectors; the component parallel to the velocity vector suffers Lorentz contraction, while the perpendicular components are unaffected:

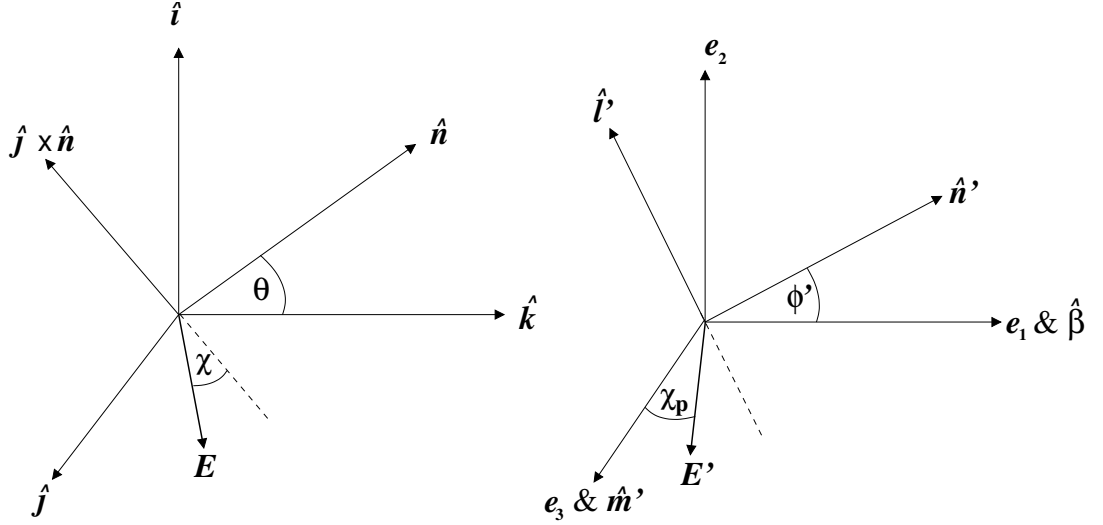


Figure 3.5: Left panel: This figure shows the principal axes of the simulation. The jet axis is parallel to unit vector $\hat{\mathbf{k}}$, and the line-of-sight unit vector $\hat{\mathbf{n}}$ (in the $\hat{\mathbf{i}}-\hat{\mathbf{k}}$ plane) points toward the observer. The vector $\hat{\mathbf{j}} \times \hat{\mathbf{n}}$ lies in the sky-plane, perpendicular to $\hat{\mathbf{j}}$. The vector \mathbf{E} indicates a direction in the sky plane parallel to the plane of polarization, and the polarization angle χ is measured from $-\hat{\mathbf{j}} \times \hat{\mathbf{n}}$ to \mathbf{E} .

Right panel: This figure shows the coordinate system in which the polarization angle is most easily determined. For each simulation cell, the unit vector \mathbf{e}_1 is parallel to the fluid velocity, and the unit vector toward the observer $\hat{\mathbf{n}}'$ lies in the $\mathbf{e}_1-\mathbf{e}_2$ plane. The angle between \mathbf{e}_1 and $\hat{\mathbf{n}}'$ is ϕ' in the rest frame of the fluid. The unit vectors $\hat{\mathbf{l}}'$ and $\hat{\mathbf{m}}'$ lie in the sky plane: $\hat{\mathbf{m}}'$ is parallel to \mathbf{e}_3 and $\hat{\mathbf{l}}'$ is parallel to $\hat{\mathbf{m}}' \times \hat{\mathbf{n}}'$. The vector \mathbf{E}' indicates a direction in the sky plane parallel to the plane of electric polarization, and the polarization angle χ_p is measured from $\hat{\mathbf{m}}'$ to \mathbf{E}' . Since $\hat{\mathbf{m}}'$ varies from cell to cell, it is necessary to refer the polarization angle to the fixed vector $\hat{\mathbf{j}}$, giving a fixed reference direction which is the same for all cells.

$$\begin{aligned}\mathcal{A}' \cdot \hat{\mathbf{e}}_1 &= \mathcal{A} \cdot \hat{\mathbf{e}}_1 / \Gamma, \\ \mathcal{A}' \cdot \hat{\mathbf{e}}_2 &= \mathcal{A} \cdot \hat{\mathbf{e}}_2, \\ \mathcal{A}' \cdot \hat{\mathbf{e}}_3 &= \mathcal{A} \cdot \hat{\mathbf{e}}_3.\end{aligned}$$

The angle between the line-of-sight and velocity vectors in the observer's frame of reference is given by

$$\cos \phi = \frac{\boldsymbol{\beta} \cdot \hat{\mathbf{n}}}{|\boldsymbol{\beta}| |\hat{\mathbf{n}}|} = \hat{\boldsymbol{\beta}} \cdot \hat{\mathbf{n}}, \quad (3.16)$$

where we assume $0 \leq \phi \leq \pi$ for uniqueness. Due to aberration, in the rest frame this angle will be

$$\cos \phi' = \frac{\cos \phi - |\boldsymbol{\beta}|}{1 - |\boldsymbol{\beta}| \cos \phi}. \quad (3.17)$$

To calculate the Stokes parameters, Equation (3.7) requires the components of magnetic field to be projected onto the observer's on-sky plane in the fluid's rest frame, $(\hat{\mathbf{l}}', \hat{\mathbf{m}}', \hat{\mathbf{n}}')$, where

$$\begin{aligned}\hat{\mathbf{l}}' &= \hat{\mathbf{m}}' \times \hat{\mathbf{n}}', \\ \hat{\mathbf{m}}' &= \hat{\mathbf{e}}_3, \\ \hat{\mathbf{n}}' &= \cos \phi' \hat{\mathbf{e}}_1 + \sin \phi' \hat{\mathbf{e}}_2.\end{aligned}$$

3.5 Radiative Transfer and Transforming Emission Coefficients

The emission coefficients j'_I , j'_Q and j'_U given by Equations (3.7) are defined relative to the $(\hat{\mathbf{l}}', \hat{\mathbf{m}}', \hat{\mathbf{n}}')$ coordinate system (see Figure 3.5, right panel), which is in the rest frame of the fluid, and oriented so that $\hat{\mathbf{n}}'$ is toward the observer, and $\hat{\mathbf{l}}'$ lies in the plane of $\hat{\mathbf{n}}'$ and $\hat{\mathbf{e}}_1$ ($\hat{\mathbf{e}}_1$ is parallel to the fluid velocity). Evaluation of the rest-frame parallelepiped vectors \mathbf{a}' , \mathbf{b}' and \mathbf{c}' relative to the $(\mathbf{e}_1, \mathbf{e}_2, \mathbf{e}_3)$ coordinate

CHAPTER 3

system has been described in Section 3.4, and only a straightforward coordinate rotation is required to obtain their $(\mathbf{l}', \mathbf{m}', \mathbf{n}')$ coordinates. Evaluation of the emission coefficients for each pixel using Equation (3.7) gives j'_I , j'_Q and j'_U , and the two latter values can be combined to give the emission coefficient for polarized flux density, $j'_P = \sqrt{j'_Q{}^2 + j'_U{}^2}$, and $\chi_p = \frac{1}{2} \tan^{-1}(j'_U/j'_Q)$. Angle χ_p gives the magnetic polarization angle of radiation from a single simulation cell, referred to the direction given by \mathbf{m}' .

The emission coefficients for total and polarized intensity transform into the observer frame as (see Rybicki & Lightman, 1979)

$$j_I = j'_I \mathcal{D}^{2+\alpha}, \quad (3.18a)$$

$$j_P = j'_P \mathcal{D}^{2+\alpha}, \quad (3.18b)$$

where $\mathcal{D} = (\Gamma - \Gamma|\beta| \cos \phi)^{-1}$ is the Doppler factor, and the polarization angle χ_p referred to the observer frame \mathbf{l} - and \mathbf{m} -axes is the same as that referred to the rest frame \mathbf{l}' - and \mathbf{m}' -axes (see, e.g. the discussion in Cawthorne & Cobb, 1990). Since the fluid velocity, and hence the \mathbf{l}' - and \mathbf{m}' -axes change from pixel to pixel, it is necessary to determine the emission coefficients for Q and U referred to a fixed direction in the sky plane, which we take to be the direction of $\hat{\mathbf{j}}$ (where $\hat{\mathbf{j}}$ is in the Cartesian y -direction).

Hence, for each pixel we define a magnetic field vector

$$\mathbf{E} = \hat{\mathbf{m}} \cos \chi_p - \hat{\mathbf{l}} \sin \chi_p \quad (3.19)$$

where $\hat{\mathbf{m}} = \hat{\boldsymbol{\beta}} \times \hat{\mathbf{n}} / |\hat{\boldsymbol{\beta}} \times \hat{\mathbf{n}}|$ and $\hat{\mathbf{l}} = \hat{\mathbf{m}} \times \hat{\mathbf{n}}$ are given in terms of the unit vectors of the simulation's Cartesian axes (see Figure 3.5, left panel). Then the required EVPA χ in the jet's rest frame, referred to the direction $\hat{\mathbf{j}}$ is defined by

CHAPTER 3

$$\begin{aligned}\cos \chi &= \mathbf{E} \cdot \hat{\mathbf{j}}, \\ \sin \chi &= \mathbf{E} \cdot (-\hat{\mathbf{j}} \times \hat{\mathbf{n}}).\end{aligned}$$

Finally, the emission coefficients for Q and U (referred to the direction $\hat{\mathbf{j}}$) can be found from

$$\begin{aligned}j_Q &= j_P \cos(2\chi), \\ j_U &= j_P \sin(2\chi),\end{aligned}$$

and these can easily be integrated (or in the optically thin case we use here, simply added) along the line of sight. Hence, Stokes Q is positive where $\mathbf{E} \parallel (\hat{\mathbf{j}} \times \hat{\mathbf{n}})$, and negative where $\mathbf{E} \parallel \hat{\mathbf{j}}$.

For each emitting cell, its on-sky coordinates must be determined. The y -axis lies in the sky-plane, so this coordinate calculation is trivial, and the $\hat{\mathbf{j}} \times \hat{\mathbf{n}}$ coordinate is a projection of the x - and z -axes, given by $\zeta = -x \cos \theta + z \sin \theta$, where θ is the viewing angle. The sky-plane coordinates (ζ, y) of every simulation cell are calculated, and their values of j_I , j_Q , and j_U are linearly decomposed onto the nearest on-sky pixels. Each pixel on the sky-plane stores the sum total of each of the Stokes emissivities, and when the contribution from every cell has been include, we obtain

$$\begin{aligned}I(\zeta, y) &= \int j_I(\zeta, y) \, d\ell, \\ Q(\zeta, y) &= \int j_Q(\zeta, y) \, d\ell, \\ U(\zeta, y) &= \int j_U(\zeta, y) \, d\ell,\end{aligned}$$

where ℓ is our line of sight. As defined in Section 3.2.1, the sky-plane pixel values of P and χ are then given by $P = \sqrt{Q^2 + U^2}$ and $\chi = \frac{1}{2} \tan^{-1}(U/Q)$.

Chapter 4

Results

In this chapter we present the simulated images that were produced from the hot, intermediate, and cold jets from the FGMP code (i.e. models J105, J106, and J109 respectively in Table 3.1), using the methods detailed in the previous chapter. We primarily concentrate on the first recollimation shock within each jet, as the complexity of the recollimation shock (RS) geometry increases thereafter for these models due to reflections occurring at the boundary $r = 0$. After calculating the radiative transfer of the simulations, we produce images showing the total intensity, polarized intensity (and thus also fractional polarization), and the electric vector polarization angle (EVPA) across the jets.

4.1 Data Processing

Prior to determining the Stokes emissivities and calculating the radiative transfer for the jet models, certain aspects of the data were modified. Here we outline the modifications made and justify their necessity.

CHAPTER 4

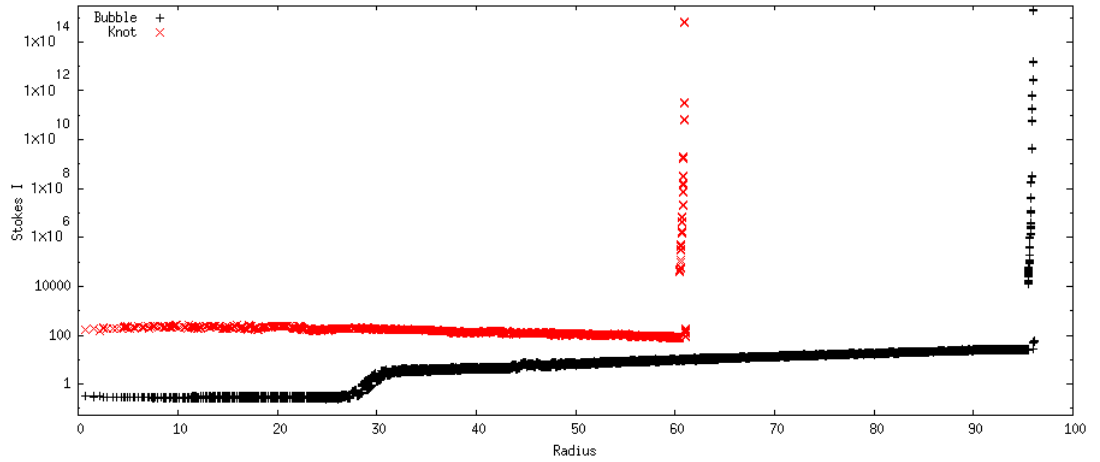


Figure 4.1: The Stokes I emissivity of each pixel, as a function of radius, for x - y slices through the first bubble and pinch of the cold model at a viewing angle of 5° .

4.1.1 Radial Jet Trimming

As detailed in Section 3.3, after the parallelepipeds for the r - z plane have been determined from the velocity field in the same plane, they are projected onto the three-dimensional Cartesian grid, and their contribution to the Stokes emissivities is then determined. It was found that the simulated images contained pixels of intense brightness near the edge of the jets, however. The pixels in question have extremely large compression factors $V'^{-11/3}$, at least three orders of magnitude larger than the average values; this occurred because these pixels were within the shear layer, and thus the parallelepiped vectors were stretched parallel to the z -axis, causing these large volume factors. The Stokes I emissivity is found to increase greatly towards the edge of the jet for these pixels, and Figure 4.1 shows this for the cold model in two separate x - y slices at the first positions of maximal jet radius (a “bubble”) and minimal radius (a “pinch”) after the inlet plane. These shear-layer pixels were removed from the simulated images by decreasing the initial radial extent of the jet (mentioned in Section 3.1) by a constant of the order of a few pixels; Figure 4.2 shows the final radial extent that we consider each jet to be bounded by.

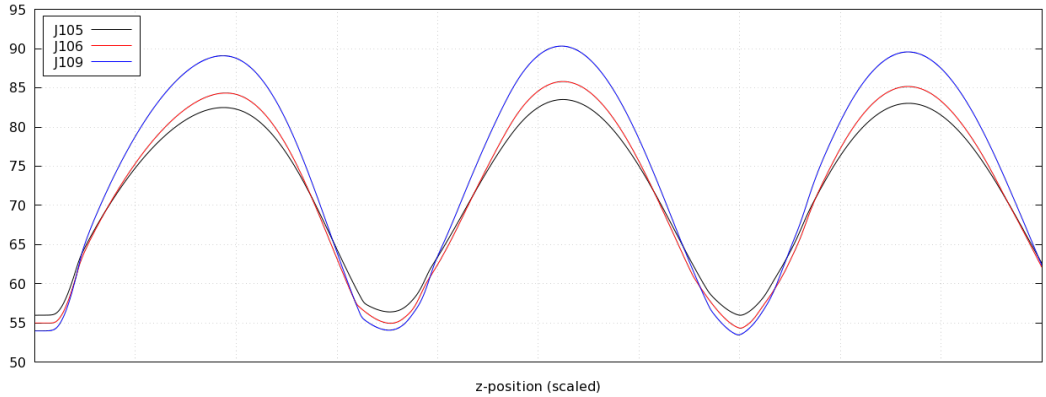


Figure 4.2: The outermost radii of pixels that we consider to be part of the jets. The horizontal axis has been scaled such that the maximal and minimal radii of the different models are aligned.

4.1.2 Gaussian Smoothing

In practice, the streamline method of parallelepiped monitoring (Section 3.3) was found to produce striated patterns in the parallelepiped vector components when using unprocessed FGMP velocity data, e.g. as can be seen in Figure 4.3. These striations were found to occur after the first, collimating, shock surface in each simulation, and are believed to be a result of how the streamlines cross the first recollimation shock. To demonstrate this, we show the profile of the a_x components of the hot jet model, focusing on six streamlines that terminate at $z = 860$, with radial positions $r = 33$ – 38 ; these streamlines are shown in Figure 4.4 (in which the streamlines are labelled A–F). When plotting the velocity difference between each end of the \mathbf{a} vector, as a function of velocity along these streamlines (Figure 4.5), it can clearly be seen streamlines A, C, and E have notably smaller velocity differences between the marker particles for \mathbf{a} as they cross the recollimation shock, compared to those of streamlines B, D, and F. It was also found that these striations were visible in the simulated observations, and so their presence could not be overlooked; in Figure 4.6, for instance, striations may be seen in the total polarization of the cold model at a viewing angle of 5° .

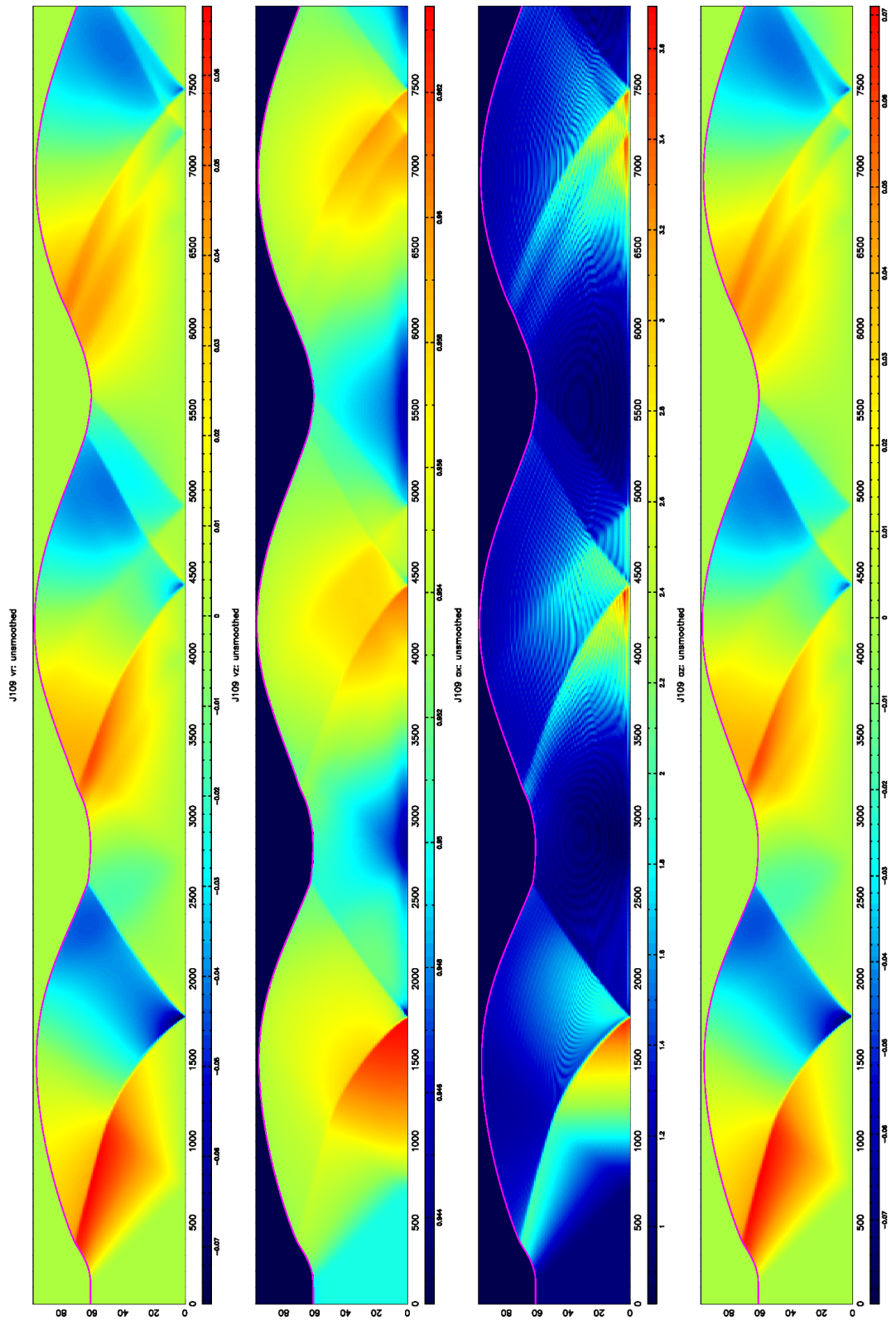


Figure 4.3a: The components of radial and axial velocity, and parallelepiped components a_x and a_z , for the cold model are shown from left to right, in that order.

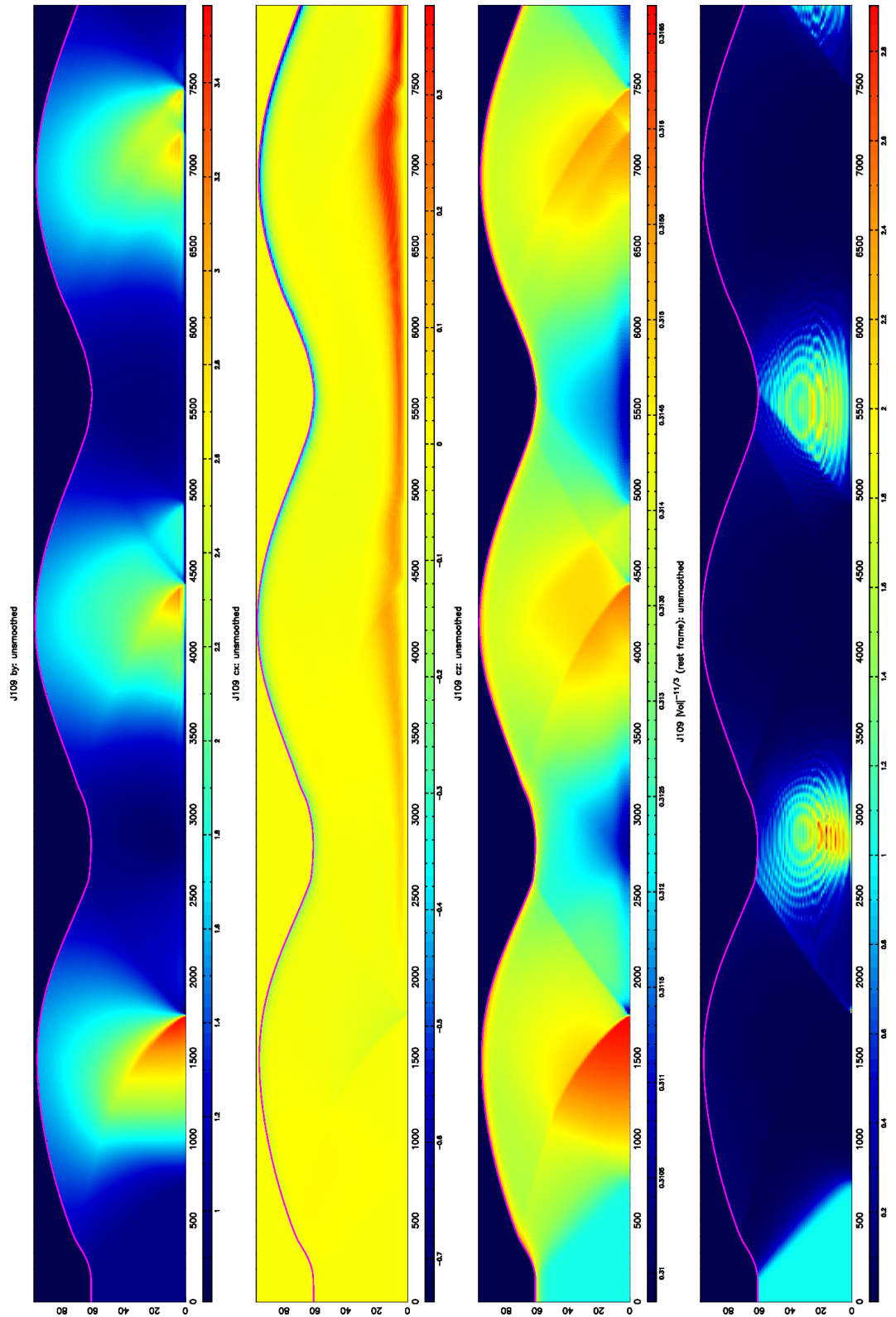
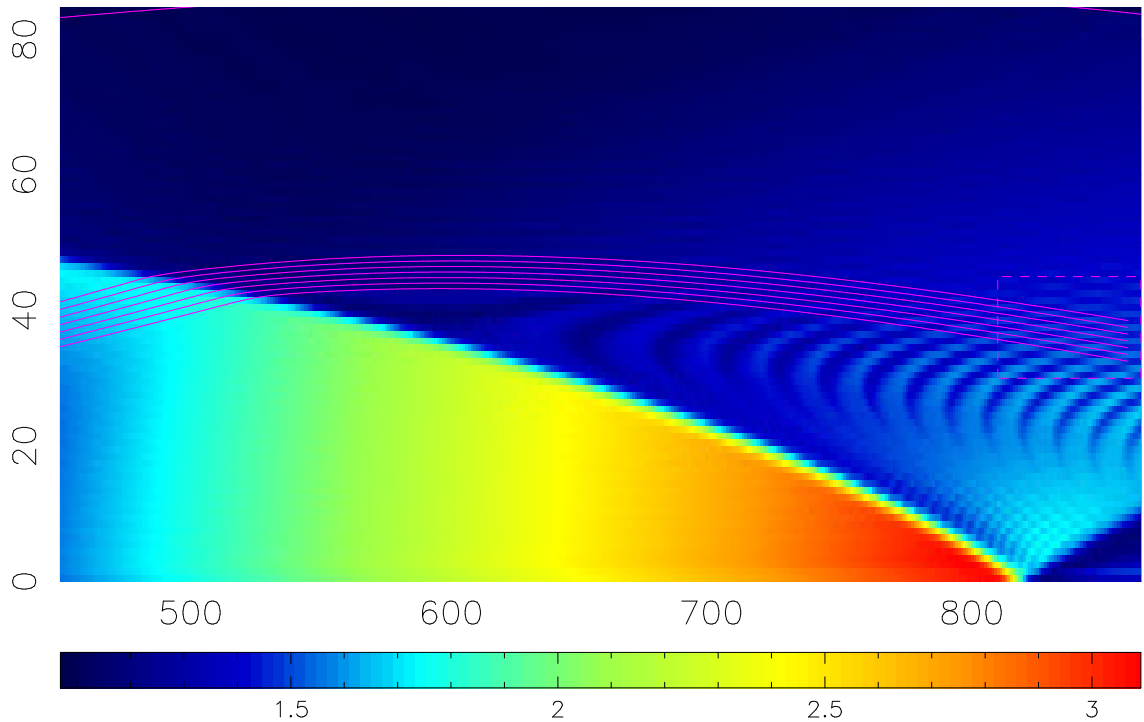
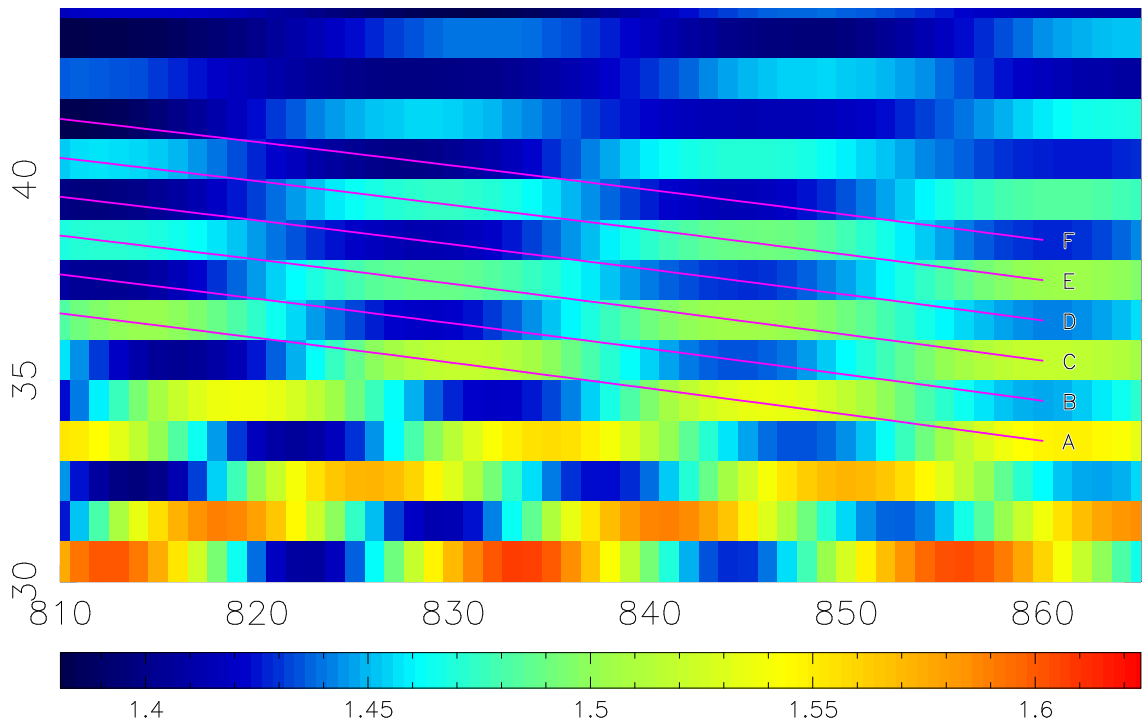


Figure 4.3b: The parallelepiped components b_y , c_x and c_z , and the compression factor $V^{-11/3}$, for the cold model are shown from left to right, in that order.



(a) Large-scale a_x profile, with a selection of streamlines



(b) Zoom-in of the selected streamline termination points

Figure 4.4: Six streamlines (A–F) are overplotted on the profile of a_x for the hot jet model. The zoomed-in image clearly shows how the a_x values oscillate with the striation layers.

CHAPTER 4

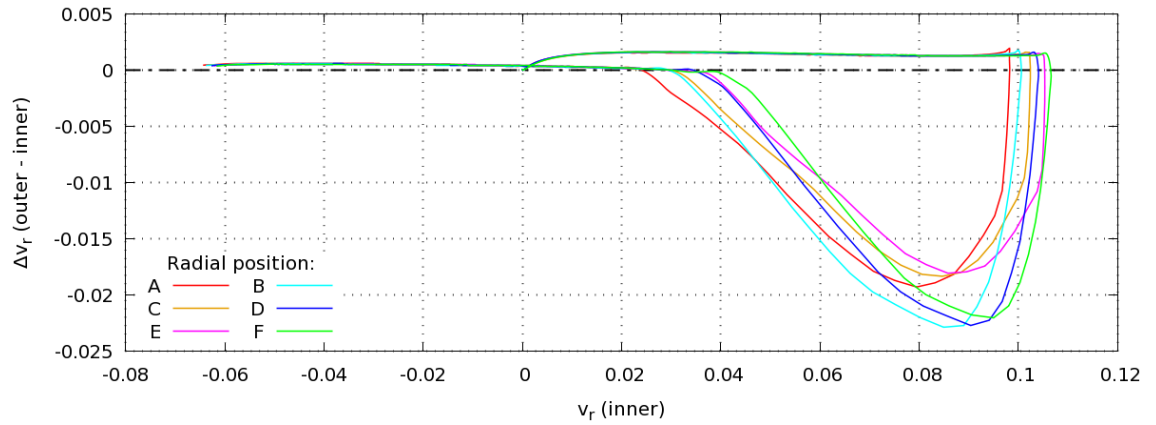


Figure 4.5: The difference in radial velocity between both ends of the \mathbf{a} vector marker particles, as a function of radial velocity of the inner marker particle, show a clear alternating pattern at the point of maximum velocity difference.

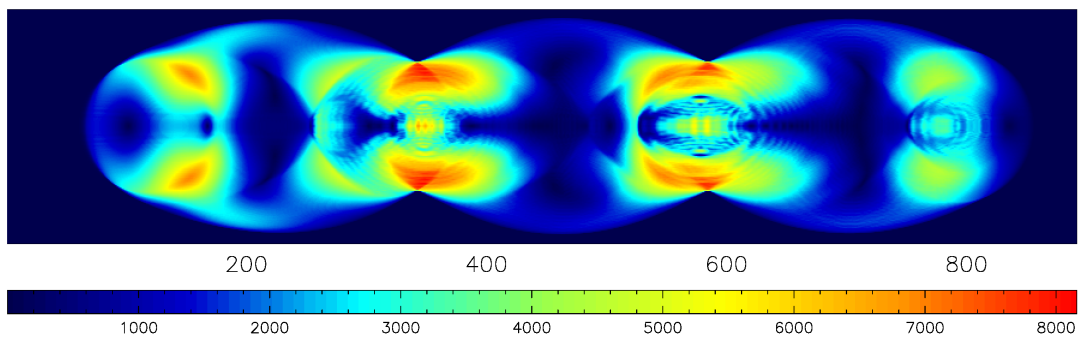


Figure 4.6: Simulated total polarized emission image obtained from the unsmoothed parallelepipeds determined for the cold model when viewed at 5° .

CHAPTER 4

Two different data-smoothing approaches were considered to diminish the presence of striations in the post-shock parallelepiped vector components; the solutions considered were (i) smoothing the velocity profiles before determining the parallelepipeds, or (ii) smoothing the parallelepipeds, before projecting them onto the three-dimensional Cartesian grid. Smoothing the velocities before advection was found to reduce radial velocities close to the jet axis, due to the cancellation of radial velocities about the jet axis. This would artificially modify the jet structure, meaning that our steady state assumption may be rendered invalid; in order to avoid this possibility, we choose to smooth the parallelepiped vector components we calculated, prior to determining the radiative transfer of the model.

Using an elliptical Gaussian kernel, with a cut-off radius of 4σ , the level of smoothing chosen for each jet model was such that the striated patterning present in parallelepiped component a_x between the first two RSs is only faintly visible after smoothing; by smoothing the parallelepipeds as little as possible, we aimed to preserve as much information as possible, while reducing the oscillatory artefacts permeating the parallelepiped distributions. The full width at half maximum (FWHM) of the elliptical kernel was chosen to be 6 pixels in the radial direction and 40, 60, and 80 pixels in the axial direction for the hot, intermediate, and cold models respectively. A comparison between the smoothed and unsmoothed a_x parallelepiped component for the cold model is shown in Figure 4.7, and the average difference between the smoothed and unsmoothed parallelepiped components across all models was found to be 2.2%, where components smaller than 10^{-6} are neglected, and the discrepancies for the principal components (i.e. a_x , b_y , and c_z) are significantly below this.

4.2 Presentation of the Data

Before discussing the images produced for the different models, we first give a general

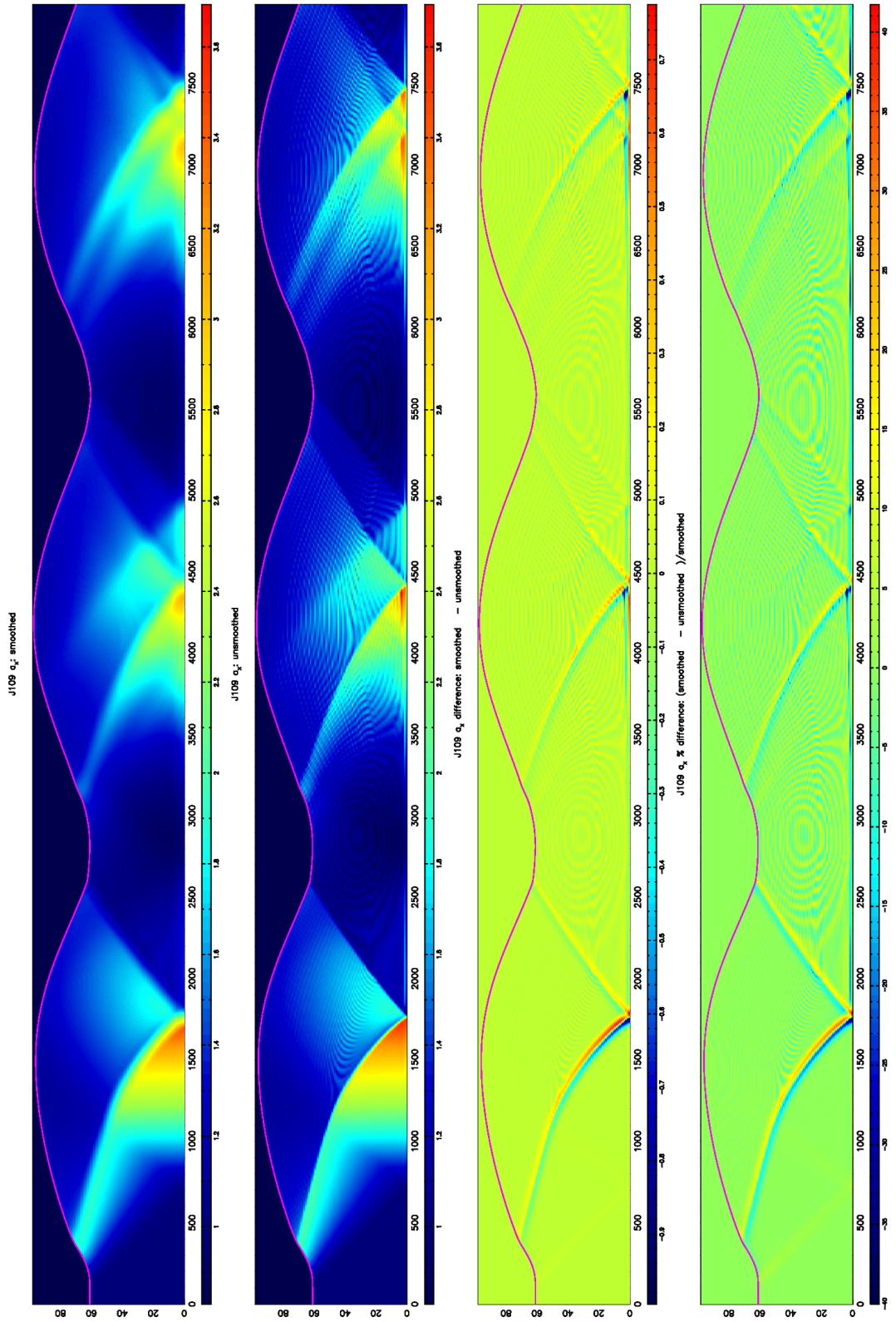


Figure 4.7: Profiles of a_x in the cold model after and before smoothing, and the difference, and percentage difference, between them from left to right, in that order.

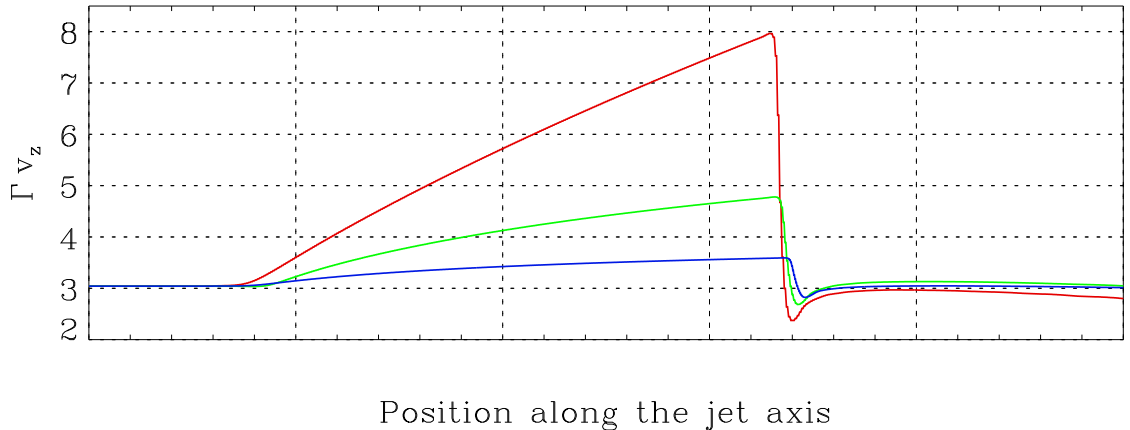


Figure 4.8: On-axis profile of Γv_z across the first bubble of each model. The red, green, and blue lines correspond to the hot, intermediate, and cold models respectively, and the horizontal axes are scaled independently.

description of the simulations, and then describe results for lines of sight through the bubbles and pinches of the jet models.

The shock spacing is closer in the hotter jet models, which is expected since the shock spacing is proportional to the Mach number of the flow (e.g. Falle & Wilson, 1985); the Mach numbers are lower for the hotter simulations as they have higher sound speeds. The recollimation shocks present within the hotter jets are also stronger than those in the colder jets, as can be seen in Figure 4.8, which shows the product Γv_z along the jet axis of each model; we use $\Delta(\Gamma v_z)/\Delta z$ as a proxy indicator of the shock strength, and find the hotter models to have significantly larger jumps in Lorentz factor (and thus stronger shocks) than the colder models. The RSs in the hotter models are more perpendicular to the jet axis, and the flows experience greater acceleration and deceleration due to the greater proportion of internal energy available for conversion to kinetic energy (see Figure 4.8).

We also find that imprints of the recollimation shocks are clearly visible in the parallelepiped vector components, but they have a limited impact on the total parallelepiped volume; the first seven panels of Figure 4.9 show v_r , v_z and the observer frame parallelepiped vector components of the cold jet in the r - z plane, and the

CHAPTER 4

final panel shows the jet's rest-frame volume compression factor $V'^{-11/3}$, to which the emissivities in Equation 3.7 are proportional. While the volume factor can be seen to increase slightly across the decollimating shock front in the cold jet, the volume factor is ~ 10 times greater between the RSs, where the jet is most pinched.

As noted by Fuentes et al. (2018), the multiple RSs seen within a single simulation appear similar, but because crossing a shock is an irreversible process, and entropy is not conserved, the shocks do differ from one to the next. After the first RS, the structure of each shock is also more complex, consisting of a principal conical shock together with one or more secondary overlapping conical shocks; these secondary shocks are a result of reflections from the simulation boundary.

As a result of the adiabatic expansion of the gas, and the flux-freezing of the magnetic field, the emissivity depends on the volume compression factor $V'^{-11/3}$, where V' is the rest-frame parallelepiped volume. This is most greatly enhanced at the pinches along the jet, where the plasma is most compressed.

The pattern of the parallelepiped components depends on two factors, the first of which is the general background flow of the jet. Supersonic flows accelerate along diverging streamlines and decelerate along converging streamlines (e.g. Paterson, 1984, contrary to the behaviour of a subsonic flow); this may cause growth, or reduction, of parallelepiped vector components as the ends of a vector follow streamlines that are divergent, or convergent, respectively. The second factor affecting the parallelepiped vector profiles is the presence of shocks within the flow. A parallelepiped vector advecting through a shock surface within a velocity field will be deformed when one end of the vector crosses the shock surface before the other end.

As an example of these factors, when the flow enters the bubble, the vector component a_x , for instance, can be seen to increase, but is sharply reduced by the oblique shock front. This occurs because the outer end of the \mathbf{a} vector meets the first (collimating) shock surface in the RS, and is deflected towards the jet axis (to

CHAPTER 4

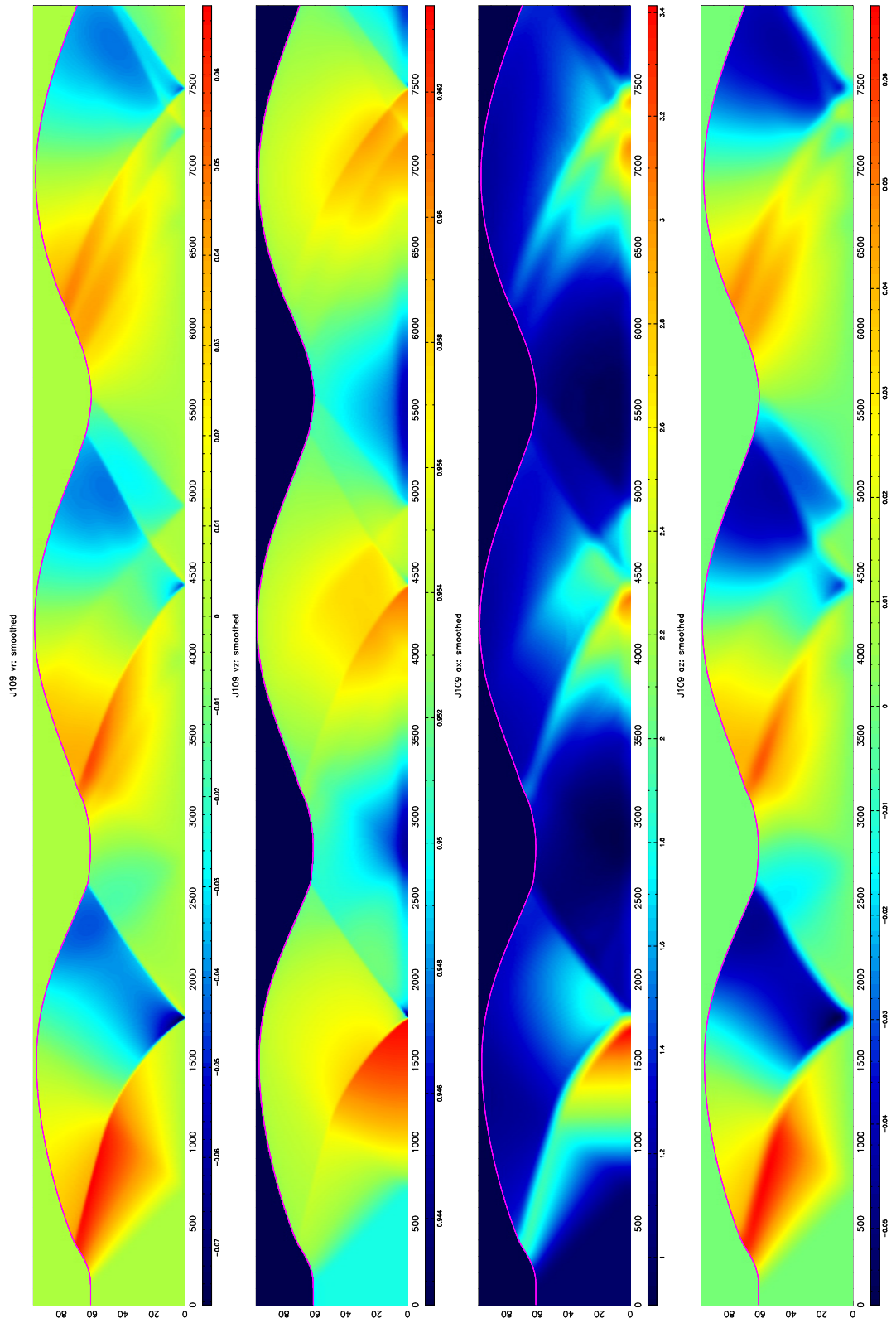


Figure 4.9a: Components of radial and axial velocity, and smoothed parallelepiped components a_x and a_z , for the cold model are shown from left to right, in that order.

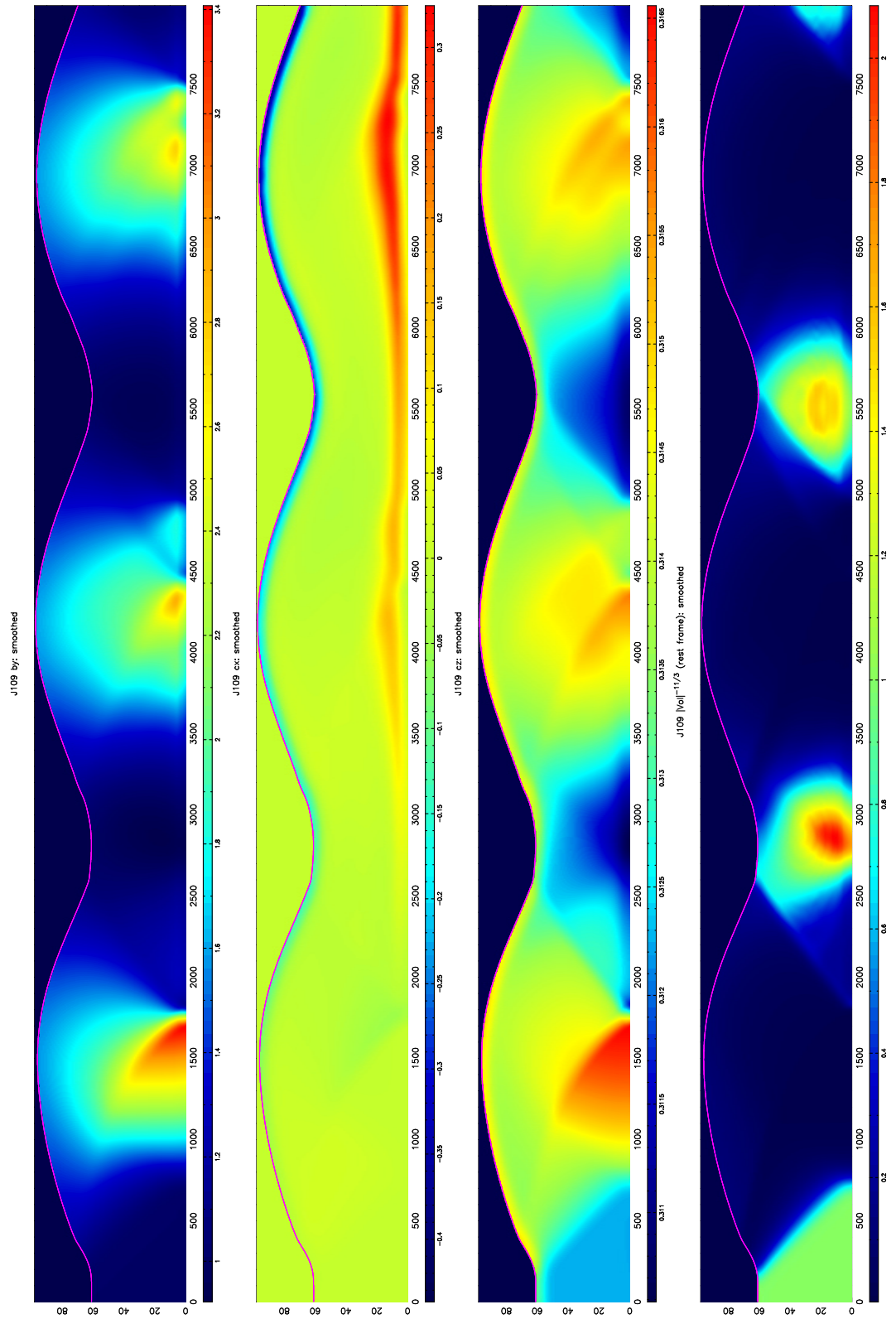


Figure 4.9b: Smoothed parallelepiped components b_y , c_x and c_z , and the compression factor $V'^{-11/3}$, for the cold model are shown from left to right, in that order.

CHAPTER 4

some extent), before the inner end has encountered the shock. For a time, the inner part of the parallelepiped vector continues moving outwards with a greater radial velocity than the outer end of the vector, meaning that a_x is decreased after the shock. Likewise, c_z can be seen to increase as the flow accelerates towards the RS of the jet, but the relative changes in v_z are much lower than those seen in v_r , and as such the increase in c_z is modest by comparison with that seen in a_x . As the flow is sharply decelerated by the oblique shock wave, there is a corresponding decrease in c_z and, as expected from the rather modest variation in v_z throughout each jet, the impact of each shock can be seen in the small variations in c_z . As a result of the small v_z gradients, the c_z vector components remain relatively constant throughout the models.

We now verify that the parallelepiped monitoring is accurate for the FGMP simulations. Figure 4.10 shows a comparison of the normalized rest-frame density of the jet material ρ/ρ_0 and the inverse rest-frame volume of each parallelepiped $1/V'$; the data plotted are taken where each jet model is most pinched after its first RS. The correspondence between the density and inverse volume of each pixel clearly shows that the streamline approach is a valid measure of the parallelepiped deformation.

4.2.1 Simulated Lines of Sight

Our simulated images differ significantly from the results of semi-dynamical modelling (e.g. Cawthorne, 2006; Cawthorne et al., 2013) due to the different assumptions behind the two approaches. In the earlier semi-dynamical work, it was assumed that the jet emitted only near the shock surface, due to synchrotron losses as the plasma moved away; here we neglect this spectral ageing altogether. In these models the brightest parts of the jets are where the flow is pinched, between the successive RSs. This pinching effect was completely ignored in the semi-dynamical simulations. This

CHAPTER 4

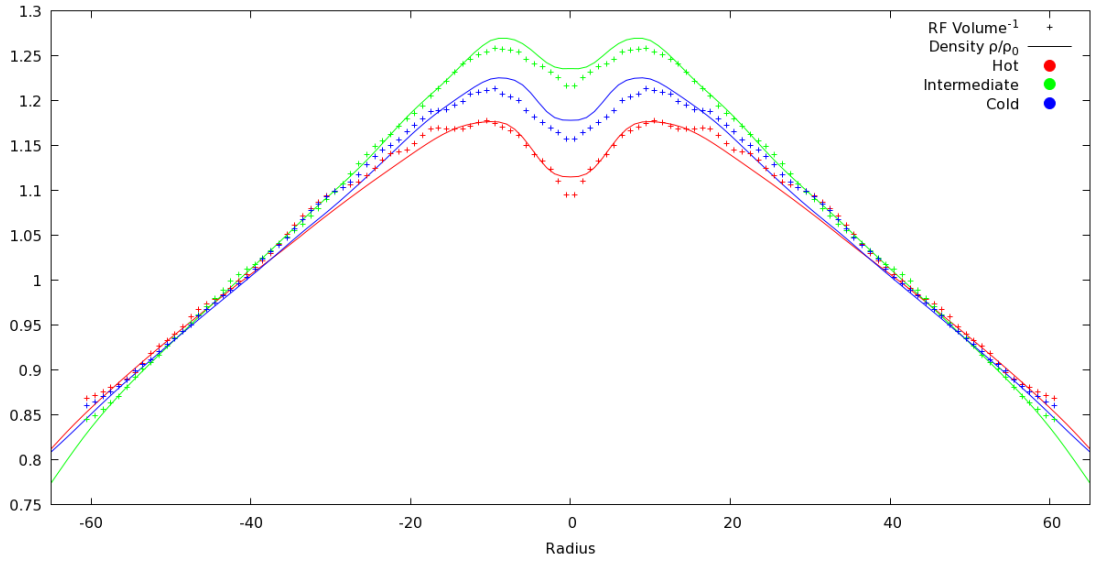


Figure 4.10: The rest-frame normalized density ρ/ρ_0 (solid lines) and the inverse of the rest-frame parallelepiped volume $1/V'$ (+ symbols) are plotted on the same axes for lines through the pinch points of the hot, intermediate and cold models (red, green and blue colours, respectively).

means that the present work presents another perspective based on a different set of assumptions. It may be that the semi-dynamical models provide a better prediction of observations at high frequencies ($\gg 1$ GHz) where synchrotron lifetimes are likely to be shorter.

It should be noted that for the most part, the parallelepiped values do not depart by a large factor from their cubic rest-frame initialization, so the fractional polarization observed within the jets is often fairly low, often less than 10% and rarely greater than 20%. This is in agreement with observations, and the replication of such modest levels of polarization was one of the major motivations for this work. However, this tends to mitigate against simple explanations for the polarization structures we observe. Particularly for small viewing angles, in which the lines of sight pass through several regions with different parallelepiped vector configurations, the resultant polarization cannot be explained in terms of any one parallelepiped shape. Nonetheless, we have tried to show how some of the trends with viewing

CHAPTER 4

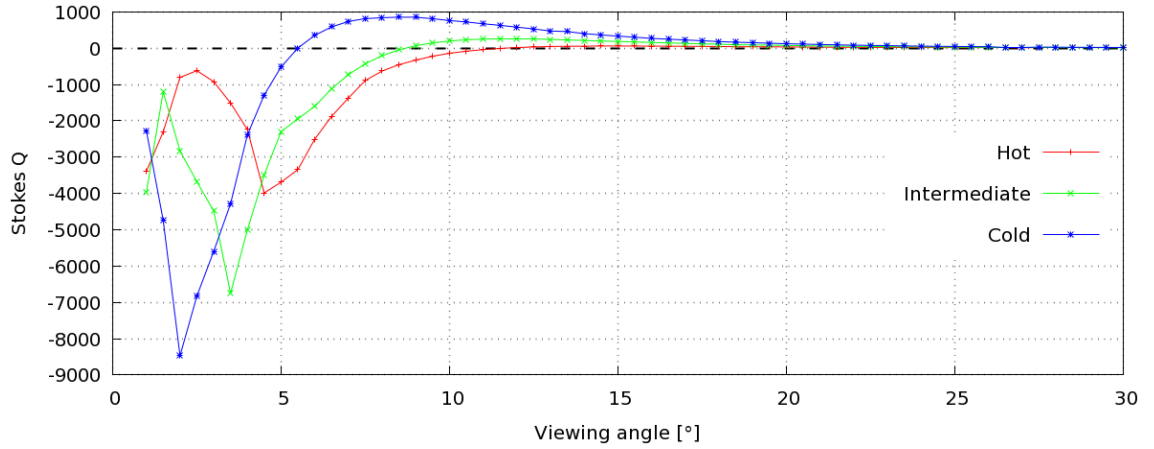


Figure 4.11: Stokes Q for lines of sight that intersect the widest part of the first bubble at the centre of the jet, as a function of the viewing angle.

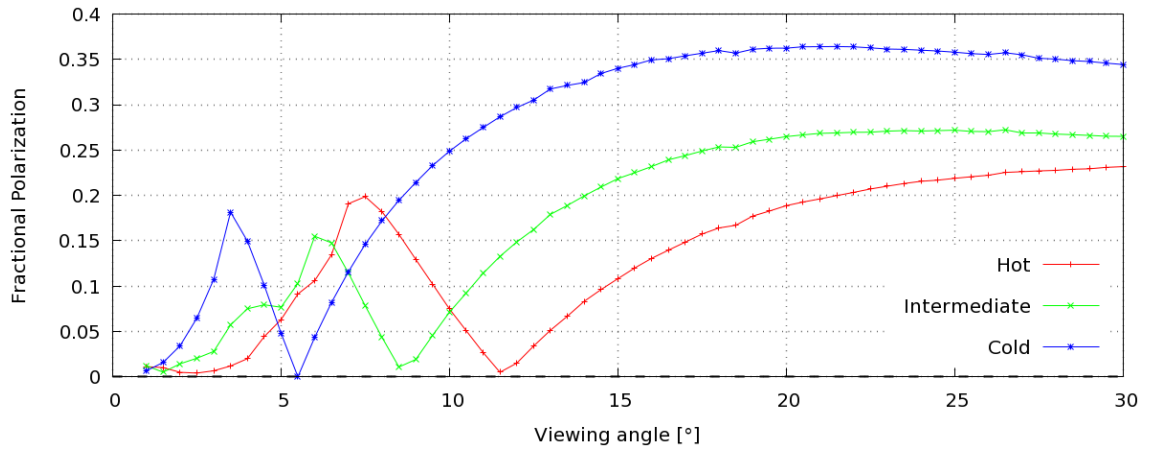


Figure 4.12: Fractional polarization for lines of sight that intersect the widest part of the first bubble at the centre of the jet, as a function of the viewing angle.

angle can be explained in terms of the parallelepiped components at the locations of the bubbles (i.e. where the jet is most expanded) and the pinch points.

To investigate the polarization properties of the first bubble and pinch point of each model, we determine the Stokes parameters along a range of lines of sights with different viewing angles, intersecting the same point at the centre of the jet. Figures 4.11 and 4.13 show the average Stokes Q per cell along the line of sight, with the line of sight intersecting the centre of the first bubble and pinch in each jet respectively; Figures 4.12 and 4.14 show the fractional polarization for the same

CHAPTER 4

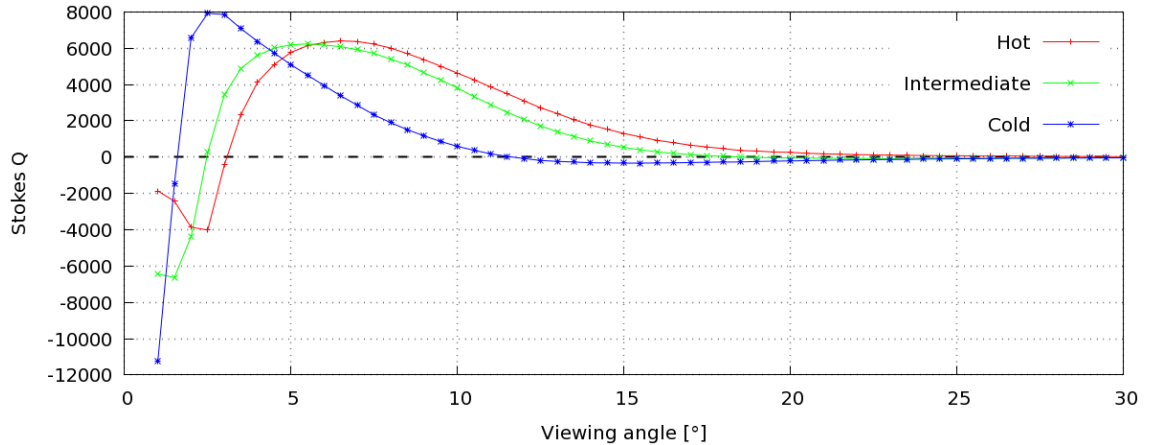


Figure 4.13: Stokes Q for lines of sight that intersect the narrowest part of the first pinch point at the centre of the jet, as a function of the viewing angle.

lines of sight through the bubble and pinch respectively. The lines of sight we use here all lie in the x - z plane, such that there will be no component of velocity in the $\pm y$ -direction; consequently, the \mathbf{m}' vector will always be parallel to $\pm \hat{\mathbf{j}}$, and \mathbf{l}' will always lie in the x - z plane. Hence, the components a'_m , b'_l , and c'_m will be identically zero (Section 3.3), and therefore Stokes U will also be zero, meaning that (in this special case) Stokes $|Q|$ is equal to the total polarized flux for a given line of sight.

All three simulations follow the same pattern in the variation of polarization as a function of viewing angle θ ; this can be seen within the bubble in Figure 4.11 for total polarization, and the fractional polarization in Figure 4.12. Within the pinch point, the polarization is shown in Figure 4.13, and the fractional polarization is shown in Figure 4.14.

The variation of Stokes Q with θ occurs because (i) different lines of sight intersect regions with differing parallelepiped vectors, and (ii) as the lines of sight change, so the contributions to the sky-plane projections of the parallelepiped vectors also change.

Within the bubble, for small viewing angles ($\theta < 5.5^\circ$ in the cold model) Q is negative, corresponding to EVPA perpendicular to the projected jet direction (or a projected magnetic field predominantly parallel to the jet direction). At larger

CHAPTER 4

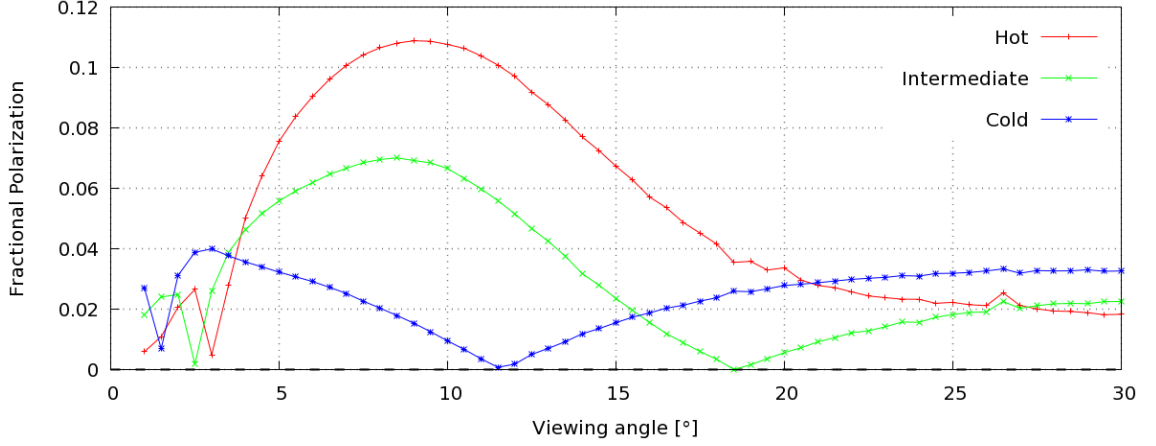


Figure 4.14: Fractional polarization for lines of sight that intersect the narrowest part of the first pinch point at the centre of the jet, as a function of the viewing angle.

angles Q becomes positive (i.e. EVPA parallel to the projected jet direction), but smaller, and the fractional polarization increases (see Figures 4.11 and 4.12).

We will now attempt to illustrate the causes of this transition with reference to the rest-frame parallelepiped vectors $\tilde{\mathbf{a}}'$, $\tilde{\mathbf{b}}'$, and $\tilde{\mathbf{c}}'$, where the tilde denotes that the parallelepiped vector, or component thereof, has been divided by the rest-frame volume of the parallelepiped and averaged along the line of sight. The variation of the principal parallelepiped vector components of $\tilde{\mathbf{a}}'$, $\tilde{\mathbf{b}}'$, and $\tilde{\mathbf{c}}'$ (i.e. \tilde{a}'_x , \tilde{b}'_y , and \tilde{c}'_z) through the bubble and pinch points are shown in Figures 4.15 and 4.16 respectively. At small viewing angles, say $\theta = 2.5^\circ$, $\tilde{a}'_x \approx 0.69$, $\tilde{b}'_y \approx 0.63$, and $\tilde{c}'_z \approx 0.52$ (the other components being small or zero). With the velocity $\mathbf{v} \approx v_z \hat{\mathbf{k}} \approx 0.96 \hat{\mathbf{k}}$, the rest-frame angle between the line of sight and the velocity vector is $\phi' \approx 17^\circ$. Thus $\tilde{a}'_l = \tilde{a}'_x \cos(\phi') \approx 0.66$, $\tilde{b}'_m = \tilde{b}'_y \approx 0.63$, and $\tilde{c}'_l = -\tilde{c}'_z \sin(\phi') \approx -0.15$. Hence $\tilde{a}'_l{}^2 + \tilde{c}'_l{}^2 > \tilde{b}'_m{}^2$, if only by a small margin, implying that the electric field is predominantly perpendicular to the jet axis, with fairly weak fractional polarization. (The significance of this inequality is explained in Section 3.2.2.)

At a larger viewing angle, e.g. $\theta = 15^\circ$, the cold model has principal vector components $\tilde{a}'_x \approx 0.43$, $\tilde{b}'_y \approx 0.55$, and $\tilde{c}'_z \approx 0.30$. Neglecting the v_x velocity component

CHAPTER 4

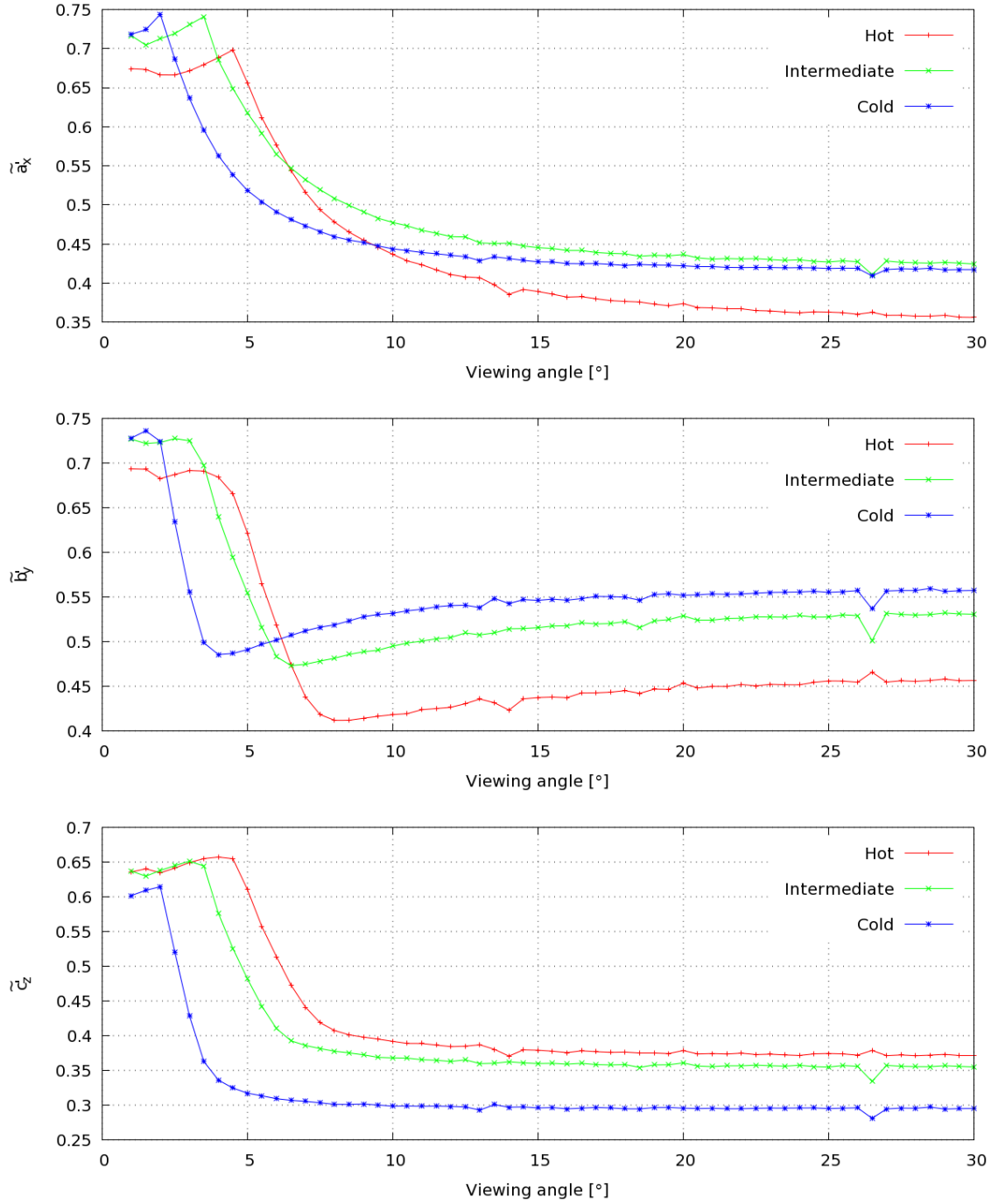


Figure 4.15: For lines of sight through the centre of the first bubble in each model, the average parallelepiped components \tilde{a}_x , \tilde{b}_y , and \tilde{c}_z are plotted as a function of viewing angle (from top to bottom respectively).

CHAPTER 4

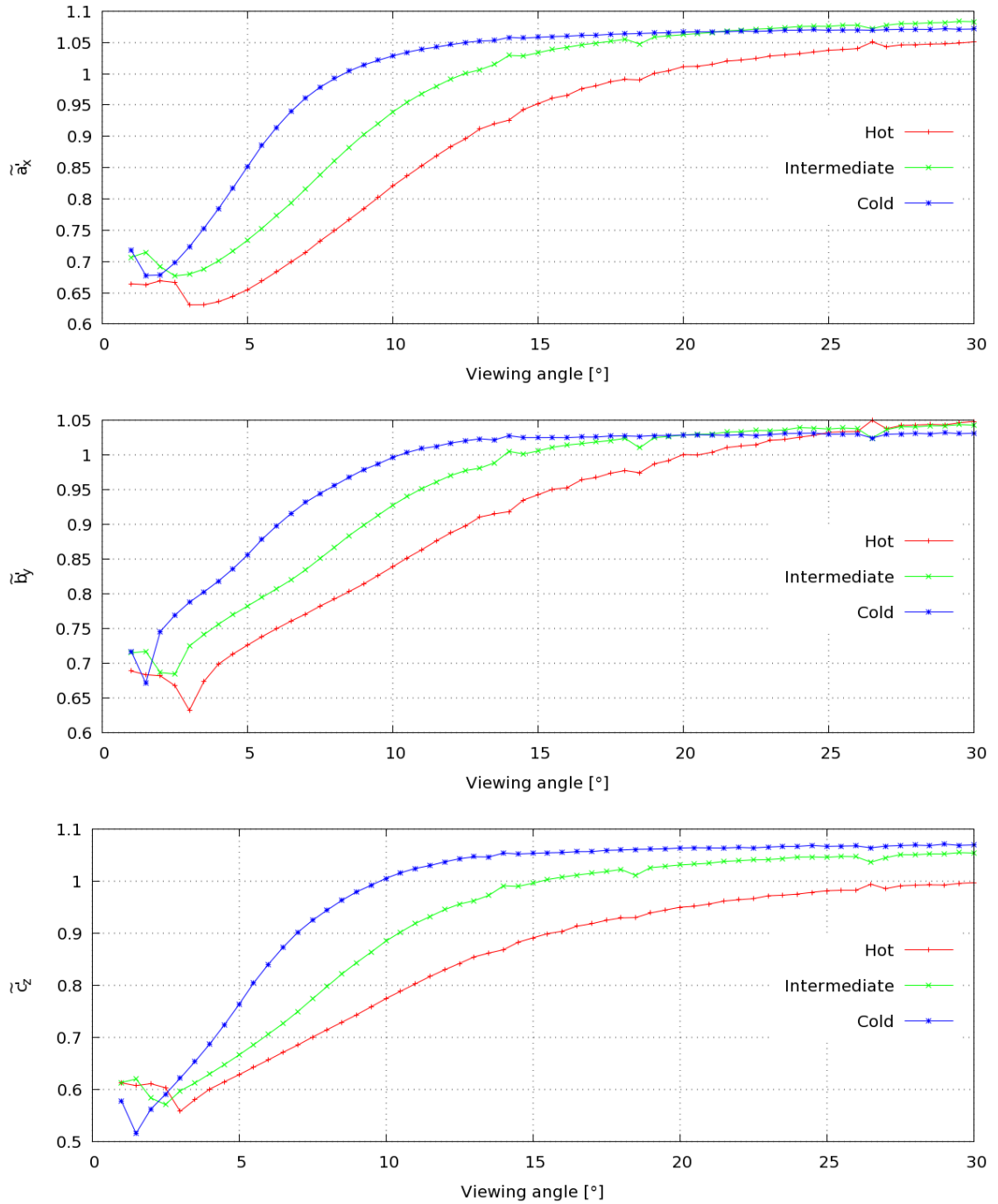


Figure 4.16: For lines of sight through the centre of the first pinch point in each model, the average parallelepiped components \tilde{a}_x , \tilde{b}_y , and \tilde{c}_z are plotted as a function of viewing angle (from top to bottom respectively).

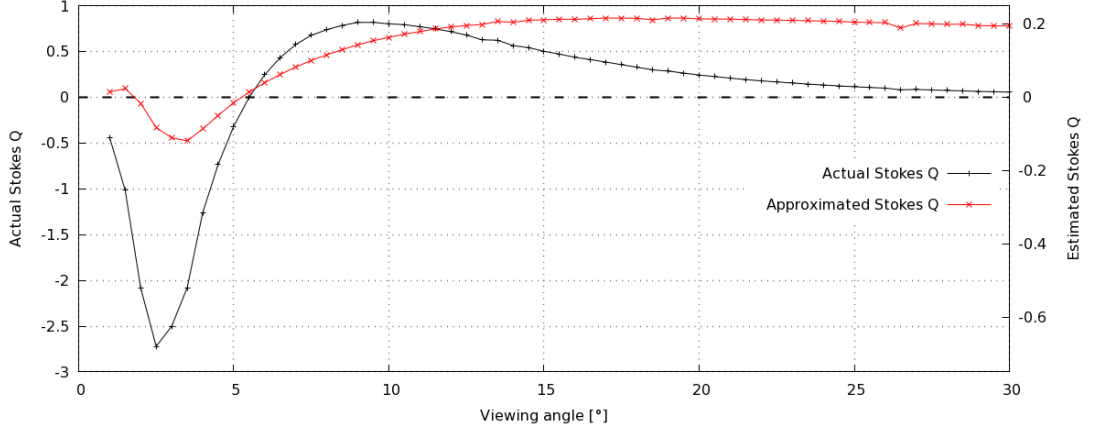


Figure 4.17: The average Stokes Q emissivity per cell along a line of sight through the centre of the bubble in the cold jet is plotted as a function of viewing angle (black line, left axis). An estimate of Stokes Q for the same lines of sight, determined using the averaged principal parallelepiped components and the Doppler brightening factor \mathcal{D}^3 , is also plotted (red line, right axis).

as before, we obtain $\phi' \approx 85^\circ$. Then $\tilde{a}'_l = \tilde{a}'_x \cos(\phi') \approx 0.04$, $\tilde{b}'_m = \tilde{b}'_y \approx 0.55$, and $\tilde{c}'_l = -\tilde{c}'_z \sin(\phi') \approx -0.30$, so clearly $\tilde{a}'_l{}^2 + \tilde{c}'_l{}^2 < \tilde{b}'_m{}^2$ by a large margin, indicating that the polarization is perpendicular to that calculated for the previous viewing angle, and that the fractional polarization is much greater. Here, although all of the vector components have decreased from their values at $\theta = 2.5^\circ$ due to the pinching of the jet, the most dominant effect has been on the projection of the $\tilde{\mathbf{a}}'$ vector, \tilde{a}'_l , since the viewing angle in the rest frame has increased to $\phi' \approx 90^\circ$, and so $\tilde{a}'_l \approx \tilde{a}'_x \cos(\phi') \approx 0$.

In the pinch points, for small viewing angles (but $\theta > 1.5^\circ$ in the cold model), Stokes Q is positive because, initially, $\tilde{b}'_m \approx \tilde{b}'_y$ is greater than \tilde{a}'_x , and the projection of \tilde{c}'_z contributes little to \tilde{c}'_l . As the viewing angle increases, however, the contribution to \tilde{c}'_l from \tilde{c}'_z increases, and this tips the balance in favour of a negative Q . Thus, the EVPA changes from being parallel to the projected jet axis at small viewing angles (with positive Stokes Q), to being perpendicular to this axis at larger angles in the cold and intermediate models; in the hot model, Stokes Q remains positive while tending to zero as the viewing angle approaches 90° .

CHAPTER 4

Figure 4.17 shows the average Stokes Q , per cell along each line of sight, as a function of viewing angle; also shown is estimate of Stokes Q for the same lines of sight, determined using only the principal components of the parallelepipeds, averaged along the line of sight (as was done for our previous examples). These simple analyses do not account for the full range of factors affecting the emissivities as the line of sight changes with viewing angle; for example, we have implicitly assumed that only the parallelepiped vectors contribute significantly to the polarization, thus ignoring the Doppler brightening of the polarization. This effect is greatest for smaller viewing angles, and if Doppler boosting were to be incorporated, we would see a decrease in polarization at the higher viewing angles, and a large increase in polarization for small θ , resulting in even better agreement with the actual values. Bearing this in mind, we can see that the sign of the approximate Stokes Q with viewing angle agrees with the actual profile of Stokes Q , especially at low angles. In short, this shows that our simple analysis of the polarization, with respect to the averaged, principal parallelepiped components provides reasonable results, even when Doppler brightening is neglected.

The three curves corresponding to the hot, intermediate, and cold jets in each of Figures 4.11–4.14 follow a similar pattern*, with key features (e.g. turning points and axis crossings) occurring at larger viewing angles for the hotter models. It seems that this is due to the fact that the shock spacing is lower and the opening angles of the shocks are greater in the hotter models. Thus, lines of sight passing through corresponding points in the structures will correspond to larger viewing angles for the hotter models. This is shown by Figure 4.18, in which the lines of sight that intersect the bubble at the centre of the jet and the pinch point at the edge of the jet are shown. The viewing angles for this line of sight in the cold, intermediate, and hot models were found to be $\theta \approx 2.3^\circ$, 4.0° , and 5.4° respectively. These angles

*This does not include the hot model within the pinch point; while the cold and intermediate models undergo transitions from positive Stokes Q to negative at $\theta > 10^\circ$, Q remains positive for the hot model, and tends to zero as the viewing angle approaches 90° .

CHAPTER 4

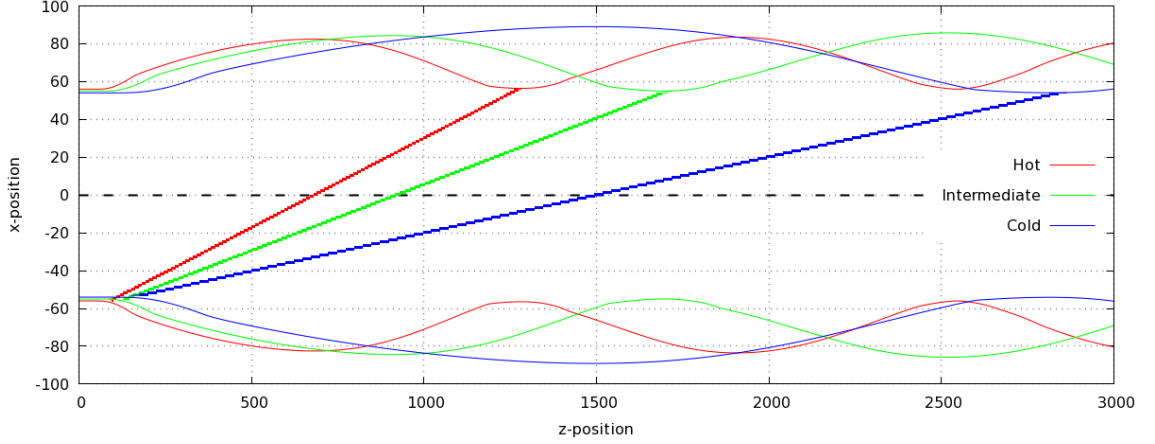


Figure 4.18: The lines of sight intersecting the bubble at the centre of the jet, and the pinch point at the edge of the jet, are plotted for the hot, intermediate and cold jet models; the edges of the jet for each model are also shown.

approximately correspond to local minima of Stokes Q in Figure 4.11.

Figures 4.13 and 4.14 show that the hotter jets have greater fractional polarization for small viewing angles in the pinch points of the jets, while the peak fractional polarizations of the cold model are about the same before and after the transition from positive to negative Q . The fractional levels of polarization present within this region of the jet are fairly low ($\lesssim 10\%$) for each model at all viewing angles; this is as expected, as on average, the parallelepipeds along each line of sight are found to be approximately cube-shaped (see Figure 4.16).

Figures 4.12 and 4.14 show that, in general, the fractional polarization for lines of sight through the bubble are higher than for the pinch point. Also, the fractional polarizations are higher for colder models at the bubbles. Conversely, when considering the most polarized models for lines of sight through the pinch points, the hotter models have greater fractional polarizations (until $\theta \approx 20^\circ$, after which the cold model has the highest polarization, Figure 4.14).

4.2.2 The Simulated Images

Many images of observed radio sources show contours of total intensity, over-plotted with sticks of length proportional to the polarized intensity at that point, and orientation aligned with the EVPA of the polarization. We also implement this scheme, over-plotting these polarization sticks onto the total intensity profiles of the jet. We have simulated images of the hot, intermediate, and cold models at $\theta = 5^\circ$, 10° , and 20° , with the length of the sticks normalized to the maximum polarization present for that model at that viewing angle.

As stated previously, we focus predominantly on the first bubble and pinch of the jets, but in some cases (e.g. the hot model at $\theta = 5^\circ$) the proximity of successive shocks on the sky-plane means that the simulated images include multiple shocks.

Hot Jet Images

Figures 4.19–4.21 show panels containing Stokes I with EVPA sticks, the total polarized flux P , and fractional polarization $\Pi = P/I$ respectively, for part of the hot model at $\theta = 5^\circ$, 10° , and 20° . If we consider Figure 4.19, it can be seen that for each image, P (given by the lengths of the EVPA sticks, scaled independently for each viewing angle) is consistently highest near the jet pinch points, where the electric vectors in the sky plane remain predominantly parallel to the projected jet axis. These observations are in agreement with our findings from Figure 4.13, which shows that for all viewing angles through the centre of the bubble, neglecting $\theta \lesssim 1.5^\circ$, Stokes Q remains positive (i.e. the electric vectors remain parallel to the projected jet axis). It should be noted, however, that the polarization around the centre of the pinch point becomes more radial in shape as the viewing angle increases. The polarization changes in the centre of the bubbles also follows a slightly complicated pattern. At $\theta = 5^\circ$, P in the bubble is of a similar magnitude (but perpendicular orientation) to that of the pinch point; at higher viewing angles, however, P in the

CHAPTER 4

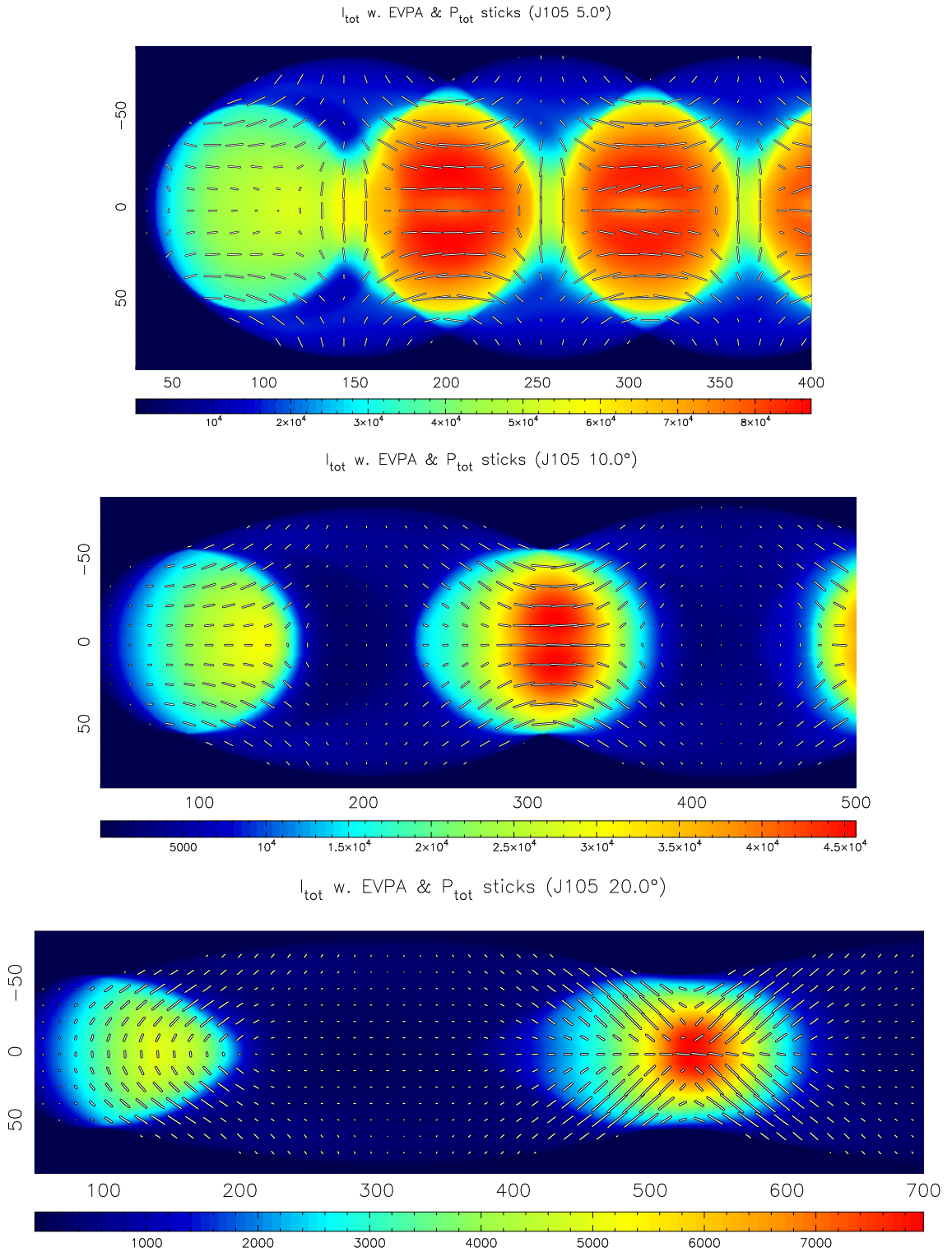


Figure 4.19: Simulated images of the total flux of the hot model, overlaid with polarization sticks, are shown for viewing angles of (a) 5°, (b) 10°, and (c) 20°, from top to bottom, respectively.

CHAPTER 4

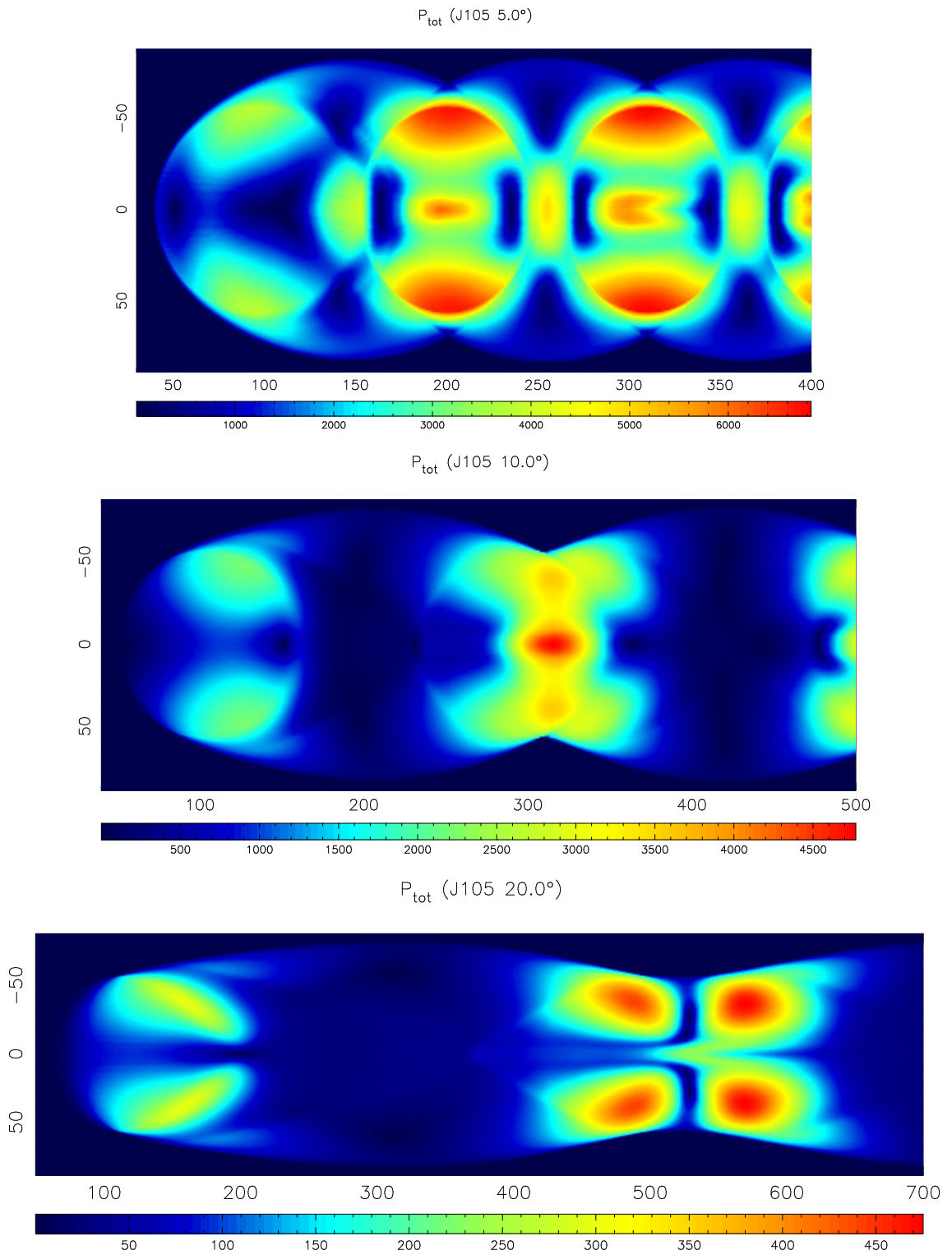


Figure 4.20: Simulated images of the polarized flux of the hot model are shown for viewing angles of (a) 5° , (b) 10° , and (c) 20° , from top to bottom, respectively.

CHAPTER 4

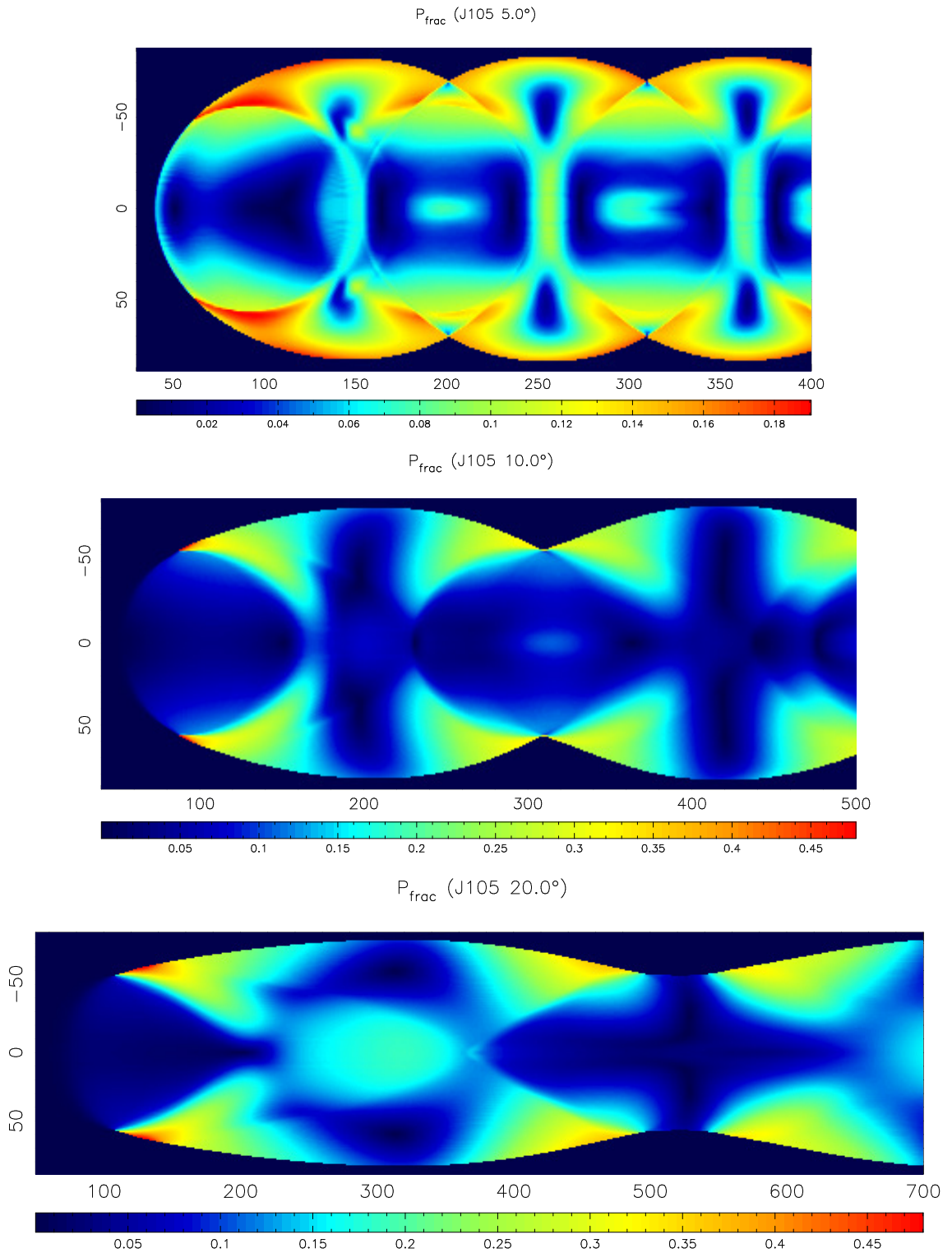


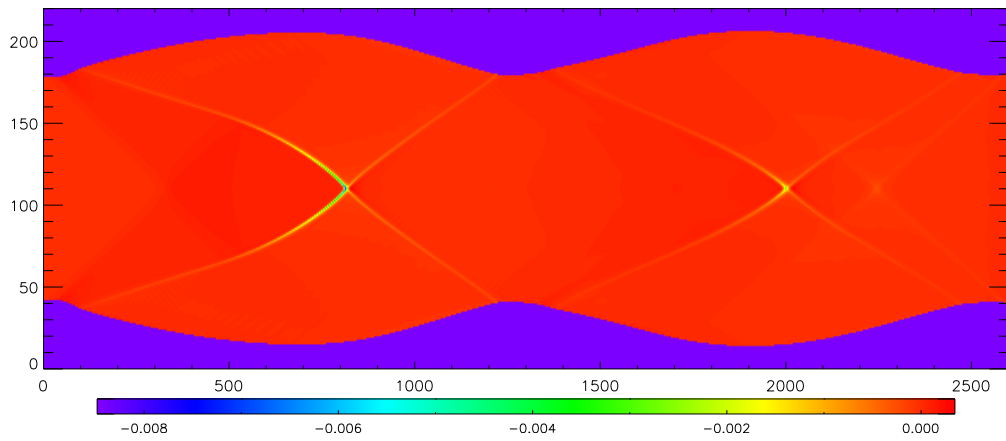
Figure 4.21: Simulated images of the fractional polarization of the hot model are shown for viewing angles of (a) $\theta = 5^\circ$, (b) 10° , and (c) 20° , from top to bottom, respectively.

CHAPTER 4

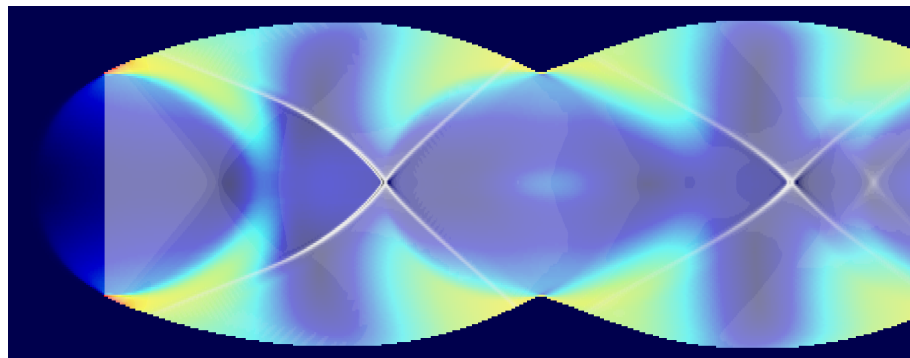
bubble is significantly lower than that of the pinch point; this is consistent with Figure 4.11, which shows that with increasing viewing angle (after $\theta \approx 4.5^\circ$), the level of polarization decreases until the (weakly) polarized flux transitions from being jet perpendicular to the jet projection to parallel at $\theta \approx 12^\circ$.

Figures 4.11 and 4.13 predict that the total polarization is generally lower at higher viewing angles, and we find this to be the case by considering the colour-bars in Figure 4.20. A detailed description of the distribution is difficult, due to the complexity of their patterns; despite this, we find that for each of the images, the global polarization maxima appear near the pinch points of the jets. The fractional polarization images (Figures 4.21) show that the range of I is much lower for the $\theta = 5^\circ$ case, but at all viewing angles we see that the regions of greatest fractional polarization lie off-axis, along an X-shape close to the projection of the shock surfaces. It is suggested that this is a signature of the conical shock fronts in the bubbles; in Figure 4.22a we show a plot of $\Delta(\Gamma v_z)/\Delta z$ in the r - z plane for the hot model. This parameter acts as a proxy indicator for the position of shocks, as it highlights the regions in which the dominant velocity component changes most rapidly (i.e. where the flow is shocked). For the sake of demonstration, we show this plot overlaid and scaled to align with the fractional polarization distribution of the hot jet at $\theta = 10^\circ$ (Figure 4.22). Considering that Figure 4.22a shows the shock positions for a single slice through the centre of the jet, the correspondence between the shock positions and the regional separation of fractional polarization is remarkably clear. We do not expect the images to align perfectly, due to the projection of different emissivities for each cell along each line of sight, but this does demonstrate that bounded regions of significant change in fractional polarization are a reliable indicator of the locations of recollimation shocks.

CHAPTER 4



(a) Profile of $\Delta(\Gamma v_z)/\Delta z$ for the hot model in the r - z plane.



(b) Fractional polarization profile of the hot model at $\theta = 10^\circ$, overlaid with the stretched, translucent $\Delta(\Gamma v_z)/\Delta z$ profile.

Figure 4.22: The locations of the shocks in the hot model are indicated in the upper panel; this has been scaled such that its radial maxima and minima align with those of Figure 4.21b, and overlaid in the bottom panel.

CHAPTER 4

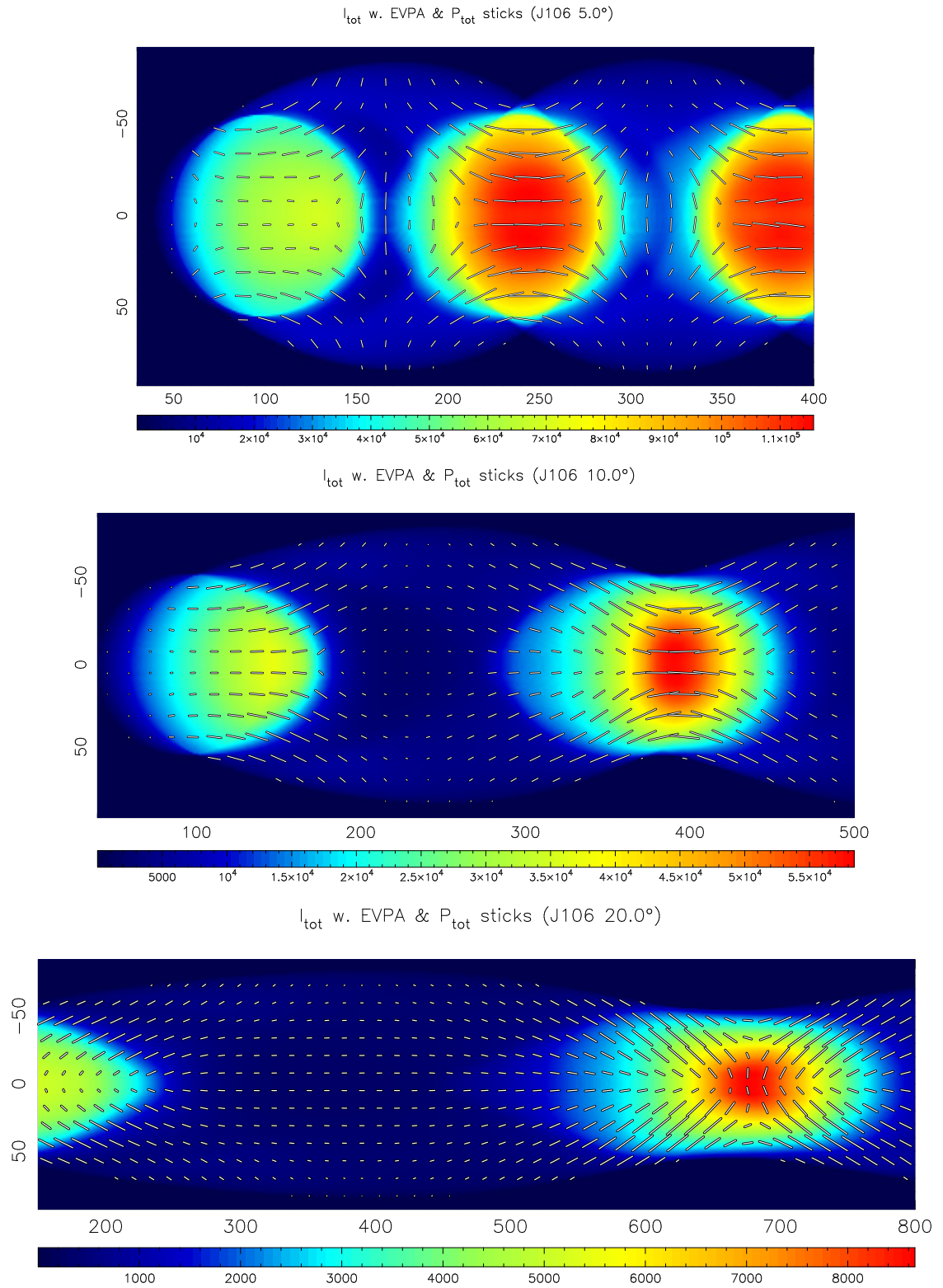


Figure 4.23: Simulated images of the total flux of the intermediate model, overlaid with polarization sticks, are shown for viewing angles of (a) 5°, (b) 10°, and (c) 20°, from top to bottom, respectively.

CHAPTER 4

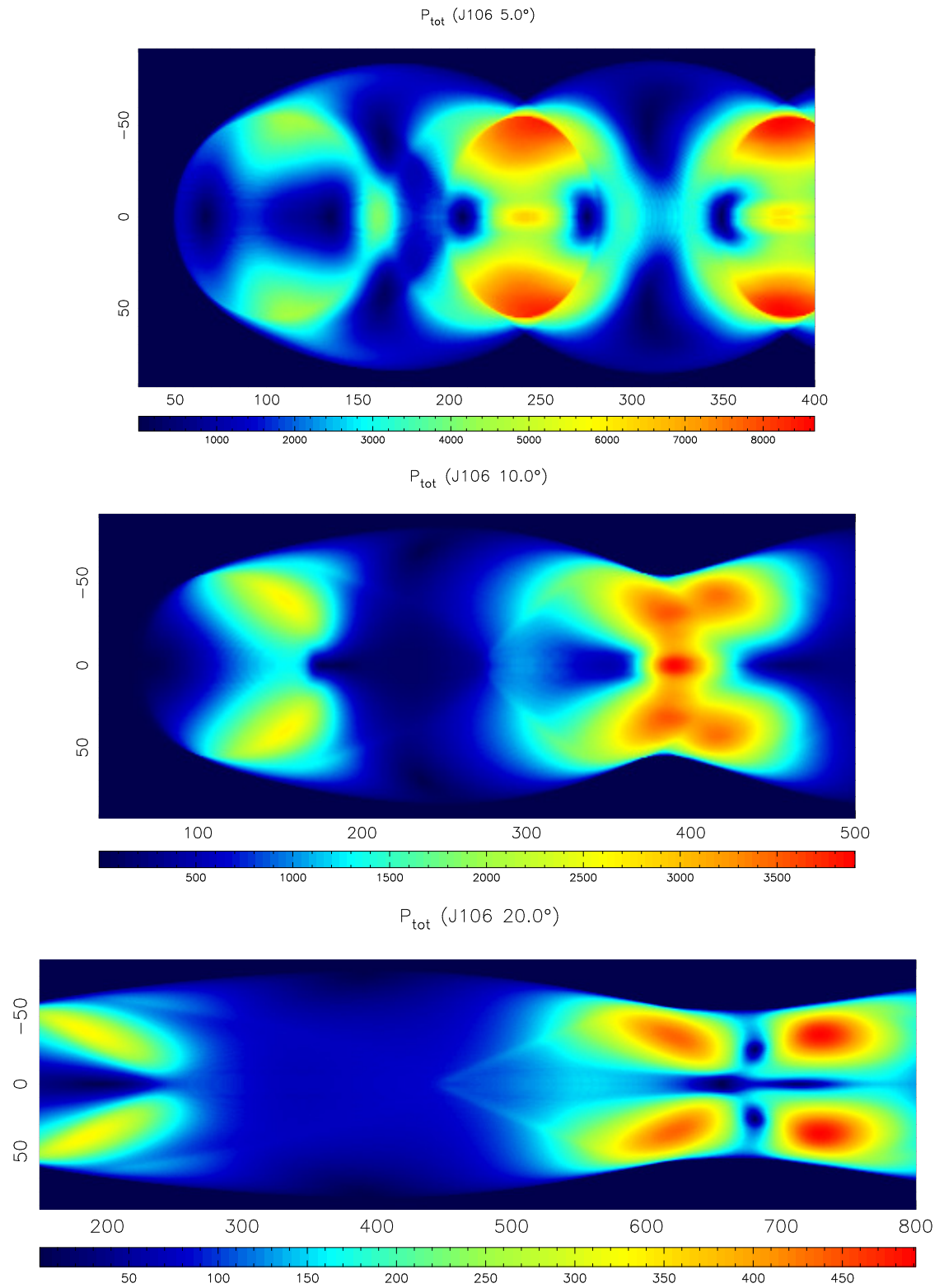


Figure 4.24: Simulated images of the polarized flux of the intermediate model are shown for viewing angles of (a) 5°, (b) 10°, and (c) 20°, from top to bottom, respectively.

CHAPTER 4

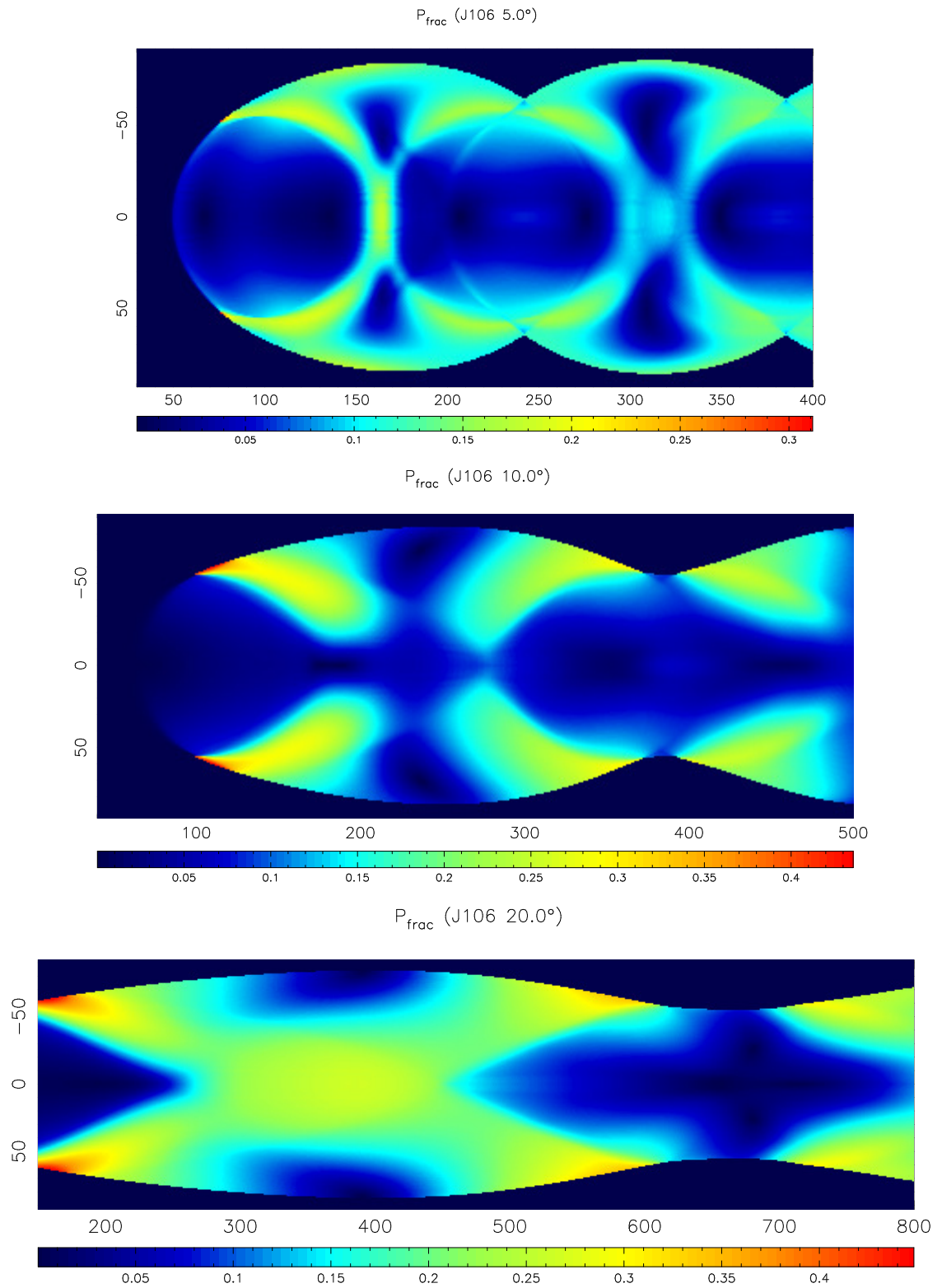


Figure 4.25: Simulated images of the fractional polarization of the intermediate model are shown for viewing angles of (a) 5° , (b) 10° , and (c) 20° , from top to bottom, respectively.

Intermediate Jet Images

Figures 4.23–4.25 show the intermediate jet’s total emission with EVPA sticks, its total polarized flux P , and its fractional polarization Π , respectively; the panels within each image show the model viewed at an angle of $\theta = 5^\circ$, 10° , and 20° . The total intensity and EVPA plots (Figure 4.23) show that the regions of greatest polarization lie at the centre of the pinch point at $\theta = 5^\circ$ and 10° , both of which have electric vectors aligned with the projected jet axis; at $\theta = 20^\circ$, however, the polarization in the centre of the pinch point has rotated 90° to what it was at smaller viewing angle, and P is now largest in region surrounding the pinch (where $2500 \lesssim I \lesssim 6000$). This is explained by Figure 4.13, which shows that the total polarization in the pinch is much lower at $\theta = 20^\circ$ than at the smaller viewing angles, and Figure 4.14 shows that the EVPA flip within the pinch had only just occurred at $\theta \approx 18.5^\circ$. The polarization near the centre of the bubble is fairly strong at $\theta = 5^\circ$ (relative to P within the pinch point), and is aligned perpendicular to the projected jet direction. At $\theta = 10^\circ$, we see that the bubble is now much less polarized, and a rotation in EVPA is actually underway, as shown by Figures 4.11 and 4.12; as the polarization within the pinch continues to diminish with viewing angle, the relative polarization of the bubble seems to increase, and so we see similar levels of polarization in the bubble and pinch point at $\theta = 20^\circ$. As with the hot model, we see that the electric vectors are aligned with the projected jet direction at the outer edges where the jet is most pinched, and the polarization at the edges of the bubbles is still perpendicular to the jet axis; the level of polarization in this direction, however, reduces with increasing viewing angles, as does the area in which the electric vectors are purely perpendicular to the jet axis, and not partially oblique.

Again, describing the precise profiles of total polarization shown in Figure 4.24 would be extremely complex, and so we note the general trends and features instead. What becomes apparent at large viewing angles is that the region of greatest total

CHAPTER 4

polarization is off axis, just past the centre of the pinch, and a second, smaller region of slightly lower polarization is found off axis, just before the jet is most pinched. The total polarization images for this model (n.b. Figure 4.24b) seem to indicate that the initial regions of high polarization actually “fracture” into two regions of increased polarization, which then separate at larger viewing angles, leaving interstitial regions of very low polarization. Also similarly to the hot jet, the fractional polarization within the bubble tends to increase with viewing angle (Figure 4.25); at $\theta = 20^\circ$, most of the bubble has a fractional polarization of $\gtrsim 20\%$, with small regions at the edge of the bubble where $II \sim 10\%$. At smaller viewing angles, however, the centre of the jet has a fractional polarization that is ~ 2.5 times lower than the regions of enhanced II , located diagonally away from the centre of the bubble. The consistently low fractional polarization values within the pinch points, and the decrease in II within the bubble, followed by its increase, with viewing angle are both as expected from Figures 4.12 and 4.14; the rotation of EVPAs through 90° (where Stokes Q or U is consistently low) necessitates that there will be a point where the total polarization transitions through $P \approx 0$, which we see at the centre of the bubble in the intermediate model for $\theta = 10^\circ$.

Cold Jet Images

Figures 4.26–4.28 show the cold jet’s total emission with EVPA sticks, its total polarized flux, and its fractional polarization, respectively; the panels within each image show the model viewed at an angle of $\theta = 5^\circ$, 10° , and 20° . In Figure 4.26, at $\theta = 5^\circ$, it can be seen that the on-sky electric vectors at the centre of the bubble are aligned perpendicularly to the jet axis, although the polarization is very low (in comparison with that of the pinch). At larger viewing angles, the polarization in the bubble is seen to be of a similar level to that within the pinch point of the jet. The polarization at the centre of the pinch point goes from being very high (relative to

CHAPTER 4

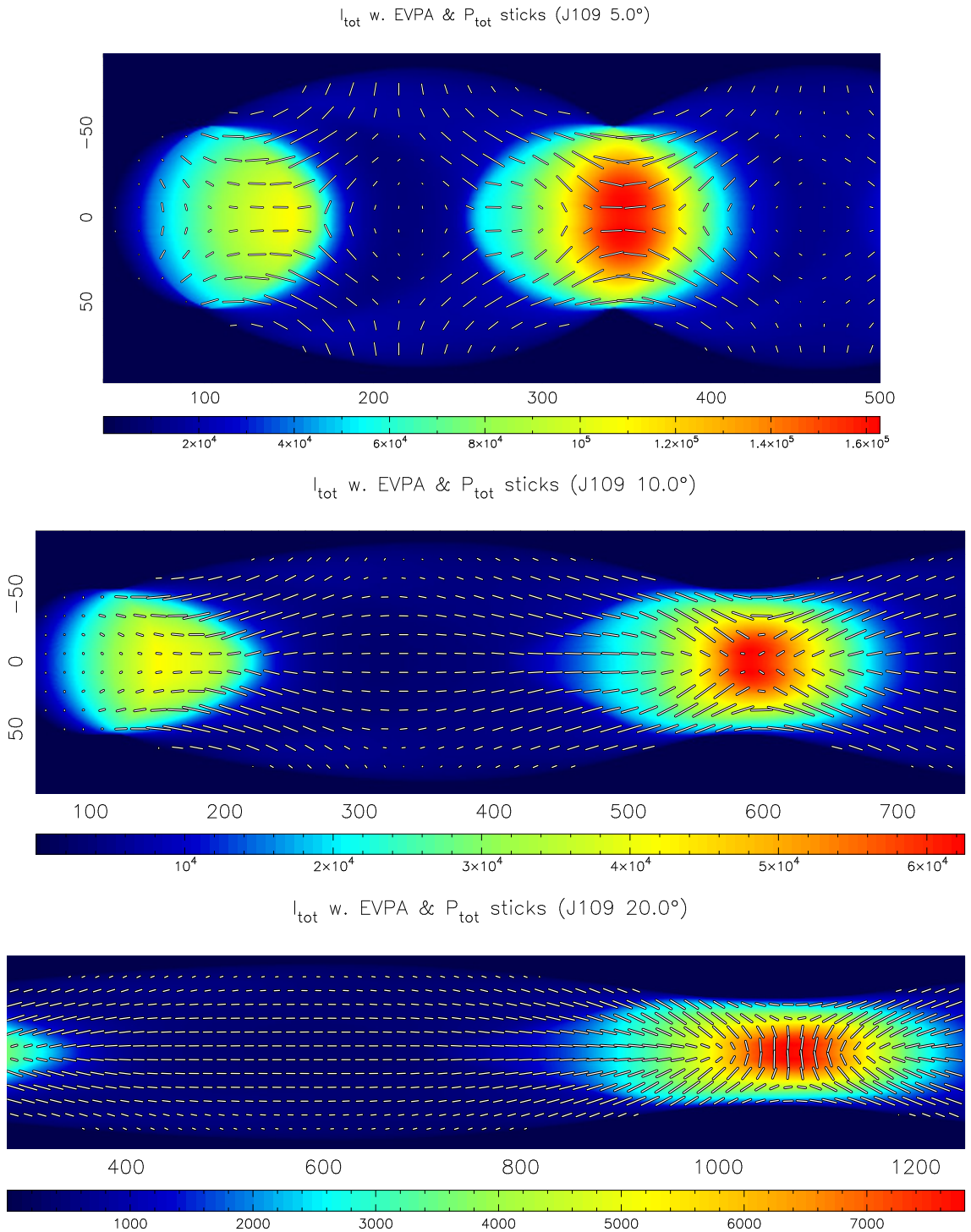


Figure 4.26: Simulated images of the total flux of the cold model, overlaid with polarization sticks, are shown for viewing angles of (a) 5°, (b) 10°, and (c) 20°, from top to bottom, respectively.

CHAPTER 4

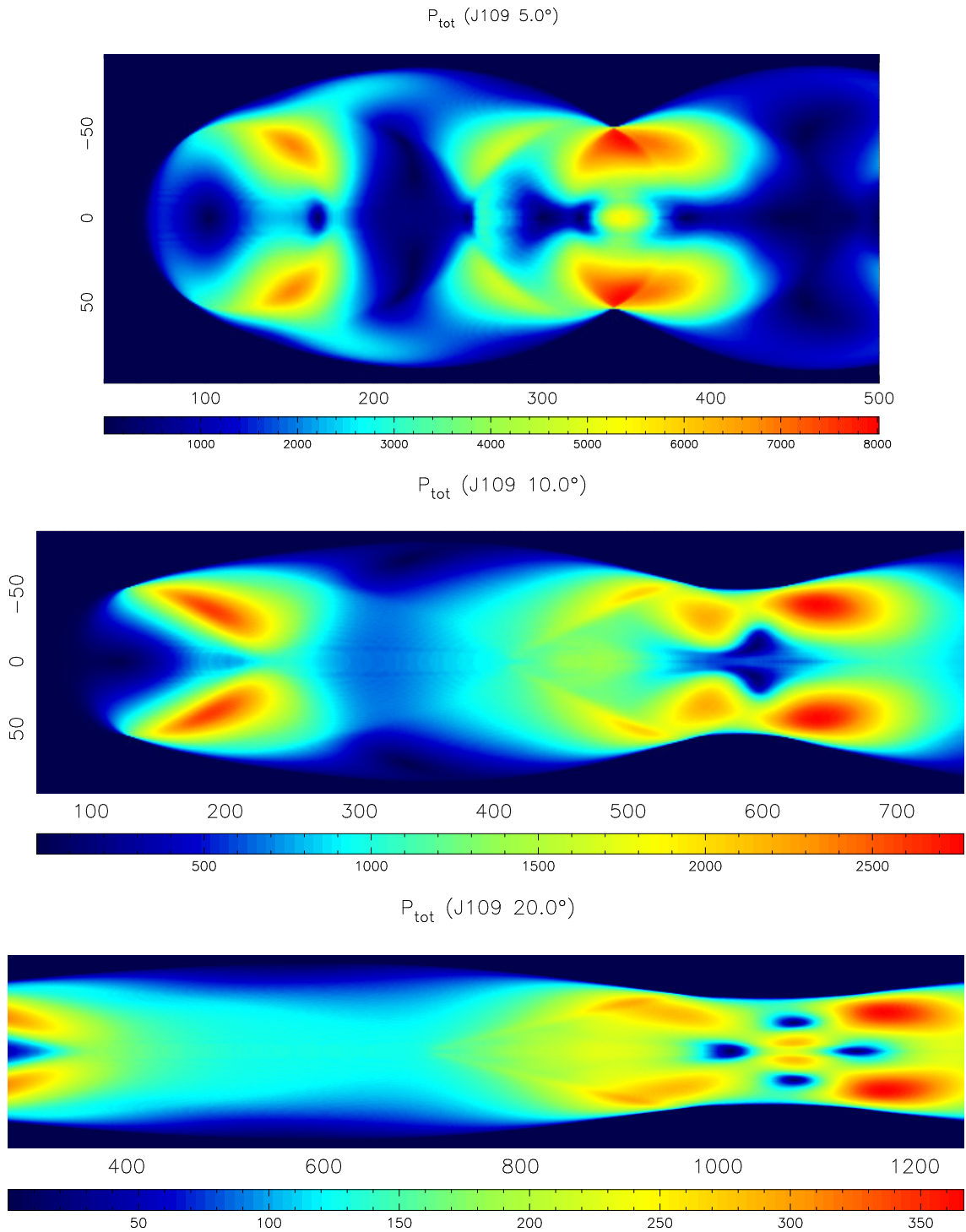


Figure 4.27: Simulated images of the polarized flux of the cold model are shown for viewing angles of (a) 5°, (b) 10°, and (c) 20°, from top to bottom, respectively.

CHAPTER 4

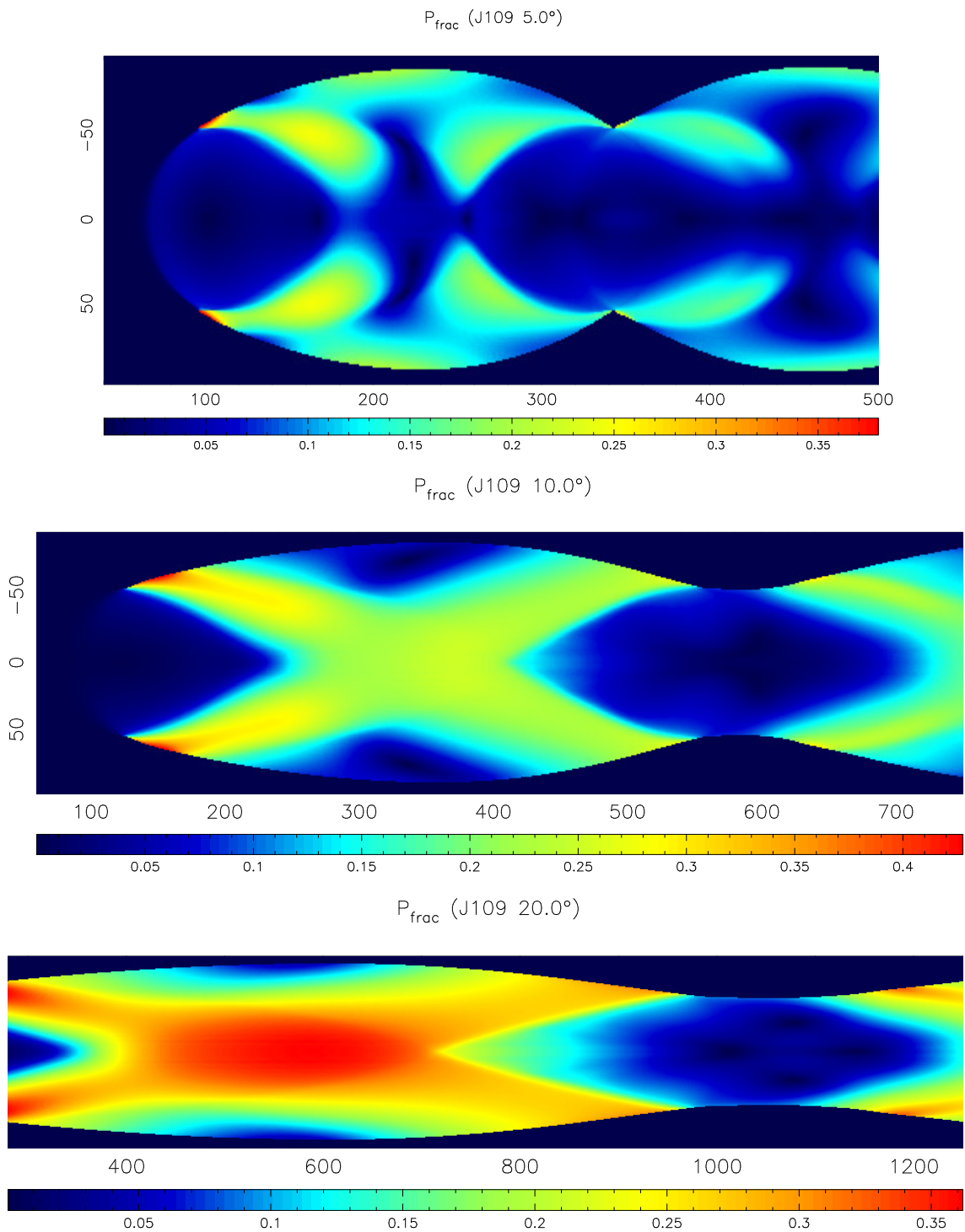


Figure 4.28: Simulated images of the fractional polarization of the model are shown at viewing angle of (a) 5° , (b) 10° , and (c) 20° , from top to bottom, respectively.

CHAPTER 4

the bubble), at $\theta = 5^\circ$, to being notably lower than that of the bubble at a viewing angle of 10° ; this is explained by Figure 4.13, which shows that this is close to the viewing angle at which the polarization of the jet pinch flips in orientation. The outer parts of the jet pinch points display greater levels of fractional polarization than the inner regions. As expected, in Figure 4.26c the polarization of at the pinch is perpendicular to the projected jet direction, and its magnitude is now of the same order as that within the bubble. At the edge of the bubble, the polarization is arranged perpendicularly to the projected jet direction at small viewing angles, but as θ increases, the size of this region diminishes until, as shown in Figure 4.26c, the polarization across the entire width of the bubble is parallel to the jet axis. It can also be seen that at, as the viewing angle increases, the EVPA sticks around the point of highest luminosity become more radially oriented, pointing outwards from the centre of the pinch point.

The maximum P of this model, shown in Figure 4.27, decreases with the increasing viewing angle. We also see each of the off-axis regions of maximal polarization about the pinch point “fragment”, with increasing θ , into two separate regions of relatively high polarization, with regions of very low polarization forming between these maxima. In the bubble, there is a central minima of P for the image at a viewing angle of 5° ; at larger viewing angles, the polarization of the bubble increases (relative to the maximal polarization values at the pinch points), such that an “X”-shaped region of increased polarization forms across the bubble, with two regions of lower polarization at the extremities of the bubble.

The same is true for the fractional polarization (Figure 4.28), with Π being larger around the edges of the bubble than the centre at $\theta = 5^\circ$, but at a viewing angle of 10° , the fractional polarization is definitely greatest in diagonal regions across the bubble. At larger viewing angles, the regions of low Π at the upper and lower edges of the bubble are diminished in size, but the region of low fractional polarization

CHAPTER 4

within the pinch persists in each of the viewing angles of the simulated images. As shown by Figure 4.22, the diagonal boundaries extending towards the centre of the bubbles are seen to align with the position of the RS within the jet; we can clearly see the presence of the RS in the cold jet by the sharp, oblique lines separating regions of low and high fractional polarization.

Inter-model Comparisons

As each model is observed from smaller viewing angles, its total and polarized flux densities increase, as can clearly be seen from the flux values in Figures 4.19, 4.23 and 4.26, and Figures 4.20, 4.24 and 4.27, respectively. These same images also show that, for the same viewing angles, the total and polarized flux densities are greater for the colder models (shown by the ranges on the colour-bars). This is due, at least in part, to the lower Mach numbers in the hotter models, meaning that the hot jets are able to respond to environmental influences over a shorter distance; this has the effect of making the recollimation shocks more oblique, and essentially “compressing” features in the z -direction, relative to the colder models. This degeneracy between viewing angle and model type will make it more difficult to determine a particular jet’s energy composition from these simulations, especially with poor constraints on the jet’s viewing angle.

From Figures 4.21, 4.25, and 4.28, we find that the maximum fractional polarization for any given model is generally found to occur at the edges of the jet, just before (or after) the jet is most radially compressed. In these locations, the lines of sight intersect jet material that is exclusively expanding (or contracting) radially, and generally has little magnetic field cancellation; at the edges of the bubbles the lines of sight intersect material that has a range of projected magnetic field orientations, leading to cancellation, which reduces the fractional polarization. The lower total and polarized fluxes here mean that this may be hard to detect in actual

CHAPTER 4

observations, however, depending on the sensitivity of the telescope in question.

The second-most fractionally polarized location within these jets is in the centre of the bubbles, especially at large viewing angles. At low viewing angles, the region of lowest fractional polarization in the bubbles generally extend perpendicularly to the jet axis; as the viewing angle increases, however, regions of high fractional polarization extend diagonally towards the centre of the bubble, eventually forming an “X”-shaped region of high fractional polarization, aligning with the on-sky projection of the RS. We have already shown that in Figures 4.20, 4.24, and 4.27 it is also possible to see the structure of the recollimation shock delineated in the profiles of polarized flux, although the shock surfaces tend to be more clearly visible in the hotter models, which is to be expected; as the RSs are strongest in the hotter models, the magnetic field is more highly ordered by the shocks, and so the fractional polarization is higher. We can also observe the trend that the fractional polarization is higher for each model at larger viewing angles; this is to be expected, as at smaller viewing angles each line of sight will intersect more regions producing differently polarized emission, resulting in a greater level of polarization cancellation.

Figures 4.20, 4.24, and 4.27 show that at $\theta = 5^\circ$, for all models, the largest regions of P are found where the jet is most pinched, near the edge of the jet. As the viewing angle increases, these regions of high polarization each begin to fragment into two separate regions of high P , such that four regions of high polarization (relative to P at the centre of the bubble) exist about the centre of the pinch points. The rate of this fragmentation with viewing angle appears to also be higher for colder models (see Figures 4.20b, 4.24b, and 4.27b in particular). In the simulated total polarization images it can also be clearly seen that the colder the jet, the higher the ratios of the downstream to upstream flux density in the fragmented P components.

At low viewing angles, all jets have polarization perpendicular to the jet axis in the bubble, and polarization parallel to the projected jet in the pinch point. We

CHAPTER 4

see that, as θ increases, the region at the edge of the bubbles where the electric polarization is mostly perpendicular to the jet is diminished in size (Figures 4.19, 4.23, and 4.26). The polarization of the pinch points near the edges of the jet, however, remain predominantly jet-parallel for any model or viewing angle. Except for these regions of fixed EVPA, the polarization pattern about these pinch points becomes increasingly radial with viewing angle, pointing away from the centre of the pinch point. The polarization at the centre of the pinch point, however, remains closely aligned with the projected jet axis for the hot model for $\theta \leq 90^\circ$, while the cooler models show a rotation to occur at $\theta \sim 10^\circ$ (Figure 4.14).

For each model, at every viewing angle, we find that the polarized flux density is greatest within the pinch points, with comparatively little polarized flux coming from the bubble (and RS therein); this is the same pattern as for Stokes I . Conversely, the fractional polarization in the pinch point is extremely small, while the degree of polarization within the jet bubble is significantly higher, reaching $\sim 30\%$ in some cases. This is because jet material is shocked by the first RS surface upon entering the bubble, causing the fluid to expand radially, increasing the ordering of the frozen in (initially disordered) magnetic field. Upon leaving the bubble, the fluid is shocked again at the latter surface of the RS, and is radially compressed; near the pinch point, the fluid has almost returned to its initial configuration, such that the magnetic field is almost completely disordered again. This means that, while the magnetized field density is greater in the pinch point (and thus the emissivity is also greater) than the bubble, the magnetic field is more ordered within the bubble, resulting in greater fractional polarization in the bubble. This increase in fractional polarization between knots has been observed, e.g. as seen between the core of 0836+710 and its first knot at a relative Declination of -2 mas (Figure 4.29; Lister et al., 2018), although this may be due to the poor characterization of the radiation where the flux density is significantly lower.

CHAPTER 4

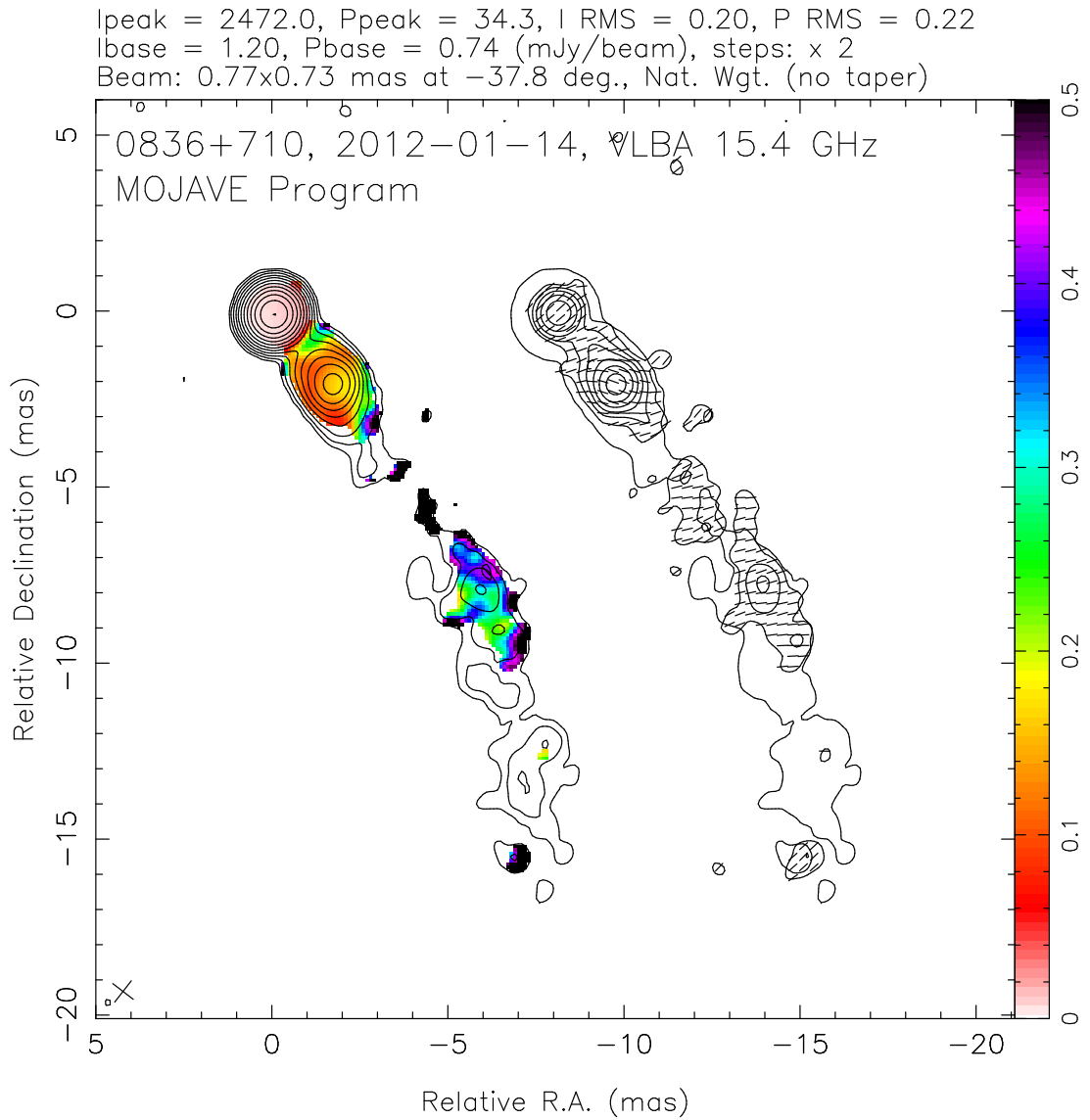


Figure 4.29: Images of 0836+710 at 15.4 GHz. Left: contours of total flux density, overplotted with the fractional polarization colour-map. Right: contours of polarized flux density, overplotted with sticks showing the EVPA.

4.3 Comparison with Observations

The simulated images presented in the previous section differ from VLBI observations in two significant ways. Firstly, our simulated images have infinite sensitivity, meaning that all emission produced by the jet model contributes to the final image; real observations are limited by factors such as equipment inefficiencies and background noise, which may result in a non-detection of a source's fainter features. Secondly, the simulated images have a significantly higher resolution than is available for most jet observations; in observations, it is not uncommon for the beamwidth to be of the order of the jet width, meaning that it is impossible to resolve any structure on scales significantly smaller than this. Convolution of simulated images with a Gaussian kernel is often used to mimic observational imaging limitations. If any of our simulated images were to be produced from VLBI observations, the total polarization at the pinch point would appear much less, due to beam depolarization from the rapidly changing EVPA, and the total jet size would be blurred across a much larger area.

In order to illustrate the effect of finite resolution, our simulated images have each been convolved with circular Gaussian kernels of FWHM 50, 100, and 150 pixels, which correspond to approximately one-, two-, and three-halves of a jet width, respectively. In Figure 4.30, simulated images of the cold jet at 20° are shown, with different levels of blurring applied; the original image (Figure 4.26c) has a strong radial EVPA distribution about its pinch point, but as the level of smoothing increases, the radial profile is quickly lost. The orientation of the polarization within the knot also transitions from being jet-perpendicular to jet-parallel as the smoothing increases. Bearing this in mind, we will compare these images with some observations that are plausibly represented by our models.

CHAPTER 4

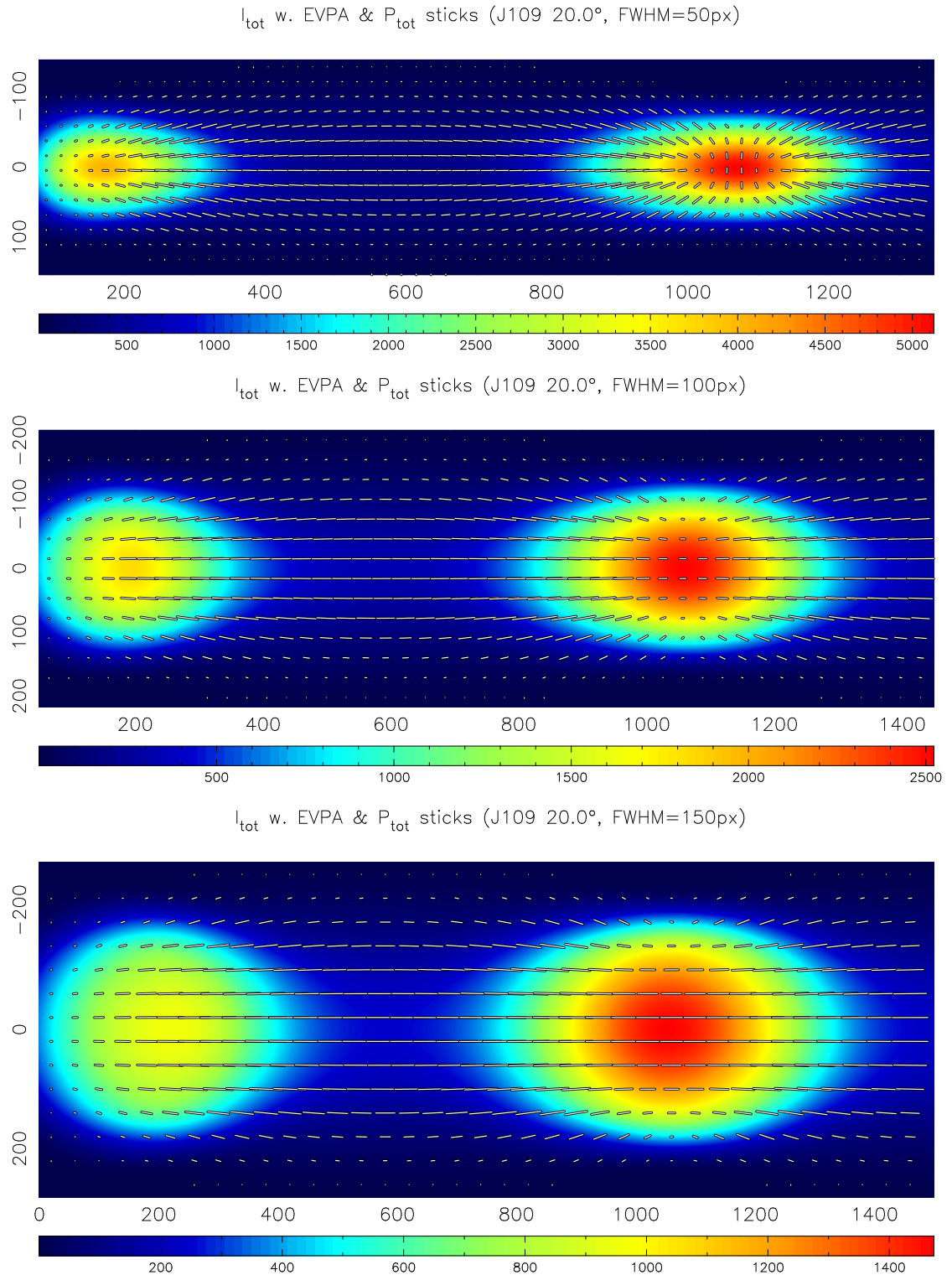


Figure 4.30: Simulated images of the total flux of the cold model, overlaid with polarization sticks, are shown for a viewing angle of 20° , after the image has been convolved with a Gaussian kernel of FWHM (a) 50 pixels, (b) 100 pixels, and (c) 150 pixels, from top to bottom, respectively.

4.3.1 0044+566

The radio source 0044+566 has been imaged several times between 2014 and 2019 by the MOJAVE VLBI array (Lister et al., 2018); during this period, the observed radio-core and adjacent stationary knot are seen to remain quiescent. There is little published work on this source, possibly due to its simple polarization profile; the polarization of the core and knot remain orthogonal to each other, aligning perpendicular and parallel to the jet axis, respectively (see Figure 4.31). In our simulated images, we find that the centre of each bubble and pinch point have orthogonal polarization at smaller viewing angles, e.g. the intermediate model at $\theta = 5^\circ$ (Figure 4.23a). These models only include optically thin emission, however, meaning that the radio-core may not be well replicated by our images, as this is an optically thick surface. If we only consider the knot, which we assume to be optically thin, then we can make some predictions about the source, but would require better constraints on some of the jet properties (e.g. orientation to the sky plane) in order to make more precise statements.

We find that each model could plausibly explain the polarization profile of the knot; the images at low viewing angles already have jet-parallel polarization, and if the images at larger viewing angles are significantly blurred, their initially radial polarization profiles become uniform and jet parallel. From the relative spacing of the radio-core and knot, if the core is the result of further recollimation shocks (as suggested by Daly & Marscher, 1988), it would appear that the viewing angle is quite small, the jet observations are significantly blurred, and/or the jet is best characterized by the hot model.

4.3.2 1803+784

The polarization profile of the radio-core within 1803+784 (Figure 4.32) has been modelled previously by Cawthorne et al. (2013, their Figure 1), who treat it as a

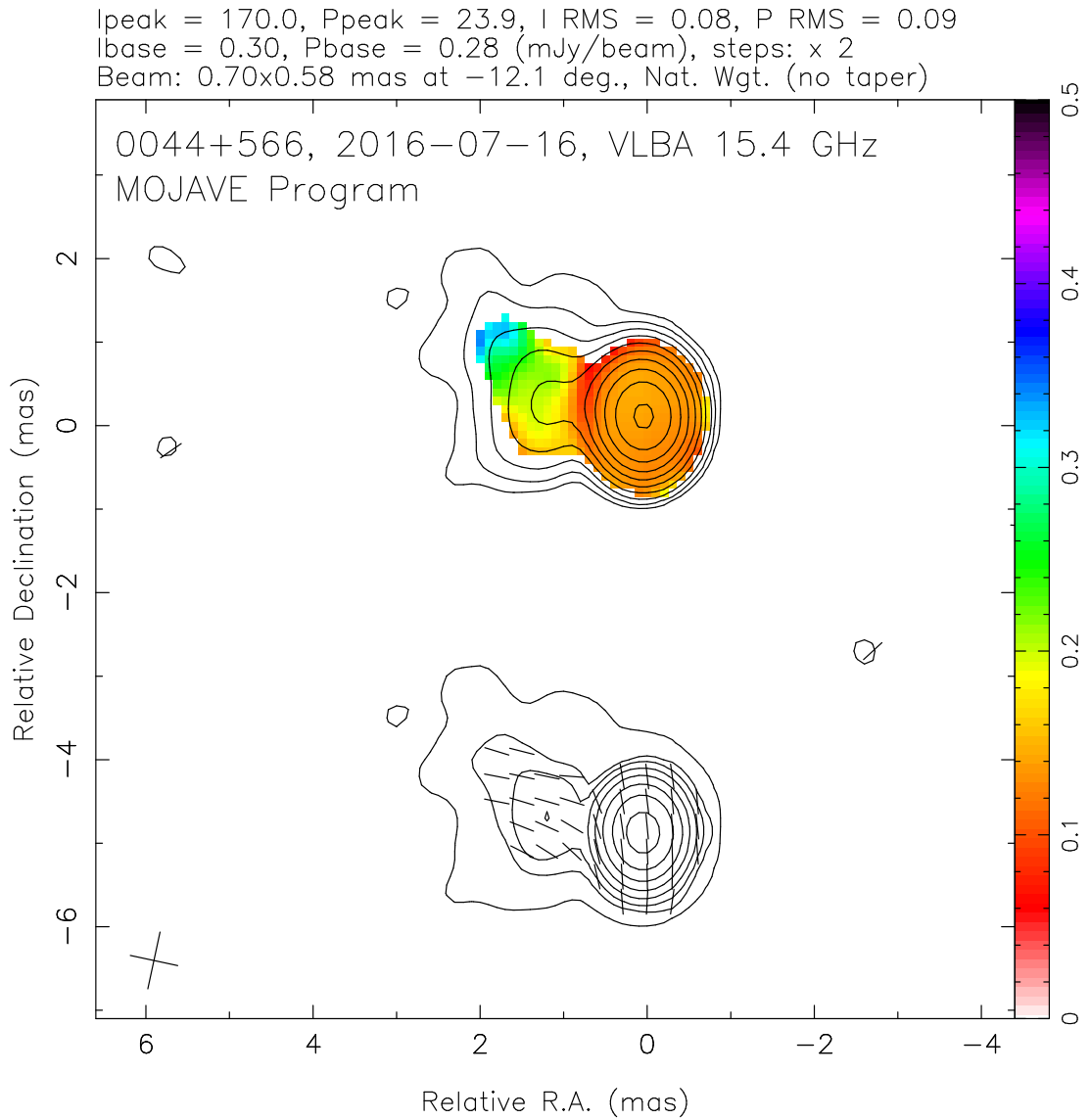


Figure 4.31: Images of 0044+566 at 15.4 GHz. Left: contours of total flux density, overplotted with the fractional polarization colour-map. Right: contours of polarized flux density, overplotted with sticks showing the EVPA.

CHAPTER 4

shock formed of two conical surfaces; under their assumption that the radiation emitted downstream of the RS is negligible, radically different results are found to what we present here.

Our simulations indicate that within a jet, the location of greatest flux, and radial polarization profile, actually occurs where the jet is most compressed, at the pinch point, downstream of a recollimation shock. Radial polarization profiles occur in each model type at large viewing angles, but colder models begin to present this radial pattern at lower viewing angles. The pinch point of the cold jet, viewed from $\theta = 20^\circ$ and blurred by a Gaussian kernel of FWHM 50 pixels is able to replicate the radial polarization profile and fractional polarization profile well (Figures 4.30a and 4.33b respectively), and the polarization maxima separated by the minima are also present in the simulated image. The total intensity contours of 1803+784 are much more circular than is seen in Figure 4.30a, however. This would suggest the viewing angle is likely to be less than 20° (suggested to be $\sim 1.4^\circ$ by Cawthorne et al.), but at smaller viewing angles the total polarization profiles are not in agreement with observations, and the polarization profiles have a more jet-parallel distribution.

This would imply that important features, such as the acceleration and ageing of the electron population, which have not yet been included in our calculations, may be vital in more accurately determining the emission of these jets. It is also possible that an initially purely disordered magnetic field is not responsible for the polarization properties seen in 1803+784.

4.3.3 M87

Avachat et al. (2016) present recent radio polarimetry of M87 and its jet, including knot HST-1. Images of the M87 nucleus and HST-1 knot are shown at a frequency of 22 GHz, and in the optical band. In their Figure 3, contours of total flux are overplotted with sticks of the total and fractional polarization, oriented with the

CHAPTER 4

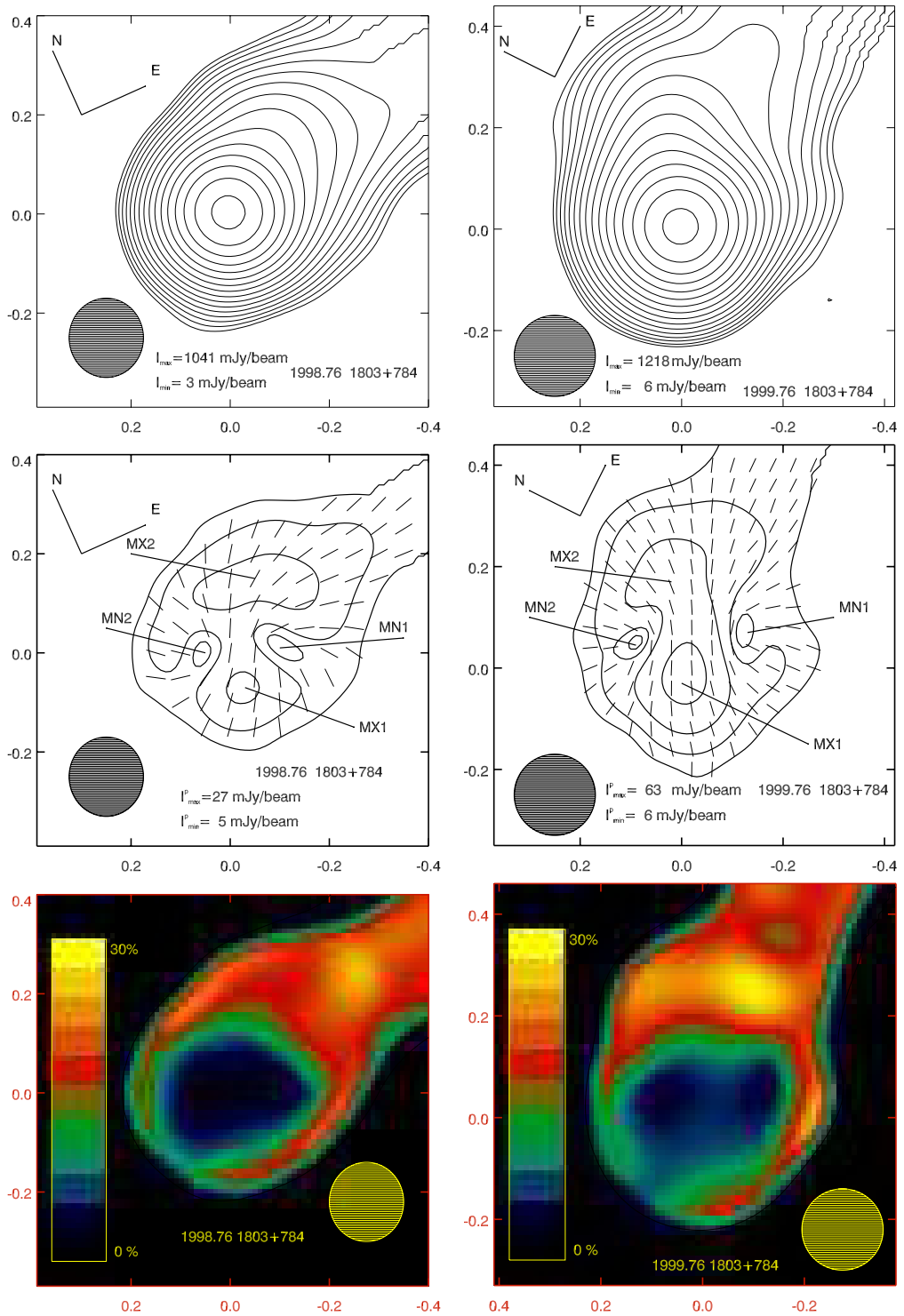


Figure 4.32: Images of 1803+784 at 43 GHz in 1998 (left) and 1999. From top to bottom, the panels show (a) contours of total intensity, (b) contours of polarized intensity, overplotted with EVPA sticks, and (c) fractional polarization colour-maps. The RA and Dec. scale is in mas, and the polarization minima and maxima are labelled MN1 and MN2, and MX1 and MX2, respectively.

CHAPTER 4

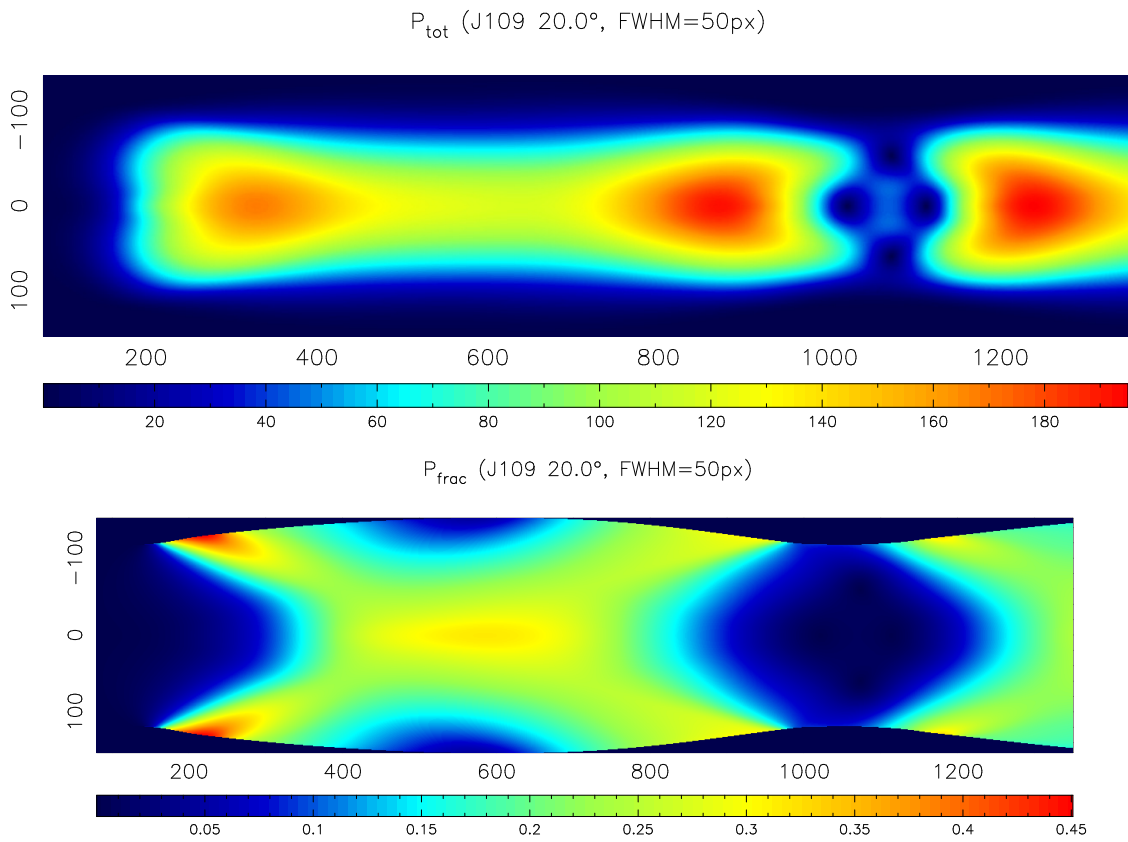


Figure 4.33: Simulated images of the polarized intensity (top), and fractional polarization of the cold model at $\theta = 20^\circ$, after the image has been convolved with a Gaussian kernel of FWHM 50 pixels.

CHAPTER 4

projected local magnetic field polarization; we show only the radio observations in Figure 4.34, and in the following discussion, we only consider the radio emission, unless explicitly stated.

The vectors plotted in these panels show the on-sky magnetic vector polarization, which will be orthogonal to that of the electric vectors, which we have considered thus far. When discussing the labels assigned in the upper panel of Figure 4.34, we use subscripts to distinguish between the labels associated with the nucleus and knot ($_{\text{N}}$ and $_{\text{k}}$, respectively).

The polarization of the electric vectors within HST-1 is mostly jet-perpendicular, with a slight radial profile around its edges, which we find in cold and intermediate jets at $\theta \gtrsim 10^\circ$, but not at all for the hot jet (see Figure 4.13).

In the region γ_{N} , the electric vectors near the centre of the jet are aligned parallel to the jet axis, and the vectors near the edge of the jet point towards the jet axis in the downstream direction. This polarization arrangement is what we find when fluid is leaving the bubble and approaching the pinch point; after it has travelled through the RS the electric vectors point towards the centre of the downstream pinch point. Our simulated images show this in the hot and intermediate jets at $\theta > 5^\circ$, and in the cold jet at $\theta \gtrsim 5^\circ$.

The total polarization is greater in HST-1 than γ_{N} ; conversely, the fractional polarization is greater in γ_{N} than HST-1. We see this in each of our models, especially at viewing angles $\theta > 5^\circ$.

The blurring of hot jet images at $\theta > 20^\circ$ may be able to produce jet perpendicular polarization in the pinch point, but the blurring of the hot jet at $\theta = 20^\circ$ serves to make more of the polarization jet-parallel, not jet perpendicular. Our models lead us to conclude that the jet of M87 is best characterized by either the intermediate or cold models, and (consistent with the assumption of Asada & Nakamura, 2012) the jet forms an angle of $\sim 20^\circ$ to the observer's line of sight.

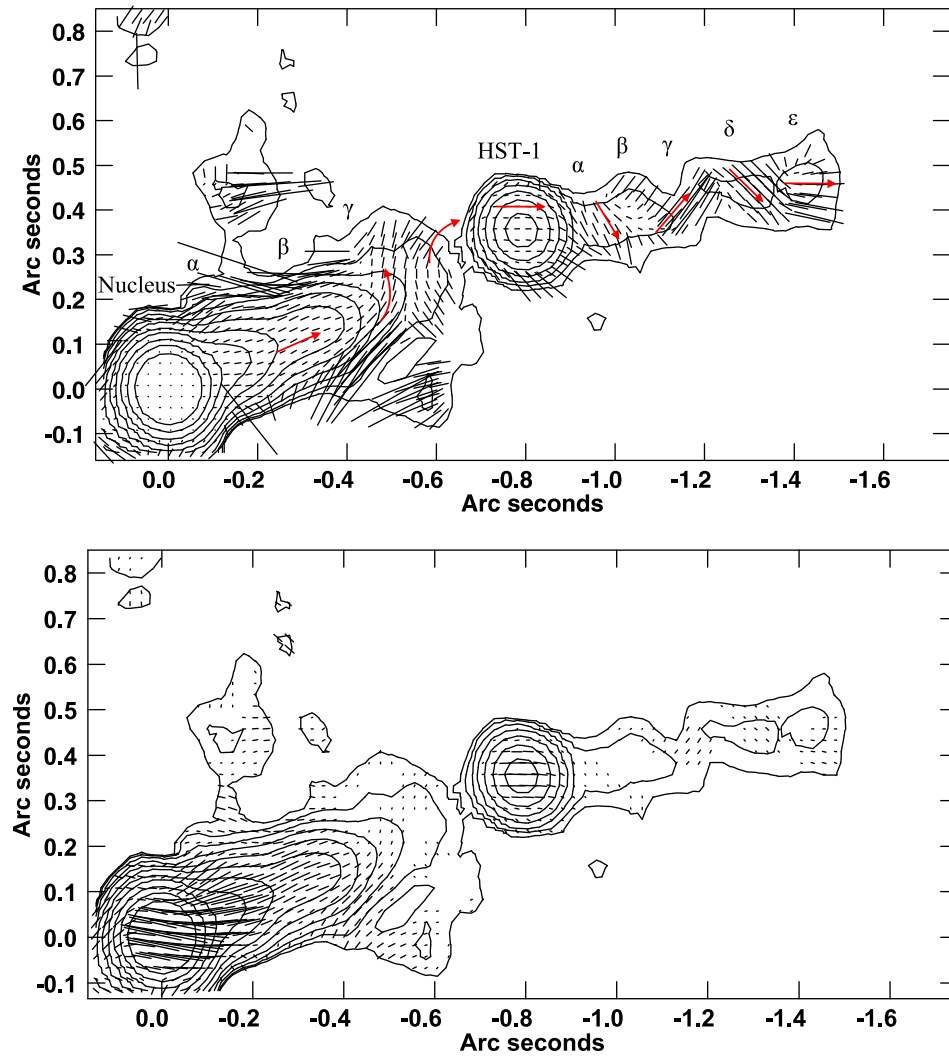


Figure 4.34: Nucleus of M87, and knot HST-1, as imaged at 22 GHz. Contours of total flux density, overplotted with magnetic field vector sticks of length proportional to either the fractional polarization (top), or the polarized flux density (bottom). Red arrows show the helical magnetic field proposed by Avachat et al. (2016).

CHAPTER 4

If we consider the effect of resolution, then blurring the intermediate model at $\theta = 20^\circ$ by a Gaussian kernel of FWHM 50 pixels, which is about half the width of the jet, causes in the polarization within the knot to become jet-parallel; as such if the jet of M87 is an intermediate jet, then it must be at a larger viewing angle.

For the cold jet at $\theta = 20^\circ$, convolved with a Gaussian kernel of FWHM 50 pixels, then the jet-perpendicular polarization within the shock persists, as does the radial profile about the perimeter of the pinch point, and the electric vectors near the end of the bubble point towards the centre of the pinch point. This is shown in Figure 4.30a.

This comparison is made under the assumption that no Faraday rotation has occurred, which may be incorrect. Avachat et al. present images of the same source in the optical band, showing that the EVPA for these different wavelengths do not align; either the radio emission has experienced Faraday rotation, or the local magnetic fields in the different regions where these wavelengths originate are very different. In the work of Avachat et al. (2016), it is concluded that there is a helical component to the magnetic field of the fluid leaving the nucleus; we will be able to compare our models to this prediction by including a helical component in the initial magnetic field, and seeing how strongly this persists after a RS.

This is a somewhat preliminary comparison of M87 with our simulated images; factors such as opacity, shock acceleration, and ageing of the electron population have all been overlooked.

Chapter 5

Summary and Conclusions

We have investigated methods to obtain synthetic images of total intensity and linear polarization of synchrotron radiation from relativistic magnetohydrodynamical simulations of an over-pressured jet that is radially expanding and contracting as it attempts to come into pressure-equilibrium with its surroundings; in doing so, the jet is subject to a series of conical recollimation shocks (RSs). Most earlier work of this nature has assumed some kind of ordered magnetic field, e.g. a helical field, but these produce high levels of linear polarization that are inconsistent with observations, and the resulting polarization often depends more on the specified magnetic field geometry than on the dynamics of the jet.

Another approach has been via semi-dynamical modelling (e.g. Cawthorne et al., 2013), in which an initially disordered magnetic field is partially ordered by passage through a conical shock wave. These analytical models assume that the emitting plasma cools rapidly as it moves away from the shock front, such that the emission is entirely from the region close to the shock front. This approach ignores the expansion and contraction of the jet that results in brightening of the jet near the pinch points.

In this work, we aimed to investigate the results of the passage of a plasma with

CHAPTER 5

an initially disordered magnetic field through a simulation of this kind. Fully three-dimensional relativistic magnetohydrodynamical simulations of a jet with magnetic field disordered on scales much less than the width of the jet would be extremely demanding of time on the most powerful computers, and is beyond the resources available for this project. Therefore we chose to adapt a method devised earlier by Matthews & Scheuer (1990), in which the disordered field is treated statistically. They injected marker particles at the base of the jet, each of which was initially cubic, but which evolved due to stretching and shearing of the plasma into a parallelepiped. The polarization for each parallelepiped is then determined by averaging over all possible directions of the initial magnetic field. A drawback of this method is clearly that the marker particles evolve to have an uneven distribution throughout the fluid, and their properties then have to be interpolated onto a regular grid, leading to errors that are hard to quantify. It was highly desirable to adapt this method so as to determine the parallelepipeds for each grid point.

Our initial approach was to incorporate the evolution of the parallelepipeds into a relativistic, three-dimensional fluid code, taking advantage of similarities between the Euler equations for fluid flow and the parallelepiped advection equation. The results of this work were described in Chapter 2. Our attempts to determine the parallelepiped base vectors by solving for them using a Godunov-type solver failed spectacularly; due to hardware restrictions, the greatest feasible resolution was insufficient for three-dimensional HuMiD simulations, leading to anomalies in the hydrodynamic structures and parallelepiped evolution within the jets. Beyond the first RS, the z -components of the parallelepiped vectors showed rapid and unphysical growth, beyond what was expected from the velocity distributions. Attempts to resolve this problem by evolving the parallelepiped vectors through an upwinded direct-differencing scheme were only partially successful. Furthermore, due to the limited computational domain, the initially cylindrical jets showed departures from

CHAPTER 5

cylindrical symmetry, adopting shapes with only four-fold rotational symmetry at various points. With no obvious way forward, and 2.5 years of PhD time consumed, it was necessary to look to another approach.

At this point, two-dimensional axisymmetric simulations were obtained from Prof. José-María Martí (University of Valencia), for steady state jets with initial Lorentz factor 3.2, over-pressured by a factor of 10 at the injection point. The three simulations provided were characterized by their internal energy density as “hot”, “intermediate” and “cold”, the exact parameters for each case being given in Table 3.1. Since we could not adapt the code used to generate these simulations, we chose a method of obtaining the parallelepiped vectors from the steady velocity field. In a steady flow, fluid particles follow streamlines, and so the evolution of the parallelepipeds as they move through the steady flow can be followed by tracking the corners of fluid particles as they move along streamlines. A method was devised for determining the parallelepipeds at each grid point, avoiding the problem of an uneven distribution. This method, together with methods for transferring the parallelepipeds onto a 3D grid, and determining the Stokes parameters, are described in Chapter 3.

The scientific results of this work are given in Chapter 4, wherein the features of the simulated images are outlined, and some observations are briefly compared to simulated images. The conclusions of this work are set out in the following section.

5.1 Conclusions

The brightest features in the jets are found at the pinch points, which are generally brighter than the neighbouring bubbles by a factor $\gtrsim 10$. This contrast results from the dependence of emissivity and magnetic flux density, both of which increase when plasma is compressed. The polarization of in this region tends to be relatively low, however, which mitigates against simple interpretations of the results.

CHAPTER 5

The emission characteristics of the bubbles and pinch points differ markedly. In Figures 4.11–4.14 we presented plots of Stokes Q and $|Q|/I$ as a function of the viewing angle θ for lines of sight in the (central) x - z plane, intersecting the widest points of the bubbles and the narrowest pinch points.

For small line of sight angles, the bubbles show on-axis EVPAs indicating a direction parallel to the projected jet axis. For line of sight angles over about 5° , there is a 90° change, with EVPAs indicating a direction perpendicular to the projected jet axis.

In the bright pinch points, the EVPA directions change from perpendicular to parallel, and then (at least for the cold and intermediate cases) back to perpendicular again, as the viewing angle increases.

The fractional polarization of the pinch points tend to be low, less than 10%, whereas the fractional polarization of the bubbles can rise as high as 35% (in the case of the cold model).

For small line of sight angles, the polarization directions at the pinch points tend to be fairly uniform, adopting an approximately radial pattern of \mathbf{E} vectors as the line of sight angle increases.

Figures 4.11–4.14 show that polarization variations for the three models—hot, intermediate, and cold—follow a similar variation as a function of line of sight angle. The fiducial points (e.g. maxima, minima, axis crossing points) occur at larger line of sight angles for hotter models. This is due to the larger spacing of the shocks and the larger shock cone angles in the hotter models; to pass through the same parts of the shock structure, a line of sight must be more steeply inclined to the axis in hotter than in colder jets.

The high level of fractional polarization found in the bubbles of the cold jet model, as high as 35%, may, ultimately, rule out such models as representations of astrophysical jets. It was found that the jet fluid almost returns to its initial

CHAPTER 5

configuration after traversing a RS, and as such the frozen-in magnetic field is disordered, resulting in low fractional polarization in the pinch points; further to this, the rapidly changing EVPA around the pinch points indicate that there is cancellation of polarization occurring along the lines of sight. Upon comparing the simulated images with observations of the radio core of 1803+784, it was found that the cold model at $\theta = 20^\circ$ provided the best match for the jet-perpendicular and radial EVPA patterns, and distributions of total and fractional polarization; however, 1803+784 is thought to have a very small viewing angle, and its circular intensity contours did not agree with the simulated intensity distribution. The source 0044+566 could be modelled by any of the jet types, with sufficient resolution degradation, making it of limited use. Observations of M87, however, were tentatively promising. The radial EVPA profile of the HST-1 knot was replicated by many simulated images, as were the jet-perpendicular electric vectors within the knot, and the electric vectors pointing towards the centre of the knot where the fractional polarization is high. This warrants a more careful study of other sources, with an aim to closely model specific sources.

The RS waves themselves are not readily apparent in the total or polarized flux density images. However, their imprint can be seen in the fractional polarization. The highest levels of fractional polarization are generally seen near an “X” shape, coincident with the projection of the conical shock wave. At small line of sight angles, the high levels of fractional polarization are concentrated at the outer parts of the X, but the inner parts become apparent, and even dominant, for larger line of sight angles.

5.2 Further Work

As this area of investigation has been somewhat overlooked by other works, many aspects of this work may be developed upon and warrant further investigation. It

CHAPTER 5

has been suggested by many authors (perhaps first by Daly & Marscher, 1988) that radio jets become bright at the position of the first RS, due to the disturbance of a previously quiescent electron population by the shock, perhaps involving Fermi particle acceleration at the shock front. If this is so, then to characterize the polarization that results, we need to incorporate opacity into the radiative transfer. This is straightforward for steady flows, and the opacities for the parallelepiped marker particles that characterize the emission properties can be obtained from an extension of the work of Cawthorne & Hughes (2013). Extending the present work in this way would enable us to address the question of whether optically thick RSs are good models for the cores of radio jets.

A further extension of this work could be to incorporate the ageing of electron populations into the radiative transfer. The age of the radiating particles associated with a marker particle is proportional to the number of iterations along a stream line required to reach its position from the base of the jet, and is automatically generated by the procedures described in Chapter 3. The average magnetic field strength at each point can be found from the parallelepipeds. Implementation of spectral ageing would allow us to investigate models in which the emissivities declined as fluid moves away from the shock fronts, perhaps allowing us to see the influence of the conical shocks in the total and polarized intensities. The results can be compared with the simpler semi-dynamical models (e.g. Cawthorne, 2006).

Although the formulae for determining the radiative transfer for two cases in which the initial magnetic fields are partially ordered (i.e. where the ordered component is uniform and parallel to the jet, and where it is helical) have been set out in Chapter 3, so far the resulting images have not been computed; this is due the limitation of time. However the results from these field configurations will be of great interest, particularly in view of the interest in helical magnetic fields arising from studies of Faraday rotation gradients (e.g. Gabuzda et al., 2015a,b).

CHAPTER 5

Again, through the limitation of time, our investigation has been restricted to a small region of parameter space: the three jets we considered all have the same initial Lorentz factor and over-pressure ratio. It should be straightforward to repeat our procedures for simulations obtained using other values of these variables. If it is possible to apply this method to time-dependent simulations, to do so would be computationally expensive. The velocity field at each time-step would be required, in order to determine the parallelepiped components for each grid point throughout the simulation, and advecting the marker particles would require the dynamic velocity field to be interpolated spatially and temporally. In semi-dynamical models of Cawthorne (2006), it was found that to a good approximation, increasing the Lorentz factor by some factor produced the same effect on the simulated images as reducing the viewing angle by the same factor, and it will be interesting to see whether the same scaling relationship exists in these numerical simulations.

It had been intended to extend this study by conducting a review of the polarization properties of radio jets in surveys (e.g. MOJAVE, Lister et al., 2018), and comparing the structures found there with the images presented in Chapter 4. The loss of time resulting from a major change of direction required by the failure of our initial approach (described in Chapter 2) means that this has been a fairly limited endeavour; however it is clearly a very important task to undertake. An inspection of images from the MOJAVE survey suggests that present imaging techniques may not have the resolution required to test the key predictions from our results. Clearly resolved images of the knots and inter-knot structures may have to await high frequency, high sensitivity observations with first-rate UV coverage. The Square Kilometre Array project (Grainge et al., 2017), for instance, is highly sensitive, and will be useful if it is able to surpass its expected upper frequency of ~ 15 GHz. The Event Horizon Telescope is expected to be able to image the base of the jet in M87 when including shorter baselines, which would also be a useful observation to have.

References

- Agudo, I., Gómez, J. L., Casadio, C., Cawthorne, T. V., & Roca-Sogorb, M. 2012, *ApJ*, **752**, 92
- Agudo, I., Gómez, J. L., Martí, J. M., et al. 2001, *ApJ*, **549**, L183
- Aller, H. D., Aller, M. F., & Hughes, P. A. 1985, *ApJ*, **298**, 296
- Amsden, A. A., Harlow, F. H., & Rayford Nix, J. 1977, *Phys. Rev. C*, **15**, 2059
- Anderson, J. D. 1995, *Computational Fluid Dynamics: The Basics with Applications* (McGraw-Hill)
- Antonucci, R. 1993, *ARA&A*, **31**, 473
- Antonucci, R. R. J. & Miller, J. S. 1985, *ApJ*, **297**, 621
- Asada, K. & Nakamura, M. 2012, *ApJ*, **745**, L28
- Avachat, S. S., Perlman, E. S., Adams, S. C., et al. 2016, *ApJ*, **832**, 3
- Binney, J. & Merrifield, M. 1998, *Galactic Astronomy* (Princeton University Press)
- Blandford, R. D. & Königl, A. 1979, *ApJ*, **232**, 34
- Blandford, R. D. & Payne, D. G. 1982, *MNRAS*, **199**, 883
- Blandford, R. D. & Znajek, R. L. 1977, *MNRAS*, **179**, 433
- Boccardi, B., Krichbaum, T. P., Bach, U., Bremer, M., & Zensus, J. A. 2016, *A&A*, **588**, L9

- Bridle, A. H. 1982, in IAU Symposium, Vol. 97, Extragalactic Radio Sources, ed. D. S. Heeschen & C. M. Wade, 121–128
- Bridle, A. H. 1992, in American Institute of Physics Conference Series, Vol. 254, American Institute of Physics Conference Series, ed. S. S. Holt, S. G. Neff, & C. M. Urry, 386–397
- Cawthorne, T. V. 2006, *MNRAS*, **367**, 851
- Cawthorne, T. V. & Cobb, W. K. 1990, *ApJ*, **350**, 536
- Cawthorne, T. V. & Hughes, P. A. 2013, *ApJ*, **771**, 60
- Cawthorne, T. V., Jorstad, S. G., & Marscher, A. P. 2013, *ApJ*, **772**, 14
- Cawthorne, T. V. & Wardle, J. F. C. 1988, *ApJ*, **332**, 696
- Cohen, M. H., Meier, D. L., Arshakian, T. G., et al. 2014, *ApJ*, **787**, 151
- Cohen, M. H. & Unwin, S. C. 1982, in IAU Symposium, Vol. 97, Extragalactic Radio Sources, ed. D. S. Heeschen & C. M. Wade, 345–353
- Condon, J. J. & Ransom, S. M. 2016, Essential Radio Astronomy (Princeton University Press)
- Daly, R. A. & Marscher, A. P. 1988, *ApJ*, **334**, 539
- Doeleman, S. S., Fish, V. L., Schenck, D. E., et al. 2012, *Science*, **338**, 355
- Duncan, G. C. & Hughes, P. A. 1994, *ApJ*, **436**, L119
- Edsberg, L. 2016, Introduction to Computation and Modeling for Differential Equations, 2nd edn. (Wiley)
- Eichler, D. 1993, *ApJ*, **419**, 111
- Einfeldt, B. 1988, in Shock Tubes and Waves, ed. H. Groenig, 671–676
- Event Horizon Telescope Collaboration. 2019, *ApJ*, **875**, L1
- Falle, S. A. E. G. & Wilson, M. J. 1985, *MNRAS*, **216**, 79

- Fanaroff, B. L. & Riley, J. M. 1974, *MNRAS*, **167**, 31P
- Fromm, C. M., Perucho, M., Porth, O., et al. 2018, *A&A*, **609**, A80
- Fuentes, A., Gómez, J. L., Martí, J. M., & Perucho, M. 2018, *ApJ*, **860**, 121
- Gabuzda, D. C., Cantwell, T. M., & Cawthorne, T. V. 2014, *MNRAS*, **438**, L1
- Gabuzda, D. C., Knuettel, S., & Bonafede, A. 2015a, *A&A*, **583**, A96
- Gabuzda, D. C., Knuettel, S., & Reardon, B. 2015b, *MNRAS*, **450**, 2441
- Gabuzda, D. C., Sitko, M. L., & Smith, P. S. 1996, *AJ*, **112**, 1877
- Garrington, S. T., Leahy, J. P., Conway, R. G., & Laing, R. A. 1988, *Nature*, **331**, 147
- Giovannini, G., Savolainen, T., Orienti, M., et al. 2018, *Nature Astronomy*, **2**, 472
- Gómez, J. L., Lobanov, A. P., Bruni, G., et al. 2016, *ApJ*, **817**, 96
- Gómez, J. L., Martí, J. M., Marscher, A. P., Ibáñez, J. M., & Alberdi, A. 1997, *ApJ*, **482**, L33
- Gómez, J. L., Martí, J. M., Marscher, A. P., Ibanez, J. M. A., & Marcaide, J. M. 1995, *ApJ*, **449**, L19
- Gourgouliatos, K. N. & Komissarov, S. S. 2018, *Nature Astronomy*, **2**, 167
- Grainge, K., Alachkar, B., Amy, S., et al. 2017, *Astronomy Reports*, **61**, 288
- Harten, A., Lax, P. D., & van Leer, B. 1983, *SIAM Review*, **25**, 35
- Hartley, P., Jackson, N., Sluse, D., Stacey, H. R., & Vives-Arias, H. 2019, *MNRAS*, **485**, 3009
- Hervet, O., Boisson, C., & Sol, H. 2016, *A&A*, **592**, A22
- Hervet, O., Meliani, Z., Zech, A., et al. 2017, *A&A*, **606**, A103
- Hughes, P. A., Aller, H. D., & Aller, M. F. 1985, *ApJ*, **298**, 301

- Hughes, P. A., Miller, M. A., & Duncan, G. C. 2002, *ApJ*, **572**, 713
- Jackson, J. D. 1975, *Classical Electrodynamics*, 2nd edn. (Wiley)
- Kahn, F. D. 1983, *MNRAS*, **202**, 553
- Kellermann, K. I., Condon, J. J., Kimball, A. E., Perley, R. A., & Ivezić, Ž. 2016, *ApJ*, **831**, 168
- Kino, M. & Takahara, F. 2004, *MNRAS*, **349**, 336
- Komissarov, S. S., Porth, O., & Lyutikov, M. 2015, *Computational Astrophysics and Cosmology*, **2**, 9
- Kosowsky, A. 1999, *New A Rev.*, **43**, 157
- Laing, R. A. 1980, *MNRAS*, **193**, 439
- Laing, R. A. 1988, *Nature*, **331**, 149
- Lister, M. L., Aller, M. F., Aller, H. D., et al. 2018, *ApJS*, **234**, 12
- Livio, M., Ogilvie, G. I., & Pringle, J. E. 1999, *ApJ*, **512**, 100
- Longair, M. S. 2011, *High Energy Astrophysics* (Cambridge University Press)
- Lynden-Bell, D. 1978, *Phys. Scr.*, **17**, 185
- Lynds, C. R. 1967, *ApJ*, **147**, 837
- Lyutikov, M., Pariev, V. I., & Gabuzda, D. C. 2005, *MNRAS*, **360**, 869
- Marcaide, J. M. & Shapiro, I. I. 1984, *ApJ*, **276**, 56
- Marscher, A. P. 2014, *ApJ*, **780**, 87
- Martí, J. M., Perucho, M., & Gómez, J. L. 2016, *ApJ*, **831**, 163
- Matthews, A. P. & Scheuer, P. A. G. 1990, *MNRAS*, **242**, 616
- Mizuno, Y., Gómez, J. L., Nishikawa, K.-I., et al. 2015, *ApJ*, **809**, 38
- Murphy, E., Cawthorne, T. V., & Gabuzda, D. C. 2013, *MNRAS*, **430**, 1504

- Mutel, R. L., Aller, H. D., & Phillips, R. B. 1981, *Nature*, **294**, 236
- Norman, M. L. & Winkler, K.-H. A. 1985, *Supersonic Jets*, Los Alamos Science No. 12 (Los Alamos National Laboratory)
- Pacholczyk, A. G. 1970, *Radio Astrophysics: Nonthermal Processes in Galactic and Extragalactic Sources* (W. H. Freeman and Company)
- Padovani, P. & Urry, C. M. 1992, *ApJ*, **387**, 449
- Park, J., Hada, K., Kino, M., et al. 2019, *ApJ*, **871**, 257
- Paterson, A. R. 1984, *A First Course in Fluid Dynamics* (Cambridge University Press)
- Penrose, R. 1969, *Nuovo Cimento Rivista Serie*, **1**
- Porth, O. & Komissarov, S. S. 2015, *MNRAS*, **452**, 1089
- Rees, M. J. 1966, *Nature*, **211**, 468
- Roca-Sogorb, M., Perucho, M., Gómez, J. L., et al. 2009, in *Astronomical Society of the Pacific Conference Series*, Vol. 402, *Approaching Micro-Arcsecond Resolution with VSOP-2: Astrophysics and Technologies*, ed. Y. Hagiwara, E. Fomalont, M. Tsuboi, & M. Yasuhiro, 353
- Rybicki, G. B. & Lightman, A. P. 1979, *Radiative Processes in Astrophysics* (Wiley-Interscience)
- Sanders, R. H. 1983, *ApJ*, **266**, 73
- Scheuer, P. A. G. 1974, *MNRAS*, **166**, 513
- Scheuer, P. A. G. 1984, in *IAU Symposium*, Vol. 110, *VLBI and Compact Radio Sources*, ed. R. Fanti, K. I. Kellermann, & G. Setti, 197
- Smith, M. D., Norman, M. L., Winkler, K.-H. A., & Smarr, L. 1985, *MNRAS*, **214**, 67

- Smith, R. J., Lucey, J. R., Hudson, M. J., Schlegel, D. J., & Davies, R. L. 2000, *MNRAS*, **313**, 469
- Stawarz, Ł., Aharonian, F., Kataoka, J., et al. 2006, *MNRAS*, **370**, 981
- Taylor, G. B. & Zavala, R. 2010, *ApJ*, **722**, L183
- Tchekhovskoy, A. 2015, in *Astrophysics and Space Science Library*, Vol. 414, The Formation and Disruption of Black Hole Jets, ed. I. Contopoulos, D. Gabuzda, & N. Kylafis, 45
- Thum, C., Agudo, I., Molina, S. N., et al. 2018, *MNRAS*, **473**, 2506
- Unwin, S. C., Wehrle, A. E., Urry, C. M., et al. 1994, *ApJ*, **432**, 103
- Urry, C. M. & Padovani, P. 1995, *PASP*, **107**, 803
- van Groningen, E., Miley, G. K., & Norman, C. A. 1980, *A&A*, **90**, L7
- Wardle, J. F. C. 2013, in *European Physical Journal Web of Conferences*, Vol. 61, European Physical Journal Web of Conferences, 06001
- Wardle, J. F. C., Homan, D. C., Ojha, R., & Roberts, D. H. 1998, *Nature*, **395**, 457
- White, C. J., Stone, J. M., & Quataert, E. 2019, *ApJ*, **874**, 168
- Williams, A. G. & Gull, S. F. 1985, *Nature*, **313**, 34
- Wilson, A. S. & Colbert, E. J. M. 1995, *ApJ*, **438**, 62
- Wilson, M. J. & Falle, S. A. E. G. 1985, *MNRAS*, **216**, 971
- Worrall, D. M. & Birkinshaw, M. 2006, in *Lecture Notes in Physics*, Berlin Springer Verlag, Vol. 693, Physics of Active Galactic Nuclei at all Scales, ed. D. Alloin, 39
- Zamaninasab, M., Clausen-Brown, E., Savolainen, T., & Tchekhovskoy, A. 2014, *Nature*, **510**, 126
- Zamaninasab, M., Savolainen, T., Clausen-Brown, E., et al. 2013, *MNRAS*, **436**, 3341